Coordination Dependent Magnetic Properties of 3*d* and 4*d* Metal Nano-Structures

THÈSE N^{O} 4559 (2010)

PRÉSENTÉE LE 29 AVRIL 2010

À LA FACULTE SCIENCES DE BASE
LABORATOIRE DE SCIENCE À L'ÉCHELLE NANOMÉTRIQUE
PROGRAMME DOCTORAL EN PHYSIQUE

ÉCOLE POLYTECHNIQUE FÉDÉRALE DE LAUSANNE

POUR L'OBTENTION DU GRADE DE DOCTEUR ÈS SCIENCES

PAR

Violetta SESSI

acceptée sur proposition du jury:

Prof. G. Dietler, président du jury
Prof. K. Kern, directeur de thèse
Prof. P. Gambardella, rapporteur
Prof. T. Greber, rapporteur
Prof. W.-D. Schneider, rapporteur

ÉCOLE POLYTECHNIQUE
FÉDÉRALE DE LAUSANNE
Suisse
2010

Abstract

In this thesis, the magnetic properties of self-assembled $3d$ and $4d$ metal nano-structures supported on surfaces have been investigated. The atomic coordination within the nano-structures was found to profoundly affect important quantities such as the magnetic moment and the magnetic anisotropy. The use of thin, atomically flat insulating Xe spacers of 1-15 monolayers (ML) thickness allowed for a study of coordination effects in the two limits of strong and weak coupling with an underlying metal substrate. The systems were characterized by surface-sensitive methods, based on synchrotron radiation (X-ray magnetic circular dichroism, and X-ray scattering/diffraction) and variable temperature scanning tunneling microscopy (VT-STM). The VT-STM was developed and implemented during this PhD work.

First, the magnetism of Rh nano-structures on a Xe buffer layer has been investigated. Rh is non-magnetic in bulk but shows a finite magnetic moment upon reducing cluster sizes to below 100 atoms. Within this work a small, non-zero magnetic moment was found for Rh nano-structures situated on Xe. The effect of intra-cluster Rh-Rh coordination was observed to affect both the spin and orbital part of the magnetic moment, leading to strongly oscillating values at smallest cluster sizes. Further, the analysis of the spectroscopic data suggests an interpretation for the absence of magnetism in directly deposited Rh on Ag(100) that is based on the formation of a kinetically promoted Ag-Rh alloy.

Second, the buffer layer assisted growth (BLAG) was studied for submonolayer Co nano-clusters on Ag(111) and Pt(111) surfaces. The observation of the cluster formation process in the very early stages of BLAG revealed the paramount importance of the substrate in determining both magnetism and structural properties of the nano-clusters. On Ag(111), a weakly interacting substrate, the clusters form on the buffer layer independently from the metal substrate and show no magnetic anisotropy at this stage. As soon as the Xe is desorbed by sample annealing an in-plane anisotropy forms, as a consequence of the contact with the substrate. X-ray scattering and diffraction data support this interpretation and also show that in the limit of a single monolayer of Xe on Ag(111) the BLAG is a 'simple' atomic diffusion process, with a very high mobility of Co atoms on Xe. On a thick Xe buffer layer instead, due to a lower Xe-Xe binding energy and to the higher surface energy of Co compared to Xe, the deposition of Co provokes a re-arrangement of the Xe atoms.

On the other hand, on Pt(111) the BLAG process fails to ensure a cluster formation process ontop the buffer layer and independent of the metal substrate. Here in fact, electric dipolar interactions occurring between Co atoms and the substrate through the Xe layer, are strong enough to destroy the Xe ML order and bring the Co atoms in direct contact with the Pt(111) before Xe atoms are thermally desorbed. This complex process becomes evident from VT-STM investigations and by the occurrence of perpendicular magnetic anisotropy right after Co deposition on the Xe ML/Pt(111).

In a detailed discussion it is shown that magnetic properties like magnetic anisotropy and orbital/spin moments are strongly entangled with their morphology. Both morphology and magnetism are determined by the interaction with the environment. This opens the way to more complex systems, where the interaction with the medium is tuned such as to gain nano-structures with a pre-defined structure and function.

Third, the knowledge about the cluster-substrate interactions during BLAG was exploited to build highly ordered arrays of Co nano-structures on a patterned template substrate. In this case the hexagonal boron nitride (*h*-BN) nanomesh on Rh(111) was used. These systems have been employed to study the effect of hybridization of the Co d band with capping layers such as Pt, Au, Al_2O_3 and MnPt on the magnetic moment of Co. It was found that in all these cases Co clusters have no remanence, due to the small size and weak coupling with the *h*-BN atoms. However, it could be shown that capping the clusters strongly influence the clusters magnetization, in a non-trivial way.

Keywords: magnetic nano-structures, Xe buffer layers, X-ray magnetic circular dichroism, scanning tunneling microscopy, X-ray surface scattering and diffraction, magnetic anisotropy.

Sommario

In questo lavoro di tesi sono state studiate le proprietà magnetiche di nanostrutture autoassemblate di metalli $3d$ e $4d$ depositate su superfici. Si è trovato che la coordinazione atomica all'interno delle nanostrutture è profondamente influenzata da impartanti grandezze quali il momento magnetico e l'anisotropia magnetica. Per studiare gli effetti di coordinazione nei limiti di accoppiamento forte e debole con il substrato metallico sottostante, sono stati utilizzati strati sottili isolanti di Xe piatti a livello atomico, di spessore variabile tra 1 e 15 strati atomici (monolayers, ML). I sistemi sono stati caratterizzti con tecniche sensibili alla superfice che utilizzano la luce di sincrotrone (*X-ray magnetic circular dichroism* e *X-ray scattering/diffraction*) e microscopia a scansione ad effetto tunnel a temperatura variabile (VT-STM). Lo sviluppo e l'implementazione dell'apparato VT-STM è stata parte integrante di questo lavoro di PhD.

Come primo esempio si è studiato il magnetismo di nanostrutture di Rh deposte su un *buffer layer* di Xe. Il Rh non ha proprietà magnetiche di *bulk* ma presenta un momento magnetico finito una volta che le dimensioni del *cluster* sono ridotte sotto i 100 atomi. Nell'ambito di questo lavoro si è trovato un momento magnetico piccolo ma diverso da zero per nanostrutture di Rh poste sullo Xe. Si è osservato che la coordinazione intra-cluster Rh-Rh influenza sia la parte di spin sia quella orbitale del momento magnetico, portando a valori fortemente oscillanti per i cluster di dimensioni minori. Inoltre, l'analisi dei dati spettroscopici suggerisce un'interpretazione riguardo all'assenza di magnetismo nel caso in cui il Rh è depositato direttamente sull'Ag(001) e che è basata sulla formazione di una lega Ag-Rh promossa da processi cinetici.

Nel secondo esempio, la crescita assistita da *buffer layer* (BLAG) è stata studiata per ricoprimenti inferiori al monolayer di cluster di Co su superfici di Ag(111) e Pt(111). L'osservazione del processo di formazione dei cluster durante i primissimi stadi della BLAG ha rivelato la fondamentale importanza del substrato nella determinazione delle proprietà magnetiche quanto di quelle strutturali dei nano-cluster. Nel caso di un substrato solo debolmente interagente come l'Ag(111), la formazione dei cluster sul buffer layer è indipendente dal substrato metallico e questi, inoltre, non mostrano anisotropia magnetica. La diffusione dei raggi X e la diffrazione confermano questa interpretazione mostrando, inoltre, che nel limite del singolo monolayer di Xe, sull'Ag(111) la BLAG è un 'semplice' processo di diffusione atomica con un'altissima mobilità degli atomi di Co sullo strato di Xe. Invece per un buffer layer spesso di Xe, a causa della bassa energia di legame Xe-Xe e all'alta energia di superficie del Co rispetto allo Xe, la deposizione del Co provoca un riarrangiamento degli atomi di Xe.

Nel Pt(111), invece, il processo BLAG fallisce nel garantire la formazione del cluster sopra il buffer layer ed in modo indipendente dal substrato metallico. In questo caso, infatti, le interazioni di dipolo elettrico tra gli atomi di Co e il substrato attraverso lo strato di Xe sono abbastanza forti da distruggere l'ordine del singolo strato di Xe e portare gli atomi di Co a diretto contatto con il Pt(111) prima che gli atomi di Xe siano desorbiti. Questo processo complesso è stato evidenziato mediante le misure VT-STM e dall'osservazione di anisotropia magnetica perpendicolare immediatamente dopo la deposizione di Co sul sistema Xe ML/Pt(111).

Attraverso una dettagliata discussione si mostra che le proprietà magnetiche quali l'anisotropia magnetica e i momenti di spin e orbitale sono fortemente legate alla morfologia. Magnetismo e morfologia sono determinati dall'interazione con l'ambiente circostante. Questo fatto apre la via allo studio di sistemi più complessi, dove l'interazione con il mezzo può essere accordata in modo tale da ottenere nanostrutture con struttura e funzione predefinite.

Infine, la conoscenza delle interazioni cluster-substrato durante la BLAG è stata sfruttata per costruire reticoli altamente ordinati di nanostrutture di Co su substrati la cui superficie è stata opportunamente modellata (*patterning*). In questo caso sono state usate nanomesh esagonali di nitruro di boro (h-BN) su substrati di Rh(111). Questi sistemi sono stati impiegati per studiare gli effetti sul momento magnetico del Co dovuti all'ibridizzazione delle bande d del Co con gli strati di copertura (*capping layers*) quali Pt, Au, Al_2O_3 e MnPt. Per tutti questi casi si è trovato che, a causa delle piccole dimensioni e del debole accoppiamento con gli atomi della h-BN, i cluster di Co non hanno magnetizzazione residua. Tuttavia, si è potuto dimostrare che ricoprire i cluster influenza fortemente la loro magnetizzazione, in modo non banale.

Parole chiave: nanostrutture magnetiche, *buffer layers* di Xe, *X-ray magnetic circular dichroism*, microscopia a scansione ad effetto tunnel, *X-ray surface scattering and diffraction*, anisotropia magnetica.

Contents

Abstract **i**

Sommario **iii**

1 Introduction **1**

2 Magnetism in reduced dimensions **5**
- 2.1 Magnetic anisotropy in reduced dimensions 8
- 2.2 Single domain nano-particles: superparamagnetism 13

3 Experimental techniques **19**
- 3.1 Scanning tunneling microscopy 19
  - 3.1.1 Principles and theory 19
  - 3.1.2 The home-made VT-STM 29
- 3.2 Synchrotron X-ray techniques 33
  - 3.2.1 Surface scattering and diffraction 33
  - 3.2.2 XAS and XMCD 43
- 3.3 Sample preparation and measurement procedure 52
  - 3.3.1 Rh nano-structures 52
  - 3.3.2 Co BLAG on Ag(111) and Pt(111) 54
  - 3.3.3 Co BLAG on the *h*-BN nanomesh 56

4 Experiments **59**
- 4.1 Rh nano-structures 59
  - 4.1.1 Magnetic moments of Rh/Xe 61
  - 4.1.2 Discussion 65
- 4.2 BLAG of Co on Ag(111) and Pt(111) 73
  - 4.2.1 Cluster growth on thick Xenon buffer layers 73
  - 4.2.2 BLAG with atomically thin Xenon layers 78
  - 4.2.3 *Ab-initio* calculations of magnetic Co_N islands on Ag(111) and Pt(111) 83

4.2.4 Discussion 84
4.3 GIXRD and GISAXS measurements 95
4.3.1 Growth of monolayer coverges of Co on atomically flat Xe layers 96
4.3.2 Growth of sub-monolayer coverages of Co on Xe/Ag(111) 99
4.3.3 Discussion 102
4.4 2D arrays of Co nano-clusters 105
4.4.1 *h*-BN nanomesh as a template for Co nano-clusters . . 106
4.4.2 Magnetic properties of capped Co nano-cluster arrays . 108
4.4.3 Discussion and open questions 112

5 Conclusions and outlook 115

Bibliography 119

Acknowledgments 129

Publications 131

Curriculum vitae 133

Chapter 1

Introduction

Nano-structures composed by only a few hundred atoms are very interesting and instructive objects, since they show special properties that are intermediate between those of single atoms and the bulk materials. For example, usually they are found to have spin and orbital moments that are higher than the corresponding bulk, and some elements like Rh and Pd that are non-magnetic in the bulk become magnetic as small clusters. In most cases though, even if nano-structures possess sizeable moments per atom, these structures have no permanent magnetization, e.g the magnetization is not stable, at least not at room temperature. This is due to the well known superparamagnetic limit, that up to now pushes the idea to use nano-structures as single bits in magnetic memories in the range of future technologies. A challenge of nanotechnology research in magnetism today is to find conditions for which structures are 'nano' and 'ferro' at the same time.

Nano-scale systems though, even if far from immediate applications, are extremely interesting from a basic-physics point of view, since they are the playground for a rich variety of phenomena. Since magnetism and electronic properties are closely related, the magnetic properties of nano-structures are very sensitive to the local environment. In complex bonding configurations 'exotic' effects such as non-collinear magnetism are observable. Even if most of these nano-structures cannot be used directly by industry at this stage, one should remember that nano-magnetism plays a key role in one of societies most developed tool: the GMR element as base of almost every computer.

In nanotechnology systems are fabricated using top-down techniques or bottom-up approaches. The latter methods are used in this thesis and are usually based on self-assembly processes. One of the most puzzling questions in self-assembly processes, is whether it is possible to build nano-structures with well defined shape, and well defined function. The word 'self-assembly' reminds of something 'natural', as if the system could self-select the right structure and scientists only have to pick it up. The truth is that there is nothing natural at a pressure of 10^{-10} mbar and the scientists themselves provoke the 'mutations', by fine tuning parameters and deciding which is the 'good' structure. Mutations are not random as in nature but induced by the researcher, and supported by a theoretical understanding of the processes. Thus one can expect that, different from Darwin's natural selection where successful mutations are very rare, the probability of finding the right structure is much higher.

Coming back from these abstract considerations to every day's lab life, it is obvious that there is a strong need for strategies to form nano-structures in a controlled way. Ideally one would like to look at the different interactions contributing in the self-assembly process separately, which all together lead to a final equilibrium shape and to certain magnetic properties of a nano-structure. In reality though these are very difficult to separate. The ultimate goal would be to be able to 'switch on' separately the different 'ingredients' of the perfect recipe for magnetic nano-structure growth: hybridization, RKKY, surface wetting, chemical bonds, polarization.

A way to study the magnetic properties of nano-structures while changing the degree of coupling with the environment is to use rare-gas layers pre-adsorbed on the surface. Rare gas can form atomically flat insulating layers that de-couple the nano-structures from the substrate. In 1989 a pioneering experiment showed that it was possible to grow Co films on Xe layers absorbed on GaAs [1]. This triggered the development of the technique called buffer layer assisted growth (BLAG) [2]. The aim of BLAG is to form clusters of a material A on a substrate B, but avoiding the interaction of A and B during the cluster formation process, that in many cases would result in the epitaxial growth of A/B. A noble gas buffer layer adsorbed on the substrate acts as a buffer between the substrate and the deposited single atoms. The rare gas is then removed simply by annealing the sample above the rare-gas desorption temperature. As a result nano-structures of the desired material A are formed on the desired substrate B.

For large amounts of rare gas, the dynamics of self-assembly on the noble gas is fairly independent of the deposited element (mostly metal) and substrate material. The size and density of the clusters at the end of BLAG then only depend on the rare gas and deposited metal coverage. In this sense the BLAG is considered to be a universal technique. In this so-called 'de-coupled' regime of BLAG the buffer layer can be used to investigate properties of deposited atoms and clusters in the 'quasi-free' limit. This is important because the contact with the substrate changes electronic and magnetic properties of the individual nano-structures. Decoupling conditions allow to study the effect of increasing nano-structure size (intra-cluster coordination) in an environ-

ment independently from the coordination with the substrate.
On the other hand for thin buffer layers experimental results have already hinted that an attractive van der Waals interaction between metal clusters and substrate can be strong enough to push the clusters inside the Xe buffer [3]. Wetting of the nano-clusters by Xenon and therefore partial incorporation into the Xenon layer has been predicted by molecular dynamics simulations [4]. These results indicate that the nano-cluster formation during BLAG is the result of a rather complex process that is not yet entirely understood. There is a the lack of experiments showing the first stages of cluster formation, between metal deposition on the buffer layer and removal of the Xe at temperatures below $T = 150$K. The main question to answer here is: What happens if the interaction with the substrate through the Xe cannot be neglected? Such conditions can be obtained in the limit of a single monolayer of rare-gas adsorbed on the surface, that is the 'coupled' regime of BLAG.

In this thesis the magnetism of $3d$ and $4d$ metal nano-structures on atomically flat Xe films with different thickness has been investigated. This has revealed to be a successful strategy to study the effect of coordination on the magnetic properties of nano-structures. It allowed in fact to observe the effect of the substrate-metal interaction in different regimes, from full de-coupling using a thick spacer layer to strong interaction as obtained on a single Xe layer. A variable temperature scanning tunneling microscopy (VT-STM) instrument was implemented and developed during the PhD thesis, that allowed for direct observation of cluster formation in the early stages of BLAG.
Two main goals have been achieved: (i) Modalities of the cluster formation process at different stages during BLAG were explored, identifying limits of the techniques but also new potentials; (ii) Important trends in the influence of the environment on magnetism in nano-structures are presented, indicating up to which extent it is possible to modify intrinsic properties of a material.
The thesis is organized as follows:

Chapter 2 introduces some of the basics concepts of magnetism at the nanometer scale, such as spin and orbital moment enhancement, magnetic anisotropy and superparamagnetism.

The experimental tools and methods used in the thesis are presented in Chapter 3. The working principle and the set-up of the home-made VT-STM are explained in Section 3.1, whereas synchrotron light related techniques are explained in Section 3.2. Section 3.3 deals with techniques for the preparations of the samples discussed in the thesis.

In Chapter 4 the experimental results are presented. The first experiment shown in Section 4.1 uses Xe layers as a separating layer between Rh nanostructures and a metal substrate. These experiments were motivated by a previous work, where the magnetism of Rh directly deposited on Ag(100) was found to be totally quenched [5]. The goal in the present work was to find conditions were the Rh magnetic moment is not destroyed by Rh-Rh and/or Rh-substrate interactions and second, to study in detail the dependence of spin and orbital magnetic moments on the quality and degree of Rh coordination. This could be achieved by X-ray absorption spectroscopy (XAS) measurements done with circularly polarized light revealing the electronic structure and magnetism of the Rh valence band, which is shown to be very sensitive to the atomic environment.

The second and third sets of experiments, shown in Sections 4.2 and 4.3, concern the BLAG *per se*, with the aim to understand the early stages of BLAG when the cluster formation occurs. The systems under investigation are Co/Xe/Ag(111) and Co/Xe/Pt(111). Section 4.2 is focused on studying the magnetic and structural properties of Co clusters on the two substrates, with the aim to clarify the role of substrate-cluster interactions. The combined use of X-ray magnetic circular dichroism (XMCD) and VT-STM techniques allows to develop models for the growth modes, which are very different in the two cases. The importance of the contact between clusters and substrate for the formation of magnetic anisotropy is discussed. In Section 4.3 the BLAG growth mode is explored from a different point of view using X-Ray surface scattering and diffraction techniques. The growth of Co on several Xe monolayers and on a mono-layer is compared, by investigating the structural changes occurring in the system Co/Xe/Ag(111) in the two cases.

In the last part of the thesis, Section 4.4, the BLAG is exploited from an application point of view. A patterned substrate, the *h*-BN nanomesh on Rh(111), is used to form ordered arrays of Co nano-clusters. The magnetism is studied in these systems, once the clusters are protected by non-magnetic or magnetic capping media.

Chapter 2

Magnetism in reduced dimensions

This paragraph will deal with free nano-magnets, made from a ferromagnetic material, like Fe, Ni and Co, but consisting of only a small number of atoms (below 10.000).

A small piece of a magnet, with size of a few nanometers, has an average magnetic moment per atom that is different from the one of a single atom but also from the one of the bulk material. The starting point to understand the origin of this behavior is to analyze qualitatively the differences in electronic structure, and consequently magnetic moment, when moving from one single atom towards the bulk, in the special case of Fe (see Fig. 2.1).
Fe atoms have eight electrons distributed in the $3d$ and $4s$ levels. To satisfy the Hund's rules that maximizes the spin, five electrons occupy the $3d$ level with spin up, two electrons occupy the $4s$ levels and finally one electron has spin down in the $3d$ level (see Fig. 2.1). The total spin moment in the ground state is therefore $4\mu_{\mathrm{B}}$.

The next step is to add more Fe atoms to the first one, bringing them close enough that electrons in the outermost levels can jump from one atom to the other. Sharing electrons leads to cohesion of the atoms (formation of chemical bonds) but also to a delocalization of the atomic orbitals, and formation of energy bands. While for s states that are more extended in space this delocalization is complete, it is incomplete for the d states, being closer to the atomic nucleus. The $3d$ electrons therefore retain partially the atomic character, with important consequences for their magnetic properties. One can calculate the magnetic moment, assuming that the $3d$ orbitals do not delocalize at all, that means one has to place one shared electron per atom in the $4s$ band and all the other 7 electrons localized in $3d$ orbitals. This is the local moment approximation or Heisenberg model that allows using

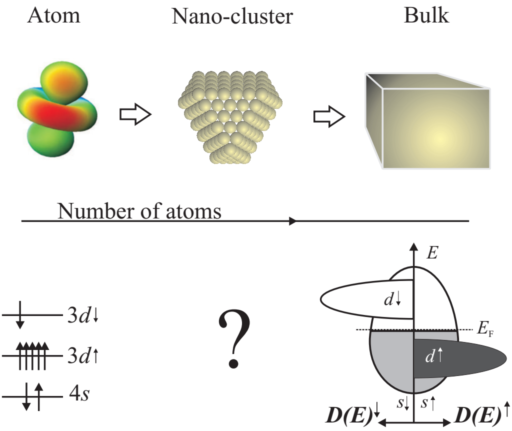

Figure 2.1: Schematic model showing the evolution of the electronic structure from single atom to bulk, in the special case of Fe.

the Hund's rules as in the case of a single atom to calculate the magnetic moment. In this case a value of $3\mu_\mathrm{B}$ per atom is found. Measurements done on bulk Fe samples actually give an even more reduced value of $2.2\mu_B$ per atom. The reason for this non-integer value is that in reality there is a partial delocalization for the $3d$ electrons as well, that makes the magnetic moments not entirely localized on the atomic cores. A model that takes into consideration the partial delocalization of the $3d$ levels is the Stoner model, or itinerant electron model [6]. Here, the $3d$ atomic levels are not discrete and are considered to form a d band. The width of the band though, inversely proportional to the degree of localization of the atomic states, increases almost continuously when adding one atom after the other until it reaches the bulk value.

Important experiments showing magnetic moment measurements for nanoclusters as a function of the number of atoms composing the cluster were performed in the beginning of the 90's [7–10]. It was necessary to develop the technology to fabricate mass-selected clusters and to measure their magnetic moment with high resolution. A cluster beam apparatus is composed of a laser vaporization (LV) cluster source to form the clusters and a time-of-flight (TOF) mass spectrometer to mass-filter the clusters. The average magnetic moments per atom $\overline{\mu}$ are determined by measuring the angular deviation of the clusters while passing through an inhomogeneous magnetic field (Stern-Gerlach experiment). In [10] magnetic moments of clusters composed of Fe, Co and Ni were investigated, as a function of the cluster size. In all three cases the average magnetic moment per atom decreases with increasing number of atoms inside a cluster. This decaying behavior indicates a gradual transition from atom-like electronic structure in case of small clusters towards a bulk-like one for larger clusters of about 400-500 atoms. The magnetic moment also shows an oscillating behavior versus cluster size, due to a different magnetic alignment among subsequent atom shells in the clusters and to magnetic anisotropy effects.

While trying to model the electronic and magnetic properties of a nano-cluster both atomic and bulk pictures are inadequate, due to the large fraction of atoms at the surface. Atoms at the surface are special because they have different electronic properties as compared to the bulk case, due to a reduced number of neighbors. This leads to a reduced hybridization and therefore to more localized $3d$ electrons (smaller width of the d band).

It is useful to consider this last case more in detail, since it has an important consequence: it suggests that 'band engineering' realized by reducing the dimension of a structure to the nanometer range can lead to non-vanishing magnetic moments. To understand this concept more quantitatively one can recall the Stoner criterion for spontaneous spin-splitting [11]. It states that ferromagnetism occurs only when the product of the density of states at the Fermi level $D(E_{\mathrm{F}})$ and the material dependent exchange integral is larger than 1: $D(E_{\mathrm{F}}) \cdot I > 1$. Three elements of the periodic table fulfill this requirement, due to their high value of d-states at the Fermi level: Fe, Co and Ni. A large number of states at the Fermi level is connected with a small d band width W_d: $W_d \propto \frac{1}{D(E_{\mathrm{F}})}$. Tight binding calculations have shown how there is a simple relation between W_d and the local environment in a nano-structure: $W_d = 2\sqrt{N} \cdot h_d$. Here N is the number of nearest neighbors and h_d is the hopping matrix element that depends on the overlap of nearest neighbors d orbitals and is therefore element specific. It is then clear that, by decreasing N the d band can be narrowed, with a consequent increase of $D(E_{\mathrm{F}})$ (for more details about this concept see Ref. [12]). In particular, transition metal elements that are non-magnetic in bulk might become magnetic in form of nano-structures like wires, clusters or impurities. Stern-Gerlach experiments on nano-clusters made out of Rh have shown the validity of this approach [13, 14]. Here, a non-vanishing magnetic moment has been measured for clusters with size below 100 atoms. The concept of 'band engineering' is used on Rh in Section 4.1.

2.1 Magnetic anisotropy in reduced dimensions

In the previous paragraph the average magnetic moment per atom $\overline{\mu}$ of a nano-structure has been considered assuming that it is the same in any direction in space. In reality magnets of any shape and size have preferential directions where the magnetization **M** wants to be aligned. These directions are called easy axis directions and they are defined by the system's magnetic anisotropy, which stabilizes the magnetization against thermal fluctuations. Without anisotropy there would be no permanent magnetization, as will be shown in the following. Therefore, the easy axis is a very important concept in magnetism, which influences also other properties like e.g. the width of domain walls. It is especially important in nano-magnetism, where the total magnetic exchange experienced by a single spin is smaller compared to bulk because of the reduced coordination of atoms (less spins available).

A special case of magnetic anisotropy is the magneto-crystalline anisotropy (MCA), were the atomic structure of the crystal in a magnetic system introduces preferential directions for the magnetization. The cost per atom to align the magnetization from one crystallographic direction to the other is called magneto-crystalline anisotropy energy (MAE). MCA phenomenologically implies that the energy of the system depends on the direction of the magnetization with respect to the crystal axes. To describe this dependence one usually describes the magneto crystalline energy per volume E_{cryst} of the system in terms of the components of the magnetization direction $\mathbf{M}/|\mathbf{M}|$ with respect to the crystal axes, the direction cosines $(\alpha_1, \alpha_2, \alpha_3)$. In a spherical coordinate system the direction cosines are defined as follows:

$$\alpha_1 = \mathrm{sin}\theta\mathrm{cos}\phi \tag{2.1}$$

$$\alpha_2 = \mathrm{sin}\theta\mathrm{sin}\phi \tag{2.2}$$

$$\alpha_3 = \mathrm{cos}\theta, \tag{2.3}$$

with θ and ϕ being the polar and azimuth angles, respectively.

E_{cryst} can now be written as a power series expansion of the direction cosines [15]. Different expressions are found, depending on the system symmetry. In case of uniaxial anisotropy for example the following holds:

$$E_{\mathrm{cryst}}^{\mathrm{uniaxial}} = K_0 + K_1\mathrm{sin}^2\theta + K_2\mathrm{sin}^4\theta + ... \tag{2.4}$$

Typical systems exhibiting uniaxial anisotropy are hexagonal or tetragonal lattices where there is only one high-symmetry axis (the c-direction).

The magnetic anisotropy increases progressively while reducing the system's dimension. K_1 is usually larger for a monolayer compared to bulk. Typical values of K_1 for bulk $3d$ metals are $K_1 = 4.8 \cdot 10^4$ J/m^3 (2.4 μeV/atom) for Fe, $K_1 = 4.1 \cdot 10^5$ J/m^3 (45 μeV/atom) for Co, and $K_1 = -5.5 \cdot 10^3$ J/m^3 (-0.3 μeV/atom) for Ni [16]. On the other hand, for objects of reduced dimension like single layers of atoms, chains of atoms or even single atoms at surfaces the order of magnitude of the magnetic anisotropy is in the meV/atom range, and it can be as high as 10 meV/atom for Co/Pt(111) [17].

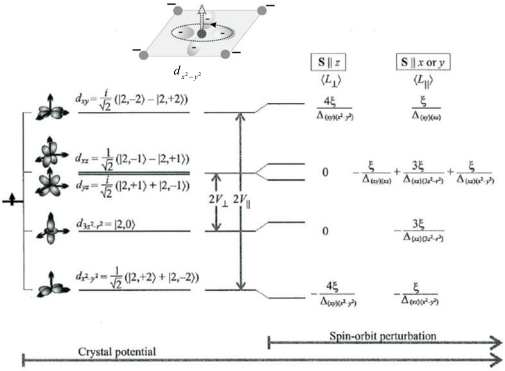
$d_{x^2-y^2}$
S ∥ z
⟨L⊥⟩
S ∥ x or y
⟨L∥⟩
$d_{xy} = \frac{i}{\sqrt{2}}(|2,-2\rangle - |2,+2\rangle)$
$d_{xz} = \frac{1}{\sqrt{2}}(|2,-1\rangle - |2,+1\rangle)$
$d_{yz} = \frac{i}{\sqrt{2}}(|2,+1\rangle + |2,-1\rangle)$
$d_{3z^2-r^2} = |2,0\rangle$
$d_{x^2-y^2} = \frac{1}{\sqrt{2}}(|2,+2\rangle + |2,-2\rangle)$
2V⊥
2V∥
$\frac{4\xi}{\Delta_{(xy)(x^2-y^2)}}$
$\frac{\xi}{\Delta_{(xy)(xz)}}$
0
$-\frac{\xi}{\Delta_{(xy)(xz)}} + \frac{3\xi}{\Delta_{(xz)(3z^2-r^2)}} + \frac{\xi}{\Delta_{(xz)(x^2-y^2)}}$
0
$-\frac{3\xi}{\Delta_{(xz)(3z^2-r^2)}}$
$-\frac{4\xi}{\Delta_{(xy)(x^2-y^2)}}$
$-\frac{\xi}{\Delta_{(xz)(x^2-y^2)}}$
Spin-orbit perturbation
Crystal potential

Figure 2.2: d-levels crystal field splitting in a square planar environment (left) and effect of the spin-orbit interaction calculated as a perturbation to the system (right). Adapted from [18].

In the previous paragraph a reduced degree of atomic coordination in nano-structures has been shown to lead to a higher spin magnetic moment μ_S, and it was announced in the introduction that the same increase occurs for the orbital moment μ_L. In the following the spin-orbit interaction term is explained, which is responsible for the formation of orbital moments and also triggers the development of the MCA.

Let's start by describing the microscopic origin of the magnetic anisotropy. The main contributions to magnetic anisotropy in nano-scale objects are the classic dipole-dipole interaction and the spin-orbit coupling. Magnetostriction, due to the influence between magnetic and elastic properties of a material, is in general more a bulk property and therefore it will not be treated here. The dipole-dipole interaction involves the magneto-static interaction between atomic magnetic moments. Since it depends on the shape of the magnet it is also called shape anisotropy. It has a classical macroscopic analogue: bar-magnets spontaneously orient themselves such that the north-pole of the first one is facing the south pole of the second one, to form a chain. Thus, in case of a chain of single atoms the shape anisotropy would lead to an easy axis along the chain axis. In case of a thin film instead the shape anisotropy gives an in-plane easy axis.

The spin-orbit coupling term is a relativistic correction to the Hamiltonian written as: $\widehat{H}_{\mathrm{SO}} = \xi\boldsymbol{\sigma}\cdot\mathbf{L}$. It connects the spin space $\boldsymbol{\sigma}$ with the lattice $\mathbf{r}$, represented by the orbital moment operator $\mathbf{L}$. $\boldsymbol{\sigma}$ is a matrix containing the Pauli matrices and ξ is the spin-orbit coupling constant. The importance of $\widehat{H}_{\mathrm{SO}}$ depends on both the spin-orbit coupling constant and the magnitude of the orbital moment. The former is element dependent whereas the latter strongly depends on the local environment of the atom and the configuration of bonding involved. For example, in bulk materials the orbital moment for $3d$ electrons is 'quenched', in the sense that the orbital motion of the electrons is suppressed due to the confinement to directional bonds between neighbor atoms (crystal field effect). In these conditions under the influence of the crystal potential combinations of the d orbitals are formed as eigenstates with a vanishing orbital moment. A simple explanation of this effect starts with the consideration that the crystal-field Hamiltonian can be expressed as a real function. Therefore it must have real eigenvalues. For example the crystal field in octahedral environment is proportional to the real function $x^4 + y^4 + z^4 - \frac{3}{5}r^4 + \ldots$. Now, the orbital moment operator $\widehat{L} = -i\widehat{r} \times \nabla$ is Hermitian and therefore must have real eigenvalues, even though it is purely imaginary. It follows that for a non-degenerate ground state $|0\rangle$ we have $\langle 0|\widehat{L}|0\rangle = 0$, since it has to be at the same time imaginary and real.

Since this work is about nano-structures on surfaces, the example of one atom bonded to four other atoms in a planar geometry as shown in Fig. 2.2 will be discussed in the following. In particular, this example will be useful to discuss the magnetic anisotropy of a monolayer of atoms.

The z axis, perpendicular to the plane of the four atoms, is taken as the quantization axis of the system. Each of the four atoms is represented by a negative charge placed in the $x - y$ plane, at an angle of 45° from the x and y axes (see Fig. 2.2). Near the corners of the square, the electron in the d orbital of the center atom will experience a Coulomb repulsion. The in-plane orbital $d_{x^2-y^2}$ formed by the linear combination of the two d eigenstates with $l = 2$ and $m_l = \pm 2$ is the one with the lowest energy, since it minimizes the overlap with the neighboring charges (see orbitals in Fig. 2.2). On the other hand, the d_{xy} orbital, with the lobes pointing in the direction as the negative charges, has the highest energy. An intermediate situation is obtained for the out of plane orbitals. All these linear combinations arising from first order perturbation theory due to the crystal potential have orbital moments equal zero (left part of Fig. 2.2). On the other hand, if the spin-orbit coupling term is present, it will counteract this quenching leading to non-vanishing orbital moments. The spin-orbit interaction in fact, differently from the crystal field operators, mixes in states with non-zero angular momentum. The expectation value of the orbital moment operator $\widehat{L}$ in presence of spin-orbit coupling in second order perturbation theory is written as:

$$\langle\widehat{L}\rangle = \sum_{i,j} \frac{\langle\psi_i|\widehat{L}|\psi_j\rangle\langle\psi_j|\widehat{H}_{\mathrm{SO}}|\psi_i\rangle}{\epsilon_i - \epsilon_j} f(\epsilon_i)[1 - f(\epsilon_j)] \tag{2.5}$$

where f is the Fermi function and $\psi_{i,j}$ are the unperturbed wave-functions of the system. Since spin and orbital coordinates are connected via $\widehat{H}_{\mathrm{SO}}$, the anisotropy of the orbital moment is reflected in the anisotropy of the magnetization of the system. The crystal lattice of the sample forces the magnetization to stay aligned in a specific direction along the crystal axis, and consequently forms a magneto-crystalline anisotropy energy. In presence of the spin-orbit interaction a second-order change in the energy ΔE_{SO} is found, which for $3d$ transition metals and neglecting spin-flip processes can be written as [19]:

$$\Delta E_{\mathrm{SO}} \approx -\frac{1}{4}\xi\widehat{S}[\langle\widehat{L}^{\downarrow}\rangle - \langle\widehat{L}^{\uparrow}\rangle]. \tag{2.6}$$

$< \widehat{L}^{\downarrow} >$ and $< \widehat{L}^{\uparrow} >$ are the expectation values of the orbital moment of the minority and majority spin sub-bands respectively. If the spin-up band is completely filled then ΔE_{SO} is proportional to the orbital moment and the MAE will be proportional to the difference in orbital moment in two different directions parallel and perpendicular to the surface [20]:

$$MAE = \frac{\xi}{4\mu_{\mathrm{B}}}[\langle\widehat{L}^{\parallel}\rangle - \langle\widehat{L}^{\perp}\rangle]. \tag{2.7}$$

The effects of the crystal field is in general strong for $3d$ elements, since here the orbitals are extended far away from the nucleus and the overlap between neighbor atoms is considerable. $4f$ orbitals instead, much less extended and positioned beneath the $5s$ and $5p$ shells, are largely unaffected by the crystal field and therefore the CF effects on rare earth elements are usually small. The spin-orbit term is predominant in this case. This behavior anyway can be very different from case to case, since the CF strongly depends on the ligands.

The above discussed planar symmetry case can be used to describe a simple square free-standing monolayer of d-metal atoms, following Stöhr [18]. For simplicity the majority d band is assumed to be filled. In a single electron picture the crystal field leads to a splitting of the atomic levels: taking the surface normal as the $\widehat{z}$ direction the two in-plane orbitals d_{xy} and $d_{x^2-y^2}$ will be separated by an energy $2V^{\parallel}$ and the out-of-plane orbitals d_{zx}, d_{yz} and d_{z^2} by $2V^{\perp}$ (see Fig. 2.2). In the simple case of a Co free standing monolayer with half filled minority band, the splitting will be symmetric around the Fermi level. In a band-picture the splitting has to be replaced by a bandwidth. The orbital moment can be calculated using perturbation theory, leading to [18]:

$$\langle \widehat{L}^{\parallel} \rangle = \frac{\xi \mu_{\mathrm{B}}}{2V^{\parallel}} (\frac{3}{R} + \frac{2}{R+1}); \langle \widehat{L}^{\perp} \rangle = 4 \frac{\xi \mu_{\mathrm{B}}}{2V^{\parallel}}, \tag{2.8}$$

with $R = \frac{V^{\perp}}{V^{\parallel}}$. This result shows how the in-plane moment depends on both the splitting of in-plane and out-of-plane orbitals, whereas the out-of-plane moment only depends on the amount of the in-plane crystal field. The higher the in-plane splitting $2V^{\parallel}$, the stronger the quenching of the out-of-plane orbital moment. This last one is indeed connected with the motion of electrons in the plane, which means hopping between d_{xy} and $d_{x^2-y^2}$ orbitals. When the energetic separation between the two levels is large, the hopping is inhibited. For the MAE one obtains:

$$MAE = \frac{\xi}{4\mu_{\mathrm{B}}} [\langle \widehat{L}^{\parallel} \rangle - \langle \widehat{L}^{\perp} \rangle] = \frac{\xi^2}{8V^{\parallel}} (\frac{3}{R} + \frac{2}{R+1} - 4). \tag{2.9}$$

This equation expresses that depending on R the easy axis is either in-plane ($R < 1$) or out-of-plane ($R > 1$). The value of R depends on the geometry and local arrangement. A free standing monolayer has $R < 1$, and indeed experimentally the easy axis for a Co monolayer supported on a non-magnetic and on a weakly interacting substrate (for example epitaxial Co thin films on Cu(001) [21]) is in-plane. Instead for a Co monolayer intercalated between two Pt layers $R < 1$ which leads to an out-of-plane easy axis (see for example [22]). In addition if the substrate supporting the monolayer is magnetically polarizable (e.g. a small magnetic moment can be induced on the substrate by the magnetic atoms) and has a high nuclear mass like in the case of Pt, then the spin-orbit constant will be large and consequently also the MAE. This means that in some cases the magnetic atoms show a magnetic anisotropy that is induced by the MAE of the substrate. An example is the Fe monolayer that shows in-plane anisotropy on W(110) [23] and out-of-plane anisotropy on Mo(110) (shown for monolayer and double layer height Fe islands [24, 25]). To complicate the picture, one has to remember that in nanostructures relaxation and reconstruction effects occur, which can strongly modify the electronic structure and therefore the MAE. The above considerations show that, as in the case of the magnetization values analyzed in the previous paragraph, also for the MAE the contribution from atoms at the surface can be very different from the bulk. For these reasons an empirical expression is often used for the anisotropy constant, in which the surface and volume anisotropy constants K^V and K^S are separated:

$$K^{\mathrm{eff}} = K^V + \frac{2K^S}{t}. \tag{2.10}$$

Here the surface term is weighted with the thickness of the film t.
For a more extensive treatment of the topic see Ref. [15, 26, 27].

2.2 Single domain nano-particles: superparamagnetism

Ensembles of atoms at the nano-scale are subdivided in two categories, depending on the way the system reacts to adding another atom: clusters and particles. For a cluster 'every atom counts' since an additional atom changes dramatically the system properties (non-scalable regime). These systems are made from a very small number of atoms and their study is interesting since it reveals the role of orbital moment and magnetic anisotropy at the atomic scale, in the way seen in the previous paragraph.

In this paragraph instead a few properties of nano-particles will be recalled. They are objects still in the nano-scale but containing a higher number of atoms as compared to a cluster. For a nano-particle new atoms only slightly affect the system, and important parameters as the Curie temperature have a monotonous dependence on the number of atoms (scalable regime). Nano-particles made from a ferromagnetic material have the special property to consist of a single domain of the magnetization if they are smaller then a critical size. In bulk materials the formation of domains with opposite magnetization saves the energy associated with dipolar fields. Each domain created, however, costs some energy, related to the build-up of the domain wall. When the sample size is reduced, energies scaling with the domain wall surface like the domain wall energy become progressively costly in comparison with volume energies, like the demagnetization energy. The reason is that the former energies scale as the (sample size)^2 whereas the latter scale as (sample size)^3. Therefore there exists a critical dimension where it is energetically more favorable to have a single magnetization domain that behaves as a macrospin. This critical size can be calculated simply by comparing the energy of a single domain state and the energy due to the formation of a domain wall [27]. For a spherical particle with cubic anisotropy, and assuming a 90° domain wall, the critical size is ∼100nm.

The direction of the magnetization in this case is determined by an eventual external magnetic field and by internal forces e.g. due to the magnetic anisotropy. The magnetization **M** of the macrospin is assumed to coherently rotate, for simplicity within a particular plane. This allows to restrict the calculations into a 2D coordinate system defined by the plane, where the polar angle θ is taken as the angle between the magnetization and the easy axis direction, usually chosen as the z axis. Uniaxial anisotropy is also assumed, originating either from shape or from magneto-crystalline anisotropy and quantified by the constant K. The magnetic anisotropy energy per volume expressed generically as E_{anis} is then given by:

$$E_{\mathrm{anis}} = K\mathrm{sin}^2\theta^1 \tag{2.11}$$

For $K > 0$ this function has minima for both $\theta = 0°$ and $\theta = 180°$, that corresponds to magnetization states parallel and anti-parallel to the z axis (see Fig. 2.3). The potential energy arising from this Hamiltonian is a double well potential, as found for single molecule magnets (SMMs, see Ref. [28]) like Mn12ac. The difference is that in the latter case the energy is quantized and has therefore discrete levels. In the case of a single domain particle instead the z component of the spin moment ($S_z = |S|\mathrm{cos}\theta$) and the energy are continuous variables, since the system is formed by several thousands of atoms forming the macrospin. Instead of well-separated energy levels energy bands are found. The energy barrier ΔE is the total magnetic anisotropy for a given particle of volume V. It is given by the product of the volume V and the difference between the maximum and the minimum value of the energy density $\Delta E_{\mathrm{anis}} = E_{\mathrm{anis}}(\theta = 90°) - E_{\mathrm{anis}}(\theta = 0°)$:

$$\Delta E = V \cdot \Delta E_{\mathrm{anis}} = V \cdot K. \tag{2.12}$$

The energy barrier has to be compared with the thermal energy $k_{\mathrm{B}}T$, where k_{B} is the Boltzmann's constant, in order to verify the stability of the magnetization along a certain direction. If $\Delta E \ll k_{\mathrm{B}}T$, then thermal energy causes the system's magnetization to continuously fluctuate over the barrier ΔE. This phenomenon is called *superparamagnetism.*

Under intermediate conditions changes of the orientation occur on time scales comparable with the time of a measurement. The fluctuation can be

---

[1] In the more general case this expression becomes $E_{\mathrm{anis}} = K \cdot (\mathrm{cos}\theta_0\mathrm{sin}\theta\mathrm{cos}\phi + \mathrm{sin}\theta_0\mathrm{cos}\theta)^2$, where θ and ϕ are polar and azimuthal angles and θ_0 is the angle between the easy axis and the z axis.

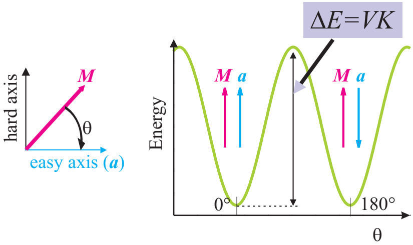

Figure 2.3: Double-well potential of a nano-particle with uniaxial anisotropy along the z direction.

measured if the system is first prepared in a specific magnetization state by applying a magnetic field parallel or anti-parallel to the z axis. When the field is removed, one can record the relaxation of the magnetization as a function of time: $M(t) = M(t = 0) \cdot e^{-t/\tau}$. The period of the fluctuation τ, or relaxation time, is given by the Arrhenius Ansatz $\tau = \tau_0 \exp(\Delta E/k_{\mathrm{B}}T)$, where τ_0 is a time scale characteristic of the material with typical values of $10^{-9} - 10^{-10}$ seconds.
An important parameter to consider now is the characteristic measuring time of the experiment, τ_m, corresponding to the time to take one measurement of the magnetization in the specific experiment. In the previous considerations τ_m has been considered much smaller than the relaxation time, which is often not the case in real experiments. In this case the stability of the magnetization comes to depend on how fast the magnetization itself is measured. A critical temperature T_{B} called the *blocking* temperature can be defined, at which the characteristic measuring time τ_m equals the relaxation time τ. From the relation:

$$\tau_m = \tau = \tau_0 \exp(\Delta E/k_{\mathrm{B}}T) \tag{2.13}$$

one obtains:

$$T_{\mathrm{B}} = \frac{V \cdot \Delta E_{\mathrm{anis}}}{k_{\mathrm{B}} \ln(\tau_m/\tau_0)} \tag{2.14}$$

For typical values of $\tau_0 = 10^{-10}$s,$\tau_m = 60$s, Eq. 2.14 becomes:

$$T_{\mathrm{B}} = \frac{V \cdot \Delta E_{\mathrm{anis}}}{27 k_{\mathrm{B}}} \tag{2.15}$$

Below T_{B} the macrospins, or spin blocks, are frozen out. T_{B} therefore represents the superparamagnetic limit for a stable magnetization and is therefore a very important parameter for magnetic storage data devices.

Anticipating a result that will be shown in the experimental chapter, one can estimate what would be the critical size for a Co nano-particle on Pt(111), at room temperature, assuming a magnetic anisotropy value of about 0.2meV/atom. This magnetic anisotropy energy is found by *ab-initio* calculations as shown in Section 4.2.3. The following typical parameters can be used: $\tau_0 \approx 10^{-10}$s, $k_{\mathrm{B}}T = 25$meV, and $\Delta E \approx N \cdot 0.2$meV, where N is the number of atoms of the nanoparticle. The requirement of a long term stability of 10 years, corresponding to $\tau = 3 \cdot 10^8$s, leads to a number of atoms of $N \approx 5000$. Assembling such a number of atoms to form a cubic nano-structure would lead to an edge length of about 10nm. This last size is equivalent to a storage density of about 6500 Gigabits/inch^2, a factor of 20 better then today's hard disks that have a capacity still below 400 Gigabits.

Finally, in the presence of an external magnetic field the magnetization **M** of a superparamagnet tends to align with the magnetic field. Above the blocking temperature, the system can be treated as a paramagnet with the macrospin which scales with N and with a magnetic energy $E(\theta, \phi) = N(E_{\mathrm{Zeeman}} + E_{\mathrm{anis}})$ given by the Zeeman term plus the magnetic anisotropy energy of Eq. 2.11. In the canonic ensemble, the expectation value of the total magnetization of a nano-particle along the direction of the magnetic field $< M_z >$ is given by:

$$< M_z >= N < \mu_z >= \overline{\mu} N \frac{\int_0^{2\pi} d\phi \int_0^{\pi} d\theta \sin\theta \cos\theta e^{-\frac{E}{k_{\mathrm{B}}T}}}{\int_0^{2\pi} d\phi \int_0^{\pi} d\theta \sin\theta e^{-\frac{E}{k_{\mathrm{B}}T}}} \tag{2.16}$$

Here $\overline{\mu}$ is the magnetic moment per atom at the saturation, averaged within all the atoms in the nano-particle and μ_z is the component of the magnetic moment along the z direction, θ and ϕ are polar and azimuthal coordinates. This equation can be used to fit the measured hysteresis loops of the system, and it allows to extract the magnetic anisotropy energy of the nano-particle ΔE_{anis} from measurements done along the easy and hard axis. It will be used in Section 4.2. For more information about the topic of superparamagnetism see Ref. [15, 27].

The magnetic response of isolated $3d$ metal nano-clusters is known to be superparamagnetic in a wide temperature range, which is disadvantageous for applications. Furthermore, a key issue in information technology is to increase the areal storage density of computer hard disks (by means of thin magnetic films it has already increased by many orders of magnitude in recent decades [29–31]. Future progress could be based on nanoscale monodisperse and aligned magnetic units, densely packed into an ordered monolayer and with stable remanent magnetization at room temperature, accessible switching fields, and negligible interactions [31]. This requires the fabrication of particles with approximately 3 nm diameter as they exhibit a stable magnetization direction at room temperature of typical hard magnetic materials with magnetic anisotropy $K_1 = 5\text{MJ/m}^3$ [32]. The magnetization of smaller particles would be thermally unstable, whereas bigger particles would lead to a waste of areal density.

Stabilization of magnetic moments can be achieved introducing magnetic anisotropies by exploiting the directionality of chemical bond or the breaking of symmetry in a non-free environment: namely bringing the clusters in contact with a surface, as we have seen in the previous paragraph or capping the clusters with special materials. The latter approach prevents oxidation and at the same time enables the interaction of the magnetic clusters with and via a surrounding matrix. This will be the topic addressed by the experiments shown in Section 4.4.

Chapter 3

Experimental techniques

In this chapter a concise description of the experimental methods used in this thesis is given. The first section deals with scanning tunneling microscopy (STM) and gives information about both the theoretical basis of the technique and technical aspects. The second section explains the principles of the X-ray techniques performed at the ESRF (European Synchrotron Radiation Facility) in Grenoble and at BESSY (Berliner Elektronen-Speicherring Gesellschaft für Synchrotronstrahlung) in Berlin. These techniques are based on X-ray absorption (XAS and XMCD), scattering (GISAXS) and diffraction (GIXRD). In the case of X-ray techniques the focus is on the information achievable by the methods, and less on the technical realization.

3.1 Scanning tunneling microscopy

3.1.1 Principles and theory

The first scanning tunneling microscope (STM) was built by Binnig and Rohrer [33] in 1982. It is used to reveal the morphology of a surface at the atomic level and/or the density of states around the Fermi level. It is based on the quantum tunneling effect occurring between two metals (electrodes) separated by a thin potential barrier, a region where the potential energy of the electron U is higher then its total energy E. The spatial extension of the wavefunction of the two electrodes and their overlap allows for electrons to transfer from one electrode to the other, a process which is forbidden in classical physics. If a potential is applied across the barrier a net flow of electrons can occur, the tunneling current I (also indicated as I_{Tunnel} in the text).

Only in few special cases the Schrödinger equation for the system has analytic solutions, one of these is the square potential barrier. This over-simplified model can be used as the first step to understand the basic idea of STM. Here the two metals are the tip and sample, and the tunneling barrier is the vacuum between them (one-dimensional metal-vacuum-metal tunneling junction, Fig. 3.1 (c)). The distance between tip and sample is only a few Ångströms which generates a finite tunneling conductance between the two. The transmission coefficient T, defined as the ratio between the tunneling current $I(z)$ that arrives at the second electrode at distance z from the first one normalized by the impinging current $I(0)$ at $z = 0$.:

$$T = \frac{I(z)}{I(0)} = e^{-2kz} \tag{3.1}$$

where

$$k = \frac{\sqrt{2m_e\phi}}{\hbar} \tag{3.2}$$

is the decay constant of a state from the 1st electrode near the Fermi level in the region of the barrier, in the approximation that the bias is much smaller then the value of the work function ϕ of the first electrode. m_e is the electron mass (see Fig. 3.1 (a)). The tunneling effect is therefore decaying exponentially as the barrier width increases. This exponential law is very important in STM: it expresses that a small variation in z leads to large variations of T and therefore, as will be shown later, of the tunneling current I. The transmission coefficient in the case of general potential barriers can be calculated starting from a semi-classic approach, the Wentzel-Kramers-Brillouin (WKB) approximation.

In the presence of a voltage difference between the two electrodes, a finite tunneling current will flow. This is converted into a voltage and then amplified and filtered (see scheme in Fig. 3.1 (b)). The topographic images in STM are obtained by scanning the tip over the sample at a fixed current (constant current mode) or fixed tip-sample distance (constant height mode). The lateral position of the tip with respect to the surface and the tip-sample distance are controlled by piezoelectric (x,y,z) motion. In the constant current mode, used in this work, an electronic feedback compares the tunneling current to a reference value (the set-point current) and the difference between the two is used to regulate the scan piezo (z). The values of z at each (x,y) position are stored by the software and form the contour plot of the substrate by conversion in grey-scale.

The system sample+tip+tunneling barrier can be schematized as an electric circuit where a resistance is in parallel with a capacitance resulting from the vacuum dielectric constant ϵ_0 (see Fig. 3.1 (b)). Typical parameters for

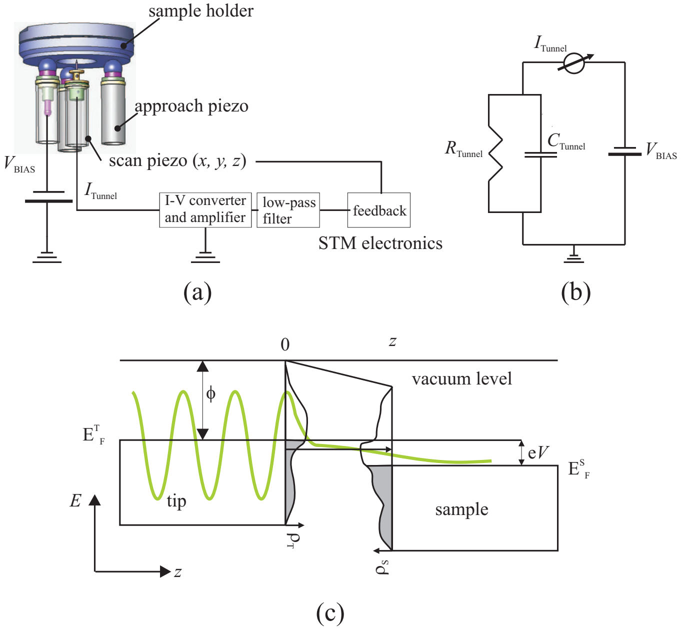
sample holder
approach piezo
scan piezo (x, y, z)
V_BIAS
I_Tunnel
I-V converter and amplifier
low-pass filter
feedback
STM electronics
(a)
I_Tunnel
R_Tunnel
C_Tunnel
V_BIAS
(b)
0
z
vacuum level
ϕ
E^T_F
eV
E^S_F
E
tip
sample
ρ_T
ρ_S
z
(c)

Figure 3.1: (a): scheme of the main components of an STM; (b) equivalent circuit for the metal-vacuum-metal tunneling junction; (c) corresponding potential energy diagram.

tunneling are a current of 1nA at a bias voltage of 1V, that gives a tunneling resistance in the GΩ range.

STM requires conductive or semi-conductive samples and atomically ’flat’ surfaces. It can be performed both in air and in UHV conditions. In the next sub-paragraphs some of the basic equations that can be used to extract quantitative information from the acquired images are recalled, following Chen [34].

Bardeen formula for the tunneling current

The Bardeen model [35] describes metal-insulator-metal tunneling junctions. Tersoff and Hamannn have applied it to calculate an equation for the tunneling current in STM [36,37], in the approximation that the two metals are

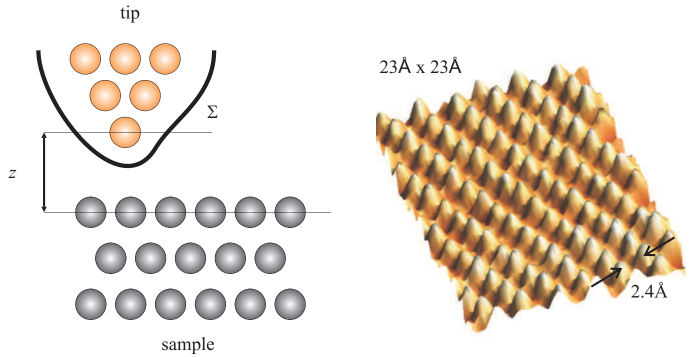

Figure 3.2: Model to describe the system tip + sample in the Bardeen tunneling theory, with a separation surface Σ drawn between the two. In the right side, a topography of a graphite sample surface taken in the home-built STM that shows atomic resolution is presented in 3D perspective.

tip and sample, and the insulator in between is the vacuum. As a first step the two sub-systems tip+vacuum and vacuum+sample are treated independently from each other and the Schrödinger equation is used to calculate the eigenstates. The second step is to use time dependent perturbation theory to calculate the rate of transfer of one electron from one sub-system to the other, due to the overlap of the wave-functions. In a last step the tunneling current is calculated.

The probability of an electron in the sample state Ψ with energy E_Ψ to tunnel to a state tip state χ with energy E_χ is given, in first order perturbation theory by the *Fermi's golden rule*:

$$w_{\Psi\to\chi} = \frac{2\pi}{\hbar}|M|^2\delta(E_\chi - E_\Psi), \tag{3.3}$$

where M is the tunneling matrix element or the amplitude of electron transfer, that is determined by the overlap of the surface wavefunctions of the two sub-systems at a separation surface Σ between the two (the choice of Σ does not affect the calculation). Bardeen has found the following formula:

$$M = -\frac{\hbar^2}{2m_e}\int\limits_\Sigma (\chi^*\nabla\psi - \psi\nabla\chi^*)\cdot d\boldsymbol{S}.$$

By summing over all the states in the tip and the sample and taking into account the occupation probabilities (Fermi distribution for both tip and sample) the tunneling current I in presence of a bias voltage can be calculated. Assuming $k_{\mathrm{B}}T$ much smaller than the energy resolution required in the measurements (the Fermi distribution can then be approximated as a step function) one finds the following expression:

$$I \propto \int_{0}^{eV} \rho_S(E_{\mathrm{F}} - eV + \epsilon)\rho_T(E_{\mathrm{F}} + \epsilon)|M|^2 d\epsilon \tag{3.4}$$

where ρ_S and ρ_T are the density of states (DOS) of the sample and of the tip, respectively and E_{F} is the Fermi energy. The tunneling current therefore depends on the convolution of the DOS of the tip and sample and on the tunneling matrix element $|M|$. The explicit expression of the tunneling matrix elements requires the knowledge of tip and sample wavefunctions. Tip wavefunctions are usually calculated based on the spherical-harmonic expansion in the gap region. A first approximation is the s-wave model, presented in the next paragraph. In the case that $|M|$ can be considered as constant in the interval of interest and the tip has a constant DOS (free-electron metal tip) then the tunneling conductance is proportional to the DOS of the sample:

$$\frac{dI}{dV} \propto \rho_S(E_{\mathrm{F}} - eV).$$

S-wave model and corrugation function

The s-wave tip model was developed by Tersoff and Hamann [36, 37, 39] at the beginning of the 80s, in coincidence with the earliest development of STM after its invention. It gives an estimation of the tunneling current and the corrugation function for a tip with radius of curvature R, assuming an s-wave tip wave function. This implies that the solutions of the Schrödinger equation for a spherical potential are taken as the tip wavefunctions. Under these assumptions, the tunneling current at very low bias is given by the following formula:

$$I \propto \sum_{E_{\mathrm{F}}-eV}^{E_{\mathrm{F}}} |\Psi(\mathbf{r}_0)|^2 = eV\rho_S(\mathbf{r}_0, E_{\mathrm{F}}) \tag{3.5}$$

Here $\rho_S(\mathbf{r}_0, E_{\mathrm{F}})$ is the sample Fermi-level local density of states (LDOS) at the center of curvature of the tip $\mathbf{r}_0$. A constant current STM image therefore is, in the s-wave model, a Fermi-level LDOS contour of the surface taken at the center of curvature of the tip. In other words form Eq. 3.5 one sees that in the s-wave model the tunneling current only reflects the properties

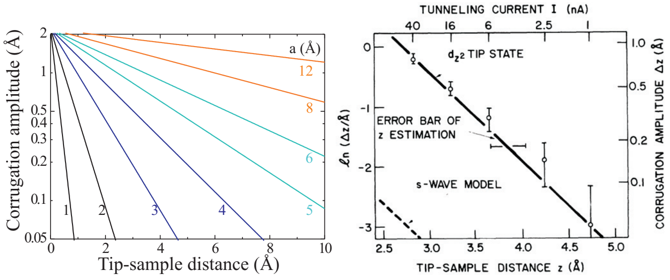

(a) (b)

Figure 3.3: Corrugation amplitudes as a function of the tip-sample distance z: (a) the case of Au(110) surface ($k \approx 11.4\text{nm}^{-1}$) for several value of the periodicity a; (b) the Al(111) surface according to the s-wave model and for d_{z^2} tip state, from [38].

of the sample, and not of the tip. In case of a free-electron metal sample, the STM image is the charge density contour, since the LDOS contour at a certain distance from the sample almost coincides with the contour of the total electron density.

It is now very important to evaluate under which conditions the s-wave model is valid. Tersoff and Hamann made an estimation of the effect of non-s-wave tip states [36, 37] on the tip wavefunction, and found that this is negligible when the following condition holds:

$$(1 + \frac{q^2}{k^2})^{\frac{l}{2}} \simeq 1. \tag{3.6}$$

Here l is the angular momentum of the tip wave function and $\mathbf{q} = (k_x, k_y)$. $\mathbf{q}$ is connected to the feature size a of the sample by $|\mathbf{q}| = \frac{\pi}{a}$. From Eq. 3.6 it is evident that the effect of tip states with $l \neq 0$ can be neglected in the limit $\frac{\mathbf{q}^2}{k^2} \ll 1$, that is $a \gg \frac{\pi}{k}$. In the case of a metal, where the decay constant k is about 10nm^{-1}, one finds $\frac{\pi}{k} \cong 0.3$ nm, that represents the lowest value for the validity of the s - wave model.

In order to understand the STM images, it is useful to introduce the concept of *corrugation* of a surface. For a given bias the physical quantity measured by STM is the tunneling current $I(x, y, z)$, that is a function of the lateral position over the surface (x, y) and the tip-sample distance z. $I(x, y, z)$ can be decomposed in two parts, one part constant in (x, y), $I_0(z)$ and a second part varying with the position over the surface, $\Delta(x, y, z)$ or surface corrugation, much smaller then the first one:

$$I(x, y, z) = I_0(z) + \Delta I(x, y, z). \tag{3.7}$$

In the constant current mode of measurement one defines a corresponding corrugation amplitude $\Delta z(x, y)$ making the Ansatz $z(x, y) = z_0 + \Delta z(x, y)$ and substituting in Eq. 3.7, the condition of constant current ($I(x, y, z) = I_0(z_0)$) leads to the following expression:

$$\Delta z(x, y, z) = -\frac{\Delta I(x, y, z)}{dI_0(z)/dz}. \tag{3.8}$$

According to the above equation, the corrugation amplitude $\Delta z(x, y, z)$ can be calculated once the tunneling current I is known. In the s-wave model, Δz coincides with the corrugation amplitude of the Fermi-level DOS or of the charge density contour. For a metal with a one-dimensional periodicity a the following formula is found [37]:

$$\Delta z(x, z) \approx 2/k \exp[(-2(k^2 + \pi^2/a^2)^{1/2} - k)z] \tag{3.9}$$

The first important observation about this formula is that the corrugation amplitude decays exponentially with distance z. In Fig. 3.3(a) Eq.3.9 is plotted for the case of Au(110) ($k \approx 11.4\text{nm}^{-1}$) for several value of the periodicity a, as a function of the tip-sample distance z. For large a the corrugation amplitude is large and depends only weakly on z. For small a instead the corrugation amplitude is very small and almost undetectable at normal operation distances ($1 - 4$Å). Therefore the s-wave model doesn't explain the experimentally observed atomic resolution at atomic spacing of $2.5 - 3$Å. Thus, this must be due to other electronic states then the s states, that becomes important for values of a in the atomic distance range. Here in fact, as explained at the beginning of this paragraph, the s-wave model doesn't hold anymore. In the case of tip states other then s the tunneling process also depends on the surface density of states, according to Eq. 3.4.

The tunneling matrix elements are found to be enhanced [34] for non-s tip states. This corresponds to an enhancement of the tunneling current I since $I \approx |M|^2$. Thus, an enhancement of the corrugation amplitude is expected as compared to that of the charge-density contour according to Eq. 3.8. In Fig. 3.3 (b) one can see for example the comparison between the corrugation amplitudes for a d_{z^2} and an s tip state as calculated for the Al(111) surface [38]. In general, the d_{z^2} has the highest corrugation amplitude among the three orbitals. This is one of the reason why most of the commonly used tip materials are d-band metals, for example W, Pt and Ir.

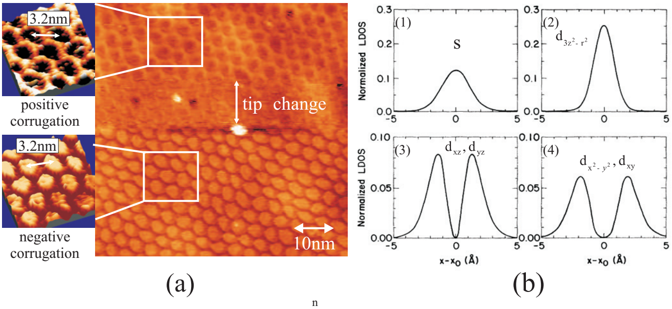

(a) (b)

Figure 3.4: (a): STM topography of the boron-nitride nanomesh showing a change of the tip with consequent change of the corrugation; (b): LDOS for different tip states, from [40]: (1) s state; (2) $l = 2$, $m = 0$ state ($d_{3z^2-r^2}$); (3) $l = 2$, $m = 1$ state (d_{xz} and d_{yz}); (4) $l = 2$, $m = 2$ state ($d_{x^2-y^2}$ and d_{xy}).

An interesting effect related to tip states is the inversion of contrast in STM images. In Fig. 3.4 a topography of the boron-nitride nanomesh is shown (see Section 3.3.3) where a change of the contrast occurred during scanning, due to a change of the tip: from positive (pits appear darker than the rim regions) in the upper part to negative (pits appear brighter than the rim regions) in the bottom part but with the same period of the hexagonal arrangement. This effect can be understood considering the shape of the LDOS of tip electronic states with different values of the magnetic quantum number m, as shown in Fig. 3.4 (c). Let's consider a d-state tip with axial symmetry (the two states with $m = 1$ - d_{xz} and d_{yz} - are degenerate. Also the two states with $m = 2$ - d_{xy} and $d_{x^2-y^2}$ - are degenerate) and a metal surface like e.g. Au constituted by atoms with only s-wave states near the Fermi level. Thus, the tunneling current distribution for a single Au atom is proportional to the tip LDOS (Eq. 3.5) and the total current distribution is the sum of the tunneling current for all the Au atoms at the surface. In the case of $m = 1$ and $m = 2$ tip states, the LDOS is ring-shaped, and therefore the tunneling current distribution should also be ring-shaped. It follows that with an $m \neq 0$ tip state, an inverted image is expected, where the sites of surface atoms are minima rather then maxima in the topographic images [41]. A double tip effect can be excluded if the lattice arrangement and periodicity in the normal and inverted image are the same.

Minimization of noise

STM requires a control over the tip-sample position with picometer precision, performed in the presence of various disturbances such as building vibrations, acoustic noise, temperature drift, as well as hysteresis and creep of the piezoelectric elements and finally electronic noise. These perturbations cause uncontrolled variations in tip-sample position at different time scales. Typically, buildings vibrate at frequencies up to 100Hz. These vibrations are excited e.g. by machines running at or near line frequency, and by the associated harmonics and sub-harmonics. Shear and bending vibrations usually resonate at frequencies between 15 and 25 Hz. Perturbations of a person walking in the laboratory are usually in the $1-3$ Hz range. Suppression of the influence of these external perturbations requires a high degree of stiffness and damping.

One can model the system STM + UHV chamber + external world as a vibrating system with one degree of freedom. The STM is represented by a mass m mounted to a frame through a spring of stiffness k (see Fig. 3.5). The frame has vibrations transmitted from the external world (ground and air) that will cause a displacement of the frame as a function of time along a certain space coordinate, *R(t)*. The problem of vibration isolation is then to minimize the vibration transferred to the mass, e.g. the displacement of the mass *r(t)*. From the solutions to Newton's equation for the mass in presence of damping one can calculate the transfer function F for the system [42]:

$$F := |\frac{r_0}{R_0}| = \frac{\sqrt{4\gamma^2\omega^6 + (\omega_0^4 - \omega_0^2\omega^2 + 4\gamma^2\omega^2)^2}}{(\omega_0^2 - \omega^2)^2 + 4\gamma^2\omega^2}. \tag{3.10}$$

r_0 and R_0 are the oscillation amplitudes for mass m and frame, ω_0 is the natural frequency of the system and γ is the damping constant. ω_0 is a function of the stretched length of the spring $\triangle l$:

$$\omega_0 = \sqrt{\frac{k}{m}} = \sqrt{\frac{g}{\triangle l}}. \tag{3.11}$$

An efficient vibration isolation corresponds to a small value of the transfer function. In Fig.3.5 the transfer function is shown for different values of ω_0 and γ . In case of zero damping ($\gamma = 0$) the isolation from vibrations is very efficient at high frequencies, but there are very large oscillations at the resonance frequency ($\omega = \omega_0$); the opposite behavior is observed for strong damping ($\gamma \gg \omega_0$), where the damping is very efficient at the resonance but not at high frequencies. The appropriate damping value is a compromise, and it depends on the system geometry.

In the present case the damping was realized in two stages: first a pneumatic

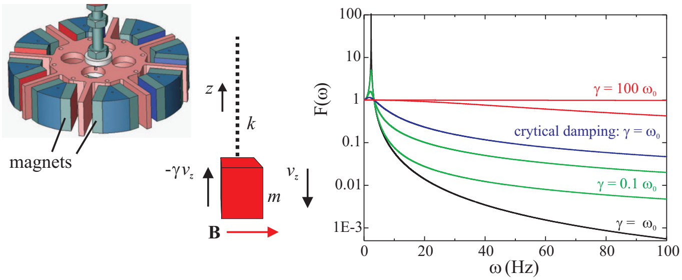

Figure 3.5: The eddy current damping system (left) and the transmission function for several values of damping, calculated for $\omega_0 = 2.4\text{Hz}$ (right).

active and passive damping of the full UHV chamber versus the floor and second an eddy current damping of the STM versus the chamber. The eddy-current system shown in Fig. 3.5 is based on the Lorentz force. When a conductive material is moving relative to a magnetic source such as a permanent magnet, the electrons inside the conductor circulate in orbits perpendicular to the magnetic field due to the Lorenz force. These circulating eddy currents will dissipate into heat, due to the resistivity of the conductor and cause a viscous damping process.

The damping force generated in the conductor for a rectangular body moving along the z direction with velocity $v_z(t)$ in presence of a magnet with circular shape is [43]:

$$F_z = -cv_z = -C_0 \frac{B^2 \pi a^2 t}{\rho} v_z \tag{3.12}$$

where πa^2 is the magnet surface area, B the magnetic field, t the body thickness, ρ the material resistivity and C_0 a constant depending on the relative dimensions of magnet and conductor. In the system used in this thesis the field is provided by strong Co-Sm (Sm2Co17, Peter Welter GmbH) magnets arranged in a circular structure (Fig. 3.5). The horizontal magnetic field between two magnets is about 200mT; in the vertical direction towards the STM the magnetic field drops to 7mT at a distance of 30mm from the magnets, that is less then half the sample-magnet distance. The natural frequency of the system STM on springs is $\omega_0 = 2.4\text{Hz}$ and the damping factor is $\gamma = \frac{c}{2m} = 0.5\text{Hz} = 0.2\omega_0$. In Fig. 3.5 the transfer function is shown that is obtained inserting this value in Eq. 3.10.

So far the influence of mechanical vibrations was discussed, while in many cases the electronic noise is the limiting factor for STM resolution. The tunneling current in STM is very small, typically between 0.01 and 10nA. A very careful grounding of the system components has to be assured in order to minimize electric noise and especially ground loops. A ground loop occurs when there is more than one ground connection path between two components of the electric equipment. The two ground paths form the equivalent of a loop antenna which picks up induced currents, due to the vicinity of varying magnetic fields (Faraday's law of induction). Resistances transform these currents into voltage fluctuations that modulate the potential of the 'real' signal carrying wires. The noise therefore becomes part of the signal. A ground loop will result as a disturbance in the signal cables (a typical hum), appearing with the frequency of the electric network (the time varying magnetic field), typically 50Hz or 100Hz. As an example in the STM set-up used in this work an improper grounding could lead to 100mV noise amplitudes at amplifier gain of 10^9 V/A. The goal is of course to minimize this disturbance and to reduce the resulting noise in the z channel to only a few picometers.

3.1.2 The home-made VT-STM

The existing UHV system was built during the time of the previous PhD students Peterka [44], [45] and Repetto [46]. The present thesis was focused on the implementation of a homemade Variable-Temperature Scanning Tunneling Microscopy (VT-STM) system, described in the following. In the final stage of this thesis the UHV chamber consisted of a preparation chamber, a VT-STM chamber and a magnetism chamber for Magneto Optical Kerr Effect (MOKE) measurements. The preparation chamber is equipped with surface analysis tools such as Low Energy Electron Diffraction (LEED) for surface structure investigations and Auger Electron Spectrometry (AES) for chemical characterization of the samples. Omicron evaporators are used for Molecular Beam Epitaxy (MBE) and a quartz micro-balance is available to calibrate the deposition rate. The magnetism chamber allows to measure the magnetization of samples using MOKE or Kerr microscopy. For *3d* metals on surfaces the coverages have to be $\theta \sim$ 1ML or larger in order to get magnetic contrast with these techniques.

The samples can be transferred *in-situ* between the different experiments by means of a long manipulator with far reach and a rotating wobble-stick. The latter is used to transfer sample holders and tip holders from the manipulator (where the sample/tips get prepared) to the VT-STM chamber. The cold sample can be transferred with the wobble stick from the manipulator to the cold STM in a short time (less then 1 minute), during which the sample stays below 100K. Operation temperatures of the sample in the manipulator

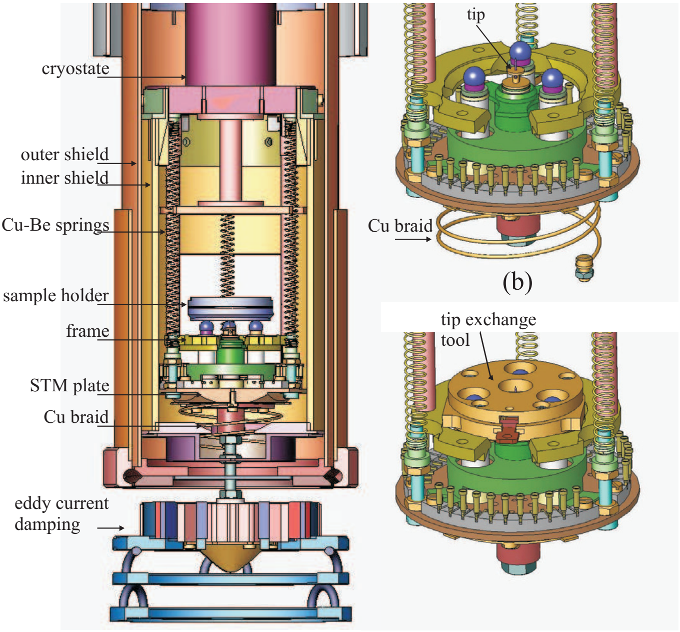
cryostate
outer shield
inner shield
Cu-Be springs
sample holder
frame
STM plate
Cu braid
eddy current
damping
tip
Cu braid
(b)
tip exchange
tool

(a) (c)

Figure 3.6: Drawings of the VT-STM: (a) cross sectional view of the STM with the cryostat, the cryogenic shields, the STM unit hanging on the springs and the eddy current damping; (b) the VT-STM head with the thermal anchoring braids; (c) the tip-exchange tool.

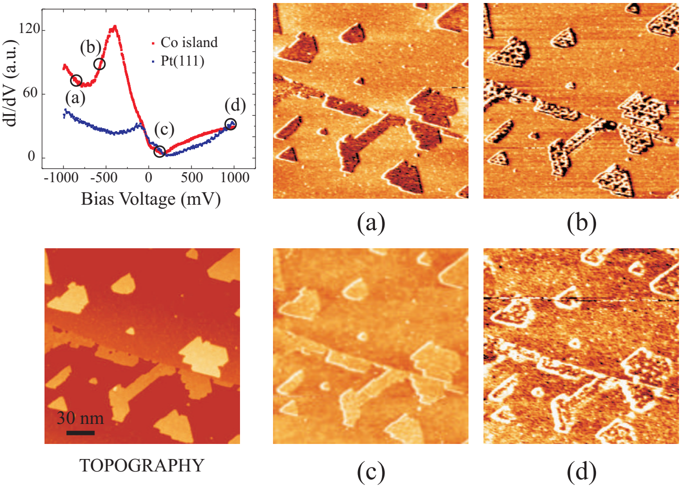

Figure 3.7: An example of STS measurements for Co monolayer islands on Pt(111): (top left) topography; (bottom left) dI/dV scan, showing the electronic structure of the Pt(111) surface and of a Co island/Pt(111), in agreement with what found in [47]; (a) - (d) dI/dV maps for several values of the bias voltage V_{BIAS} giving different structural contrast. In (b) for example dislocation lines in the Co layer are visible, due to the lattice mismatch of 9.4% between Pt and Co [47, 48].

are between 35K (Liquid Helium cooling) and 1200K (electron bombardment heating [46]). The crystal preparation procedure consist of Ar-sputtering followed by annealing cycles, and the cleanliness can be checked by Auger, LEED and STM measurements. The UHV in the chamber is obtained by a turbo-molecular pump backed by a rotary pump, an ion getter ionization pump, a Ti-sublimation pump and an H_2-getter pump. Pressures which are usually achieved are in the range of $2 \cdot 10^{-10}$mbar. A load-lock system allows the storage of five different sample/tip holders that can be inserted in the preparation chamber without breaking the vacuum. The load-lock is pumped independently with a small turbo pump. Two leak-valves allow the filling of the chamber with gases for adsorption experiments and sample sputtering.

The VT-STM is a home-made beetle type or Besocke STM [49] and the design is based on Wilson Ho [50]. The microscope is provided with a tip exchange mechanism that allows the removal of the tip for substitution and preparation. Variable temperature measurements between 20 and 300K are routinely performable. The cooling is provided by a helium flow cryostat. To reduce mechanical vibrations caused by the liquid He flow and by chamber vibrations, the cold plate of the cryostat is decoupled from the cryostat by three CuBe springs. The oscillations of the springs are damped by an eddy current damping system, shown in Fig. 3.6. Two concentric gold coated Oxygen free Cu radiation shields around the microscope prevent the heating of the sample by thermal radiation. A thermal anchoring of the STM plate to the internal shield is necessary to reach the temperature of 20K. It is obtained by three Cu braids each of them made out of about 4000 Oxygen free wires (Goodfellow) with diameter 40μm. This solution ensures on the one hand an efficient and fast cooling of the STM plate and on the other hand, that the light braids do not introduce extra mechanical coupling. In order to avoid external mechanical vibration (building, laboratory pumps) to propagate to the STM, the UHV chamber is damped by active and passive elements. The temperature is controlled by a thermal heater placed close to the cryostat. Temperature sensors (diodes) are placed at three different points of the STM: cryostat, frame and STM plate (Fig.3.6). The time required to cool down the sample in the STM from RT to 20K and start measurements is about 2 hours. This includes a long waiting time until thermal drifts have vanished.

A big effort has been done to minimize the electronic noise in the tunneling current. Especially the grounding and the decoupling of the system from the electric network ground appeared to be very important to minimize ground loops and therefore 50 and 150Hz noise. In the final configuration we have the chamber decoupled from the network ground, and the electronics of the STM powered through a separation-transformer. The final performances of the microscope are at RT a noise level in the z direction below 5pm and stable conditions (low drift) at 20K to perform spectroscopy measurements as shown in Fig.3.7.

dI/dV measurements are performed by means of a lock-in technique: a small AC signal V' is added to the bias V_{BIAS} and the resulting current is read by the lock-in (input signal). Here it is multiplied by a reference signal (usually the same V') and transformed to a DC signal. Finally the output of the dual lock-in amplifier ((x,y) or (R,θ) mode) is recorded by the STM electronics as a function of V_{BIAS}. The x channel is in fact proportional to dI/dV at correct phase settings. Due to the AC nature of the additional bias, one has to consider that the current will contain not only the tunneling part I_{Tunnel} but also a capacitive component I_{C} (with complex impedance given by $Z = \frac{1}{jwC}$, see Fig. 3.1 (c)) that is shifted of 90 degrees as compared to V'. The I_{Tunnel} signal is instead in phase with V'. The phase of the reference signal is chosen such that it minimizes the capacitive component of the input signal. This is

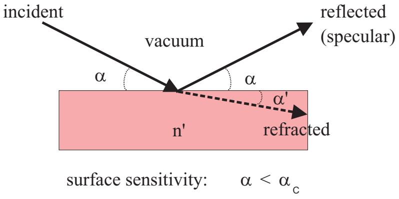

Figure 3.8: X-ray reflection and refraction.

done out of tunneling, where only I_{C} is present. At correct phase settings the signal at the y channel has to be very small, since this is proportional to I_{C}.

3.2 Synchrotron X-ray techniques

This chapter describes the X-ray techniques that are used in the thesis: (a) surface diffraction and scattering and (b) X-ray absorption spectroscopy (XAS) and X-ray magnetic circular dichroism (XMCD). These techniques give information about the ordering of the surface at the atomic and at the nanoscale and about the average magnetization. Differently to STM though the X-ray techniques used here are spatially integrated, i.e. the detected signal is averaged over a relatively large area/volume of the sample given by the beam spot size of the radiation used.

3.2.1 Surface scattering and diffraction

The techniques of Grazing Incidence Small Angle X-ray Scattering (GISAXS) and Grazing Incidence X-ray Diffraction (GIXRD) are important tools in surface science to investigate the average structural properties of samples at the atomic and nanometer scale.

Here an incident beam of X-ray photons is targeted onto a sample under an angle α, as shown in Fig. 3.8. The interaction between X-ray radiation and matter results in a reflected beam and a refracted one traveling inside the sample. The Bragg's law expresses that the constructive interference between light with wavelength λ scattered by adjacent crystal planes separated by the distance d occurs at wavelengths defined by the following relation :

$$2d \cdot \sin\alpha = n\lambda, \tag{3.13}$$

where n is an integer number. An important quantity in diffraction is the momentum transfer, defined as $\mathbf{q} = \mathbf{k}_f - \mathbf{k}_i$ ($\mathbf{k}_f$ and $\mathbf{k}_i$ are the final and initial wavevectors), since it defines the length scale at which we are observing the system. The *diffraction* range is reached at wide angles, when the inverse of the momentum transfer perpendicular to the surface ($q_\perp = \frac{4\pi}{\lambda} \sin\alpha$, with α being the scattering angle) is close to the interatomic distance. By the analysis of the integrated diffraction intensities, one can access the atomic structure.

The *diffuse scattering* range instead, located around Bragg peaks, gives information about the disorder in the studied system. Furthermore, for systems with periodicity d in the nanometer range, the corresponding variations of the electron density yield X-ray scattering at small momentum transfer (or *small angle scattering*), which can thus be measured to probe the sample morphology.

In the past the scattering techniques were limited to three dimensional samples as the strong penetration depth of the radiation and the low signal to noise ratio hampered the surface sensitivity. Thanks to the use of synchrotron radiation, scattering techniques have been extended to surface geometry using the phenomenon of total external reflection of X-rays in the grazing incidence angle. According to Snell's law, an electromagnetic wave impinging on a surface will be reflected and refracted according to the following relation:

$$n \cos\alpha = n' \cos\alpha' \tag{3.14}$$

with α, α' being the incident and diffraction angles and n, n' the refractive index of vacuum and surface material, respectively (See Fig. 3.8). The real part of the X-ray refractive index of a material is given by [51]:

$$n' = 1 - \frac{1}{2\pi} N Z r_0 \lambda^2 \tag{3.15}$$

where N is the numerical density of the material, Z is the atomic number and r_0 is the classical electron radius. The imaginary part of the refractive index, which takes into account the absorption of the medium, can be usually neglected for energies far from absorption edges, being two orders of magnitude smaller than the real part. For X-rays n is always slightly less then one (the vacuum value). Thus in case of X-rays propagating from the vacuum and impinging on a surface the reflection angle is in general larger than the refraction angle. From the Snell's law and the above relation for n we find the condition for total external reflection:

$$\cos\alpha' = 1 \Rightarrow \cos\alpha = \frac{n'}{n} = 1 - \frac{1}{2\pi} N Z r_0 \lambda^2 \tag{3.16}$$

Given a certain incidence angle α, the wavelength has to be higher then a critical value λ_C, or, for a given λ, the incidence angle has to be smaller then a critical angle α_C. In these conditions the refracted wave propagates parallel to the interface and is exponentially damped in the direction into the surface. This is the so-called *glancing angle geometry*, where the diffracted and scattered intensities arise mainly from the limited depth of the surface.

What kind of scattering patterns result from a 2D system? In 3D arrays of point-like objects, the light scattering results in very sharp peaks whose positions and intensity allow to determine the crystal structure of the solid. In case of a surface or an ad-layer the scattering pattern changes as described in the following, starting by writing the diffraction intensity for point-like objects, following the approach in [52]. The interaction of X-rays with matter is largely dominated by the Thompson scattering, resulting from the coupling between the electric field of the X-rays and the charge of the electrons inside an atom. When an incoming wave $\mathbf{E}_0 e^{-i\mathbf{k}_i \cdot \mathbf{r}}$ is scattered by a free electron the resulting scattered field $\mathbf{E}_e e^{-i\mathbf{k}_f \cdot \mathbf{r}}$ observed at a distance R from the electron has the amplitude E_0 given by [53], [54]:

$$E_e = E_0 \frac{e^2}{m_e c^2 R} P^{\frac{1}{2}} \tag{3.17}$$

where m_e is the electron mass and P is the polarization factor that assumes the values of $P = 1$ if $\mathbf{E}_0$ is normal to the scattering plane (the plane spanned by $\mathbf{k}_i$ and $\mathbf{k}_f$) and $P = \cos^2 2\alpha$ when $\mathbf{E}_0$ is in the scattering plane.
To find the scattering from one atom, one has to sum up the contributions from each of the Z electrons, distributed around the nucleus to give an atomic density $\rho_a(\mathbf{r})$. Then Eq. 3.17 becomes:

$$E_a = \int E_e \rho_a(\mathbf{r}) dV = E_0 \frac{e^2}{m_e c^2 R} P^{\frac{1}{2}} \int \rho_a(\mathbf{r}) e^{i\mathbf{q}\cdot\mathbf{r}} dV. \tag{3.18}$$

The integral at the right side of Eq. 3.18 is called atomic form factor and it is defined as

$$f_0(\mathbf{q}) = \int \rho_a(\mathbf{r}) e^{i\mathbf{q}\cdot\mathbf{r}} dV. \tag{3.19}$$

The next step is to calculate the structure factor, i.e. the scattering from atoms arranged in a three-dimensional crystal lattice described by the lattice vectors $\mathbf{a}_1$, $\mathbf{a}_2$ and $\mathbf{a}_3$. The position of each atom is written as

$$\mathbf{R}_{jj_1j_2j_3} = j_1\mathbf{a}_1 + j_2\mathbf{a}_2 + j_3\mathbf{a}_3 + \mathbf{r}_j \tag{3.20}$$

where $\mathbf{r}_j$ describes the atomic arrangement within the unit cell. The structure factor $F(\mathbf{q})$ is given as the sum of contributions to the scattering from the individual atoms in the unit cell. Including also the isotropic thermal vibration of atoms around the average position, the so-called Debye -Waller effect, the structure factor is:

$$F(\mathbf{q}) = \sum_j f_j(q) e^{i\mathbf{q}\cdot\mathbf{r}_j} e^{-B_j(\frac{q}{4\pi})^2}, \tag{3.21}$$

Here B_j is the so-called B-factor for the atom j, that defines the atom displacement from the average position. Finally, the intensity of the scattered wave $I(\mathbf{q})$ is calculated as the square of the corresponding amplitude of the scattered field $I(\mathbf{q}) = |E_{3\text{D}}|^2$ from a 3D lattice that gives:

$$I(\mathbf{q}) = I_0 \frac{e^4}{m_e^2 c^4 R^2} P |F(\mathbf{q})|^2 \frac{\sin^2\left(\frac{1}{2}N_1\mathbf{q}\cdot\mathbf{a}_1\right)}{\sin^2\left(\frac{1}{2}\mathbf{q}\cdot\mathbf{a}_1\right)} \frac{\sin^2\left(\frac{1}{2}N_2\mathbf{q}\cdot\mathbf{a}_2\right)}{\sin^2\left(\frac{1}{2}\mathbf{q}\cdot\mathbf{a}_2\right)} \frac{\sin^2\left(\frac{1}{2}N_3\mathbf{q}\cdot\mathbf{a}_3\right)}{\sin^2\left(\frac{1}{2}\mathbf{q}\cdot\mathbf{a}_3\right)}. \tag{3.22}$$

$I(\mathbf{q})$ has maxima when the Laue conditions are fulfilled:
$\mathbf{q}\cdot\mathbf{a}_1 = 2\pi H$, $\mathbf{q}\cdot\mathbf{a}_2 = 2\pi K$, $\mathbf{q}\cdot\ \mathbf{a}_3 = 2\pi L$
with H, K and L integers. The Laue conditions demand that $\mathbf{q}$ is a point in the reciprocal lattice, that is $\mathbf{q} = H\mathbf{b}_1 + K\mathbf{b}_2 + L\mathbf{b}_3$ with $\mathbf{b}_1$, $\mathbf{b}_2$ and $\mathbf{b}_3$ being basis vectors in the reciprocal space. The Laue condition for the momentum transfer perpendicular to the surface plane coincides with the Bragg law (Eq. 3.13).

In the case of diffraction from a surface, the abrupt interruption of the infinite 3D lattice at the surface breaks the bulk symmetry. The diffracted intensity in this case is the convolution between the diffracted intensity of the infinite lattice, leading to Bragg peaks as seen before, and the signal from a 2D system (surface) in between the Bragg peaks (crystal truncation rods) as we will see now. The derivation of the scattered intensity in the 2D case is very similar to the 3D case, but now the atomic lattice is described by only two basis vectors and therefore

$$R_{j,j_1j_2} = j_1\mathbf{a}_1 + j_2\mathbf{a}_2 + \mathbf{r}_j \tag{3.23}$$

with $\mathbf{a}_1$ and $\mathbf{a}_2$ in the plane of the surface. Here the vector $\mathbf{r}_j$ describes not only the atomic positions within the unit cell in the surface plane, but also the positions in the direction normal to the surface. In this case the Laue conditions are:

$$\mathbf{q}\cdot\mathbf{a}_1 = 2\pi H, \mathbf{q}\cdot\mathbf{a}_2 = 2\pi K, \tag{3.24}$$

and the component q_z of $\mathbf{q}$ in the direction normal to the surface becomes a continuous variable. The reciprocal lattice therefore consists of rods instead

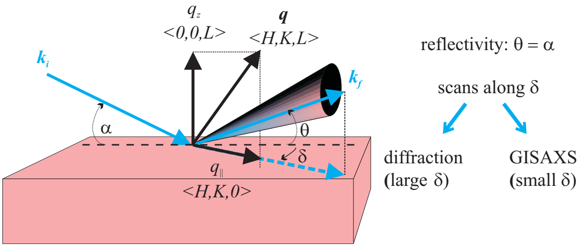

Figure 3.9: Scheme illustrating the different kinds of measurement geometry used in this thesis.

of sharp delta functions. These continuous intensity distributions are called crystal truncation rods (CTR), or Bragg rods since they are curves that connect the Bragg reflections. The minima of the CTR along the so-called L-axis, located in the midpoint between two consecutive Bragg reflections, correspond to scattering conditions of destructive interference between two consecutive crystal planes. Because of that the bulk contribution to the scattered intensity is very small, and all what remains is the diffraction from the topmost layers, or surface scattering. At the minima of the CTR therefore the surface sensitivity is the highest. The diffraction from the surface occurs at any position along these rods. The definition of the structure factor in Eq. 3.21 is the same, and the peak intensity is

$$I_{HK}^{peak}(\mathbf{q}) = I_0 \frac{e^4}{m_e^2 c^4 R^2} P |F_{HK}(q_z)|^2 N_1^2 N_2^2. \tag{3.25}$$

The structure factor is calculated with the indices (H, K) for the in-plane component of the momentum transfer, but depends also on the continuous out-of-plane component q_z. This dependence describes the arrangement of the atoms in the direction normal to the surface. The intensity of the surface signal is several orders of magnitude lower then the bulk signal, therefore intense synchrotron light is required for these experiments. Several measurements techniques are used to extract information on the sample structure. Grazing incidence geometry is used in order to enhance the sensitivity to the surface contribution to the scattering. In the following those that have been used in the thesis are recalled (see Fig. 3.9).

Grazing Incidence X-ray Diffraction (GIXRD)

- *Reflectivity.* Reflectivity measurements are performed by keeping the detector at an exit angle equal to the incident angle ($\theta = \alpha$ in Fig 3.9). One therefore measures the light reflected from the sample, that in reciprocal space corresponds to measuring the intensity along q_z. Following the argument about refraction, one can say that the reflectivity R equals one below a critical angle α_C and then falls like $R_\mathrm{F} \propto \alpha^{-4}$ for larger α (Fresnel law for a perfectly flat surface) as shown in Fig. 3.10. In the case of more complex systems one can use the matrix formalism normally employed in classical optics [55] for stratified media.

  Any kind of disorder which is present on the surface or interface can be described by the z coordinate of a point $\mathbf{x}$ on the surface (or interface), $z(\mathbf{x})$. The latter is usually assumed to be a Gaussian random variable, and therefore described by the standard deviation σ. The main effect of roughness is to decrease the reflected intensity (see Fig. 3.10). Mathematically, the Fresnel reflectivity becomes multiplied by an exponential term that depends on σ [56]:

  $$R(q) = R_\mathrm{F}(q)e^{-q^2\sigma^2} \tag{3.26}$$

  A measurement of the reflectivity therefore gives information on the roughness of a surface. The scattered intensity from a surface is composed of two parts: specular reflection and diffuse scattering. The intensity lost due to diffuse scattering is redistributed in the reciprocal space.

  In case of a smooth film of a different chemical species adsorbed on the surface, the interference between reflection from the top of the surface and the interface between substrate and monolayer leads to an oscillation of the intensity, known as *Kiessig fringes* [57, 58]. The angular spacing $\Delta\alpha$ between two Kiessig maxima is, in first approximation, inversely proportional to the total ad-layer thickness t, $\Delta\alpha \propto \frac{\lambda}{t}$ [59]. The number of oscillations instead is connected with the film roughness and homogeneity.

- *CTR.* In this case the exit angle is different from the incidence angle and this gives information about the atomic structure along different directions then the perpendicular one. A measurement of the intensity of the CTRs as a function of the continuous variable L is in this way performed. The (H,K) vector can be chosen corresponding to special axis of the in-plane unit cell. L scans contain information about both normal and in-plane atomic ordering and roughness of the interfaces.

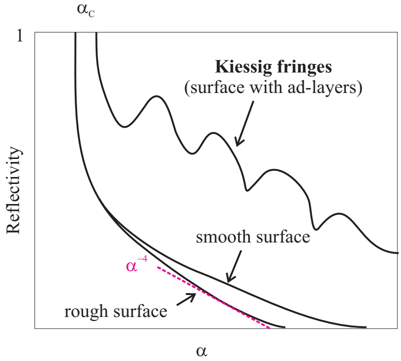

Figure 3.10: Schematic of a reflectivity scan measured for different systems.

- *In-plane δ-scans.* The diffracted intensity is recorded at grazing incidence for different values of the angle $\delta > 10°$. For a disordered film it coincides with the 2Θ scan of a powder sample containing crystal grains in all the possible orientations. It gives information about the in-plane atomic structure of the film. In case of a sample made of many particles on a surface with random orientation it will give information about the crystal structure of the constituents.

Grazing Incidence Small Angle X-ray Scattering (GISAXS)

The GISAXS technique is commonly used for probing structures on large length scales such as self-assembled nano-particles with sizes up to a few microns. The measurements are performed at very small scattering angles (between few micro-radians to a tenth of a radian) and at grazing incidence to be surface sensitive. A specific value for q is chosen by fixing the scattering angle, and then a scan of the angle δ is performed to monitor the diffuse scattering profile along this direction. The use of a CCD camera allows to record GISAXS scans for a broad range of q values. These measurements are technically challenging because of the small angular separation of the direct beam (which is very intense) and the scattered beam. Often a beam stop has to be used to block the direct beam, the reflected beam or the diffuse scattering.

Electron density variations or surface roughness produce beam scattering in the non-specular direction (diffuse scattering). This is in particular the case for islands or dots on a surface. The description of the system is done in

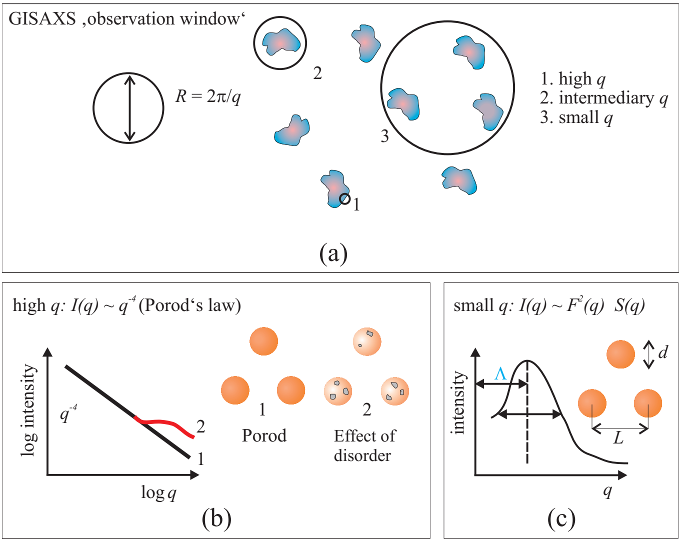
GISAXS ‚observation window‘
R = 2π/q
2
3
1
1. high q
2. intermediary q
3. small q
(a)
high q: I(q) ~ q^-4 (Porod‘s law)
log intensity
q^-4
2
1
log q
1
Porod
2
Effect of disorder
(b)
small q: I(q) ~ F^2(q) S(q)
d
Λ
intensity
L
q
(c)

Figure 3.11: (a) Cartoon showing the different q regimes in GISAXS measurements; (b)-(c) GISAXS intensity for a system made out of spherical particles with diameter d and inter-particle distance L in the limit of high (b) and small q (c). In the high q regime the effect of disorder at the particle interface on the GISAXS intensity is also shown.

the framework of the distorted-wave Born approximation [60], that takes into account multiple scattering events due to the surface roughness. An approximated formula for the GISAXS intensity $I(q)$ from an ensemble of randomly oriented clusters on a flat surface is [61]:

$$I(q) \approx S(q)|F(q)|^2 \tag{3.27}$$

where $F(q)$ is the form factor of the clusters averaged over the size distribution and crystal orientations of the particles and $S(q)$ is the correlation function describing the average spatial distribution of the clusters, that characterizes the particle ordering. Therefore from the GISAXS intensity it is possible to determine average information for both quantities [62, 63].

For a binary sample composed for example by particles with density ρ_1 embedded in a matrix element with density ρ_2, the scattered intensity is also proportional to the electronic contrast, defined by the difference $\Delta\rho = \rho_1 - \rho_2$.

The more different the two materials are electronically, the more intense is the scattered signal. A certain q value will correspond to a window in real space with a diameter given by $R = \frac{2\pi}{q}$: a scattering signal is observed only if the electronic contrast $\Delta\rho$ inside the window is different from zero. The value of q determines therefore the minimum and maximum size of a particle that can be observed using this technique. The q-range in small angle scattering experiments is usually divided into three domains (Fig. 3.11 (a)). In each of this domains approximations of the Eq. 3.27 are found, that allow to have information about different properties of the system:

- *High q domain: interface*
  In the limit of large q the observation window size is of the same order or smaller then the size of the scattering element and the contrast is obtained only at the interface between two phases with different density. Therefore GISAXS measurements in this range give information about the interface. The small angle scattering intensity follows a power law whose exponent depends on how the two phases are separated. Namely, the scattered intensity doesn't contain information about order but only depends on the form factor $F(q)$ of the nano-objects that contribute to scattering (scattering elements, or domains), that means the regions of the sample of differing electron density. A simple expression for the scattered intensity can be found, that describes the dependence of scattered light on the window size R. This is simply proportional to the number of scattering elements in the irradiated volume, $N(R)$, and to the number of electrons in the area defined by R, $n_e^2(R)$:

  $$I(q) = N(R) \cdot n_e^2(R) \tag{3.28}$$

  From this equation one finds that $I(q)$ is proportional to the volume corresponding to D, since the number of electrons in a particle goes like the volume of the particle, and the number of particles goes like the inverse of the particle volume. Since the particle volume decreases with q, the GISAXS intensity always displays a decaying behavior with q.

  Depending on the specific geometry of the interfaces, the proportionality expressed by Eq. 3.28 leads to different power laws, a few of them we recall in the following. In the case of a 3D sample composed of spherical objects with well defined separation surfaces the scattered intensity follows an asymptotic law in the high q region (Porod's limit, see Fig. 3.11 (b)):

$$I(q) \simeq q^{-4}. \tag{3.29}$$

If $q^4 I(q)$ does not converge towards a constant value at large q, then the volumes of different electron density might be fractal. In this case the (modified) Porod's trend would give

$$I(q) \sim q^{-(6-D_\mathrm{f})} \tag{3.30}$$

where D_f is the fractal dimension of the system. Other commonly observed power laws in GISAXS are: diffuse interface law: $I(q) \sim q^{-(4+\eta)}$, in case of intermixing of the two phases at their interface (η describes the concentration decay of the diffuse interface) and the dimensional scattering law:

$$I(q) \sim q^{-D} \tag{3.31}$$

for nano-objects with D being the spatial dimension (for a rod $D = 1$, for a disk $D = 2$ and for a sphere $D = 3$). This expression is derived from the dependence of the mass, and therefore of the scattered intensity, on the size of the object raised to the dimension.

- *Intermediate zone: size and shape of a particle*
  In this regime the window has the size of one of the constituent elements of the systems (e.g. a nano-particle). In the dilute regime where interactions among particles can be neglected the scattered intensity is directly proportional to the form factor $F(q)$ of a single particle. Size, shape and internal structure of a particle can therefore be measured.

- *Small q domain (or 'dense' system limit): interactions between particles*
  The observation window is in this case very large and contains many particles. The scattered intensity therefore also depends on the $S(q)$ term, and in addition to the particle geometry it also contains information about the spatial ordering (average distance between particles) and interactions of the particles. For a system of particles with the same size and the same distance from each other the term $S(q)|F(q)|^2$ has a typical bell shape, from which it is possible to derive the mean particle diameter d and the mean distance between particles L (see Fig. 3.11 (c)). After converting the angle δ into momentum transfer in the surface plane $q_\parallel$ according to the formula

$$q_\parallel = \frac{4\pi}{\lambda} \cdot \sin(\frac{\delta}{2}), \tag{3.32}$$

d and L are estimated from the Full Width at Half Maximum ($FWHM = \Delta$) and the position of the maximum of the intensity curve (Λ):

$$d = \frac{2\pi}{\Delta}; L = \frac{2\pi}{\Lambda} \tag{3.33}$$

.

The GISAXS intensity versus q is usually displayed in double-logarithmic plots to determine the power law dependence at different values of q. In this way the components with different size of a system can be more easily identified, since they lead to distinctively different power laws. It is important to stress that the definition of a particle in GISAXS does not reflect necessarily a real domain, but the size of an element that contributes to the scattering of light.
X-ray scattering and diffraction experiments shown in this thesis were performed at the ID03 beamline of the ESRF.

3.2.2 XAS and XMCD

X-ray absorption spectroscopy (XAS) is an element specific technique that allows to probe unoccupied electronic states of a given material. The process of absorption is studied at different photon energies and therefore a tunable light source is required which is provided by the synchrotron facilities. The synchrotron radiation offers high intensity and brilliance in a wide range of energies.

XAS experiments with polarized light allow to probe the magnetic state of the system. Qualitatively this is explained by a dependence of the absorption process on the relative orientation between sample magnetization $\mathbf{M}$ and photon helicity $\boldsymbol{\epsilon}$. The light can have linear or right (R) and left (L) circular polarization. The corresponding helicity is conventionally labeled as $\boldsymbol{\epsilon}^0$ for linear and $\boldsymbol{\epsilon}^{\pm}$ for R and L circular polarization. In Fig. 3.12 (a) the XAS recorded for Co/Ag(111) is plotted, in the energy range of the Co $L_{3,2}$ absorption edges (blue and red curves). As a reference the background signal of a clean Ag(111) substrate is shown. The spectra have been recorded for R and L circular polarized light, and it is evident that the absorption process is different in the two cases. The X-ray magnetic circular dichroism (XMCD) is simply defined as the difference in the absorption cross sections for parallel σ^+ and antiparallel σ^- alignment between $\mathbf{M}$ and $\boldsymbol{\epsilon}$ for circular polarized light (Fig.3.12 (b)). This can be measured equivalently by using R and L circular polarization or by changing the magnetization direction. The maximum dichroism effect is obtained when the magnetization is aligned with

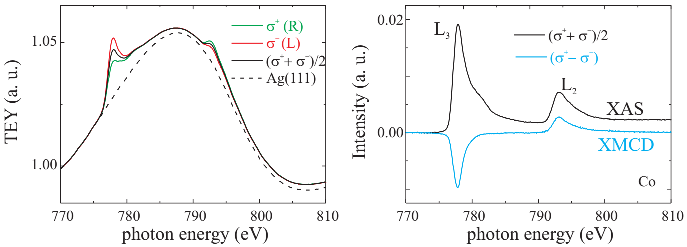

(a) (b)

Figure 3.12: Spectroscopy and dichroism of the valence d-band of Co on Ag(111): (a) Total electron yield (TEY) for right (R) and left (L) circularly polarized light at the Co $L_{3,2}$ absorption edge, corresponding to parallel (σ^+) and anti-parallel (σ^-) orientation between sample magnetization $\mathbf{M}$ and photon helicity $\boldsymbol{\epsilon}$; the dotted line indicates the Ag(111) reference background; (b) XAS spectra for Co after Ag(111) background subtraction and dichroic signal (XMCD).

the photon spin direction. If there is an angle θ between the two, then the XMCD signal is scaled by $\cos\theta$.
It will be shown in the following, that the XMCD intensity is proportional to the imbalance between the minority and majority $3d$ states above the Fermi level, which in turn is proportional to $\mathbf{M}$. Changes in the XMCD therefore record variations of $\mathbf{M}$.

The starting point to explain the sensitivity to magnetism of XMCD is the interaction between photons and matter. The light excites electrons in the core levels generating transitions to empty levels with higher energies (absorption process, see Fig. 3.13 (b)). The absorption cross section σ is defined as the number of excited electrons per unit time (or the transition amplitude $w_{i\to f}$ between initial and final state), divided by the incident photon flux I_0:

$$\sigma = \frac{w_{i\to f}}{I_0}. \tag{3.34}$$

The transition amplitude per unit time is given to first order perturbation theory by Fermi's golden rule:

$$w_{i\to f} = \frac{2\pi}{\hbar}\sum_f |<f|\widehat{H_1}|i>|^2 \delta(E_f - E_i - \hbar\omega) \tag{3.35}$$

where E_f, E_i are the energy of final and initial states, respectively. The Hamiltonian $\widehat{H_1}$ describes the absorption process and is given by $\widehat{H_1} =$

$-\frac{e}{mc}\mathbf{A}\cdot\mathbf{p}$, with $\mathbf{A}$ being the vector potential of the electromagnetic radiation and $\mathbf{p}$ the momentum operator of the electron. H_1 is the first term of the full Hamiltonian that describes the interaction between matter and light, and also comprises scattering terms [64]. Without going into details, to calculate the absorption cross section in Eq. 3.34 one makes the approximation that during the absorption process the core-electron, localized around the nuclei, does not 'see' the spatial variation of the electromagnetic wave and therefore $e^{i\mathbf{k}\cdot\mathbf{r}} \approx 1$ (electric dipole approximation). This approximation is valid in the energy range of soft X-rays. $\mathbf{k}$ is the light wave vector and $\mathbf{r}$ is the space coordinate of the electron wavefunction. A further assumption concerns the electron excitation process which is considered to be a one-electron process. This allows to write the initial state as a core wavefunction and the final state as a free electron wavefunction [65]. All the other electrons are assumed not to take part in the X-ray transition process.
With these approximations Eq. 3.34 becomes [66]:

$$\sigma = \frac{4\pi^2 e^2}{\hbar c}\hbar\omega \sum_f |<f|\boldsymbol{\epsilon}\cdot\mathbf{r}|i>|^2 \rho(E_\mathrm{f} = E_\mathrm{i} + \hbar\omega) \qquad (3.36)$$

where $\rho(E)$ is the density of unoccupied final states. In the above equation, for circularly polarized light the propagation direction is chosen to point along the z axis, that corresponds to the quantization axis of the system, given by the magnetization direction. Permitted transitions are only those for which the matrix element in Eq. 3.36 is not zero. One finds conditions for the quantum numbers of the final state, also known as electric-dipole selection rules. These conditions are:
$\Delta j = 0, \pm 1, \Delta l = \pm 1, \Delta s = 0, \Delta m_l^{linear} = 0, \Delta m_l^{R,L} = \pm 1.$
j, l, and s are the quantum numbers of the total angular momentum, the orbital angular momentum and the spin momentum. m_l and m_s are the components of the orbital and spin moments along the quantization direction. The superscript label of m_l indicates the light polarization.

The dipole operator $\boldsymbol{\epsilon}_\pm \cdot \mathbf{r}$ does not involve the electron spin, and thus the photo-electron spin is conserved during the absorption process. Furthermore, if the photoelectron originates from a spin-orbit split level, e.g. the $p_{3/2}$ level, the angular momentum of the photon can be transferred in part to the spin through the spin-orbit coupling. As will be shown more precisely below, since the $p_{3/2}$ and $p_{1/2}$ levels have opposite spin-orbit coupling ($l + s$ and $l - s$, respectively), the spin-polarization will be opposite at the two edges, L_3 and L_2.

For transition metal elements the dipole-permitted excitations from core p to valence d states have energies in the soft X-ray range. For $3d$ transition

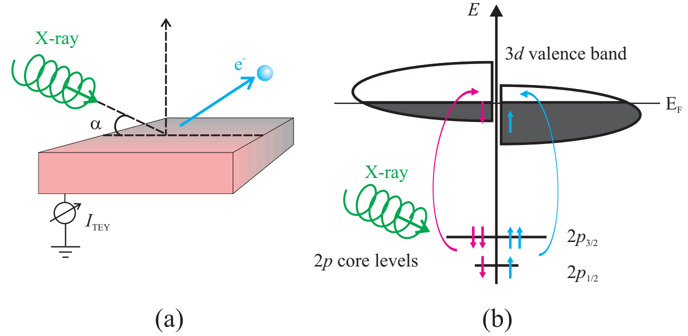

Figure 3.13: (a) Schematic drawing of the XAS measurement in the TEY mode; (b) Absorption process in the case of $2p \rightarrow 3d$ transitions.

metals the dipole selection rules allow the following transitions:

$$K : 1s \rightarrow 4p_{1/2}$$

$$L_2 : 2p_{1/2} \rightarrow 3d_{3/2}, 4s$$

$$L_3 : 2p_{3/2} \rightarrow 3d_{3/2,5/2}, 4s,$$

The p to d channel often called 'white lines' largely dominates the absorption process by 95% [67].
The sum of the L_3 and L_2 line intensities after the correction for transitions into continuum states is proportional to the number of holes in the $3d$ band. This correction is usually done by the subtraction of step functions from the experimental XAS [68]. In absence of spin-orbit coupling at the final states, a ratio (so called branching-ratio) $2:1$ is expected for the white line intensities at the L_3 and L_2 edges for unpolarized radiation, which reflects the number of sub-levels of the $p_{3/2}$ and $p_{1/2}$ states.

To understand the role of light polarization in revealing the valence state magnetization one has to consider the transition matrix elements for p to d transitions that describe the absorption process (Eq. 3.36). The procedure follows again Ref. [69].
First, the initial and final states of the system $|i>$ and $|f>$ are written as a linear combination of $|nlm_l m_s>$ states using Clebsch-Gordan coefficients. This is because the absorption process involves the angular momentum quantum numbers l and m_l and not the total moment j. In Table 3.1 the decomposition of the $2p$ states with $j = 3/2$ and $j = 1/2$ is shown.

Second, the matrix elements in Eq. 3.36 are calculated for R and L circularly polarized light, corresponding to the helicity $\boldsymbol{\epsilon}_{\pm}$. For $2p \rightarrow 3d$ transitions from the above selection rules one finds that the only non-zero matrix elements are those for which $l^{'} = l + 1$ and $m_l^{'} = m_l \pm 1$:

$$< f|\boldsymbol{\epsilon}_{\pm} \cdot \mathbf{r}|i > = < n^{'}, l^{'} = l + 1, m_l^{'} = m_l \pm 1|\boldsymbol{\epsilon}_{\pm 1} \cdot \mathbf{r}|nlm_l >$$

$$= -\sqrt{\frac{(l \pm m_l + 2)(l \pm m_l + 1)}{2(2l+3)(2l+1)}} \cdot Q = M_{jm}^{\pm} \cdot Q, \tag{3.37}$$

where Q is the radial part of the integral, independent on the light polarization. In the third and forth column of Table 3.1 the squared matrix elements calculated according to Eq. 3.37 are listed for R and L polarized light. Adding all contributions for one specific spin direction (up for example), one finds the probability P to excite the respective spin state with a certain light polarization (R or L) (after normalizing for the sum of all possible squared matrix elements for a given edge), for both edges: $P_{\mathrm{R,up}}(L_3) = 62.5\%$, $P_{\mathrm{L,up}}(L_3) = 37.5\%$, $P_{\mathrm{R,up}}(L_2) = 25\%$, $P_{\mathrm{L,up}}(L_2) = 75\%$. This means that R-circularly polarized light excites more spin up at the L_3 edge than at the L_2 edge, and the opposite is true for L circular polarized light.

Table 3.1: Decomposition of the base $|njm_j >$ (first column) into $|nlm_lm_s >$ (second column) and squared matrix elements $(M_{jm}^{\pm}/Q)^2 = (< f|\epsilon_{\pm} \cdot \mathbf{r}|i > /Q)^2$ (third and forth column), according to Eq. 3.37.

j, m_j	m_l, m_s	$(M_{jm}^{+}/Q)^2$	$(M_{jm}^{-}/Q)^2$
$\frac{3}{2}, +\frac{3}{2}$	$\lvert +1 \uparrow>$	$(\frac{2}{5})_{\uparrow}$	$(\frac{1}{15})_{\uparrow}$
$\frac{3}{2}, +\frac{1}{2}$	$\sqrt{\frac{1}{3}}\lvert +1 \downarrow> + \sqrt{\frac{2}{3}}\lvert 0 \uparrow>$	$(\frac{2}{15})_{\downarrow} + (\frac{2}{15})_{\uparrow}$	$(\frac{1}{45})_{\downarrow} + (\frac{2}{15})_{\uparrow}$
$\frac{3}{2}, -\frac{1}{2}$	$\sqrt{\frac{2}{3}}\lvert 0 \downarrow> + \sqrt{\frac{1}{3}}\lvert -1 \uparrow>$	$(\frac{2}{15})_{\downarrow} + (\frac{1}{45})_{\uparrow}$	$(\frac{2}{15})_{\downarrow} + (\frac{2}{15})_{\uparrow}$
$\frac{3}{2}, -\frac{3}{2}$	$\lvert -1 \downarrow>$	$(\frac{1}{15})_{\downarrow}$	$(\frac{2}{5})_{\downarrow}$
$\frac{1}{2}, +\frac{1}{2}$	$-\sqrt{\frac{2}{3}}\lvert +1 \downarrow> + \sqrt{\frac{1}{3}}\lvert 0 \uparrow>$	$(\frac{4}{15})_{\downarrow} + (\frac{1}{15})_{\uparrow}$	$(\frac{2}{45})_{\downarrow} + (\frac{1}{15})_{\uparrow}$
$\frac{1}{2}, -\frac{1}{2}$	$-\sqrt{\frac{1}{3}}\lvert 0 \downarrow> + \sqrt{\frac{2}{3}}\lvert -1 \uparrow>$	$(\frac{1}{15})_{\downarrow} + (\frac{2}{45})_{\uparrow}$	$(\frac{1}{15})_{\downarrow} + (\frac{4}{15})_{\uparrow}$

If one interprets the absorption as a two-step process then, in the single electron approximation, after the initial excitation step the absorption cross section is also proportional to the density of final states (Eq. 3.36). In the

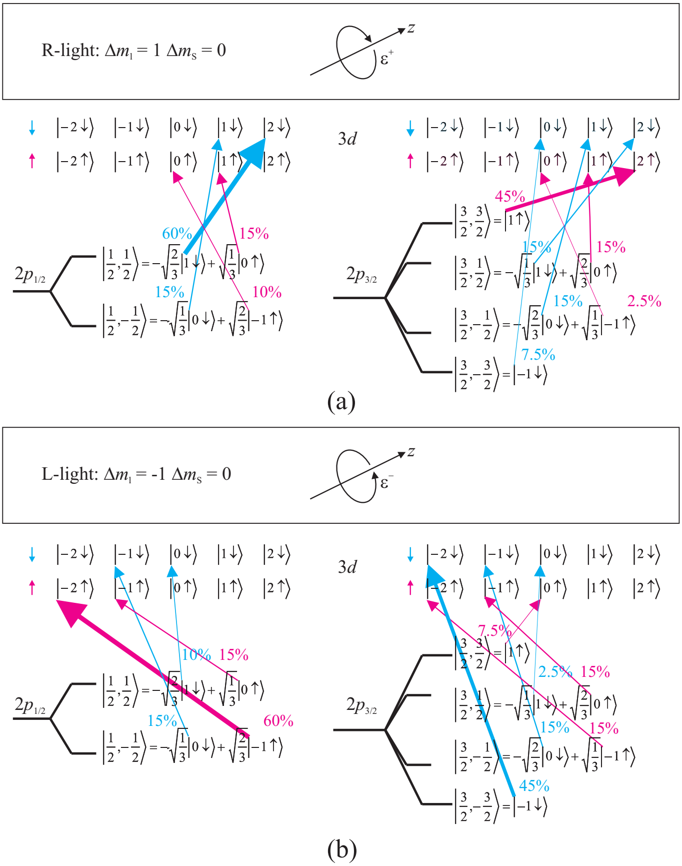
R-light: Δm_l = 1 Δm_s = 0
z
ε⁺
3d
|−2↓⟩ |−1↓⟩ |0↓⟩ |1↓⟩ |2↓⟩
|−2↑⟩ |−1↑⟩ |0↑⟩ |1↑⟩ |2↑⟩
2p1/2
|1/2, 1/2⟩ = −√(2/3)|1↓⟩ + √(1/3)|0↑⟩
|1/2, −1/2⟩ = −√(1/3)|0↓⟩ + √(2/3)|−1↑⟩
60%
15%
15%
10%
2p3/2
|3/2, 3/2⟩ = |1↑⟩
|3/2, 1/2⟩ = −√(1/3)|1↓⟩ + √(2/3)|0↑⟩
|3/2, −1/2⟩ = −√(2/3)|0↓⟩ + √(1/3)|−1↑⟩
|3/2, −3/2⟩ = |−1↓⟩
45%
15%
15%
15%
2.5%
7.5%
(a)
L-light: Δm_l = -1 Δm_s = 0
z
ε⁻
10%
15%
15%
60%
7.5%
2.5%
15%
15%
15%
45%
(b)

Figure 3.14: Allowed transitions between $2p$ and $3d$ states for the case of spin-orbit interaction in the $2p$ shell and spin polarization in the $3d$ shell. The strength (probability) of the transition for each $|m_l m_s>$ state is also indicated, calculated from the matrix elements $(M^{\pm}_{jm}/Q)^2$ listed in Table 3.1 third and forth column, normalized by the sum of all the matrix elements at the same edge. The scheme is drawn for both R (a) and L (b) circular polarized light.

absence of a net magnetization (spin-polarization) in the final state, that is if spin-up and spin-down states are equally populated, there is no difference between the spectra taken with R- and L-circularly polarized photons and no dichroism is observed. The total (spin up and spin down) transition intensities for R and L circular polarization are in fact identical. The total spin polarization for the p level, summing up over the $p_{3/2}$ and $p_{1/2}$ manyfolds, is also equal to zero.

The situation is different if the $3d$ band is split into a spin majority and a spin minority band, i.e., the empty states have predominantly minority character. In this case the final states act as a filter for the spin of the excited photoelectron. If for example there are only spin down empty states, then the dichroic signal will only be sensitive to spin down electrons. The XAS signal at the L_3 edge will be larger for L (62.5% spin down) than for R circularly polarized light (37.5% spin down) and *vice-versa* at the L_2 edge, giving a non-zero dichroic signal. If both spin up and down states are available at the final state, then the dichroism is proportional to the difference between them.

Similarly, if the d valence shell possess an orbital momentum, it will act as an orbital momentum filter for the excited photoelectrons that will also contribute to the dichroic signal. The presence of a non-vanishing orbital magnetic moment in the final state will lead to L_3/L_2 ratios of the XMCD signal which differ from the $-1 : 1$ value that one would expect, using the matrix elements given in Tab. 3.1. The XMCD at the L_3 edge in fact is found to have a higher intensity then at the L_2, and this effect is attributed to the spin-orbit coupling in the final state that lifts the degeneracy of the d states (un-quenching of the orbital moment, see Chapter 2). Therefore the L_3 and L_2 edges probe different final states, according to the dipole selection rules [67].

A scheme of allowed transitions and relative intensities between the initial states given by the $2p_{3/2}$ and $2p_{1/2}$ core states and the final $3d$ states, split into minority and majority can be seen in Fig. 3.14. The probabilities P for each transition (squared matrix element normalized by the sum of all the squared matrix elements for the considered edge) are also indicated, after calculation using the matrix elements in Tab. 3.1. It is clear that P depends on light polarization and value of m_l in the initial state.

Given an experimental set of data one can use the so-called sum rules to extract the orbital and spin contribution to the magnetic moment from an XMCD spectrum, as discussed in the following section.

Sum rules and measurement methods

Three important magneto-optical sum rules [70, 71] relate the XAS and XMCD data to the element specific orbital and spin magnetic moment, and to the anisotropy terms of the spin and charge densities in the unit cell. The derivation of these rules has been carried out for electric dipole transitions in a localized model, considering a single ion in an arbitrary crystal field symmetry. Hybridization of the final states is only allowed for intra-shell orbitals, i.e. there is no mixing of the d states with sp-like states. The sum rules have been verified experimentally [68] for the $3d$ metals Fe and Co.

The first rule relates the shell-specific groundstate expectation value of the orbital angular momentum operator $\widehat{L}_z$ (z is the direction specified by the incident photon beam) to the integral of the XMCD adsorption spectrum taken over the complete core level edge of a magnetically oriented ferromagnetic or ferrimagnetic material. The ground state expectation value of the orbital angular momentum per hole can be expressed as:

$$\frac{1}{2}\frac{l'(l'+1)+2-l(l+1)}{l'(l'+1)(4l'+2-n_h)} < \widehat{L}_z >= \frac{\int_{j_+ + j_-} dE(\sigma^+ - \sigma^-)}{\int_{j_+ + j_-} dE(\sigma^+ + \sigma^- + \sigma^0)} \tag{3.38}$$

where n_h is the number of holes in the d shell, and the denominator term normalizes the XMCD signal to the unpolarized (isotropic) absorption spectrum (σ^0 is the absorption coefficient for linearly polarized light) and it is usually taken to be the average between σ^+ and σ^-. l and l' are orbital quantum numbers for initial (core electrons) and final (valence electrons) state, respectively and $j_\pm = l \pm \frac{1}{2}$.

The second sum rule relates the XMCD signal to the shell-specific groundstate expectation values of the total spin operator $\widehat{S}_z$ per hole and of the intra-atomic magnetic dipole operator $\widehat{T}_z$ per hole:

$$\begin{aligned} &\frac{l'(l'+1)-2-l(l+1)}{3l(4l'+2-n_h)} < \widehat{S}_z > + \\ &+\frac{l'(l'+1)[l'(l'+1)+2l(l+1)+4]-3(l-1)^2(l+2)^2}{6l'l(l'+1)(4l'+2-n_h)} < \widehat{T}_z >= \\ &= \frac{\int_{j_+} dE(\sigma^+ - \sigma^-) - \frac{l+1}{l}\int_{j_-} dE(\sigma^+ - \sigma^-)}{\int_{j_+ + j_-} dE(\sigma^+ + \sigma^- + \sigma^0)}. \end{aligned} \tag{3.39}$$

The term containing $< \widehat{T}_z >$ arises from the multipole expansion of the spin density: the largest (monopole) term integrated over the atomic volume corresponds to the isotropic magnetic spin moment; the next higher (quadrupole) term reflects the lowest order anisotropic spin distribution in the atomic shell and it gives rise to the intra-atomic magnetic dipole moment $\mu_T = -\mu_\mathrm{B} < \widehat{T}_z >$, where $\mu_\mathrm{B} = \frac{e\hbar}{2m_e}$ is the Bohr magneton. First principle calculations show that the $7 < \widehat{T}_z >$ term in the previous equation can be safely neglected for atoms in bulk cubic symmetry. However, its contribution can be of the order of 10 per cent of $< \widehat{S}_z >$ for atoms in highly asymmetric environments like surfaces and interfaces.

In the derivation of Eqs. 3.38 and 3.39, the sample magnetization is supposed to be completely saturated, which might not always be the case in an experiment. If the saturation is incomplete, the ratio $\frac{<\widehat{L}_z>}{<\widehat{S}_z>}$ is more reliable, since it is independent on the number of holes in the d band and therefore the experimental value can be directly compared with theory. The orbital and spin magnetic moments are related to the expectation values of the $\widehat{L}_z$ and $\widehat{S}_z$ operators by $\mu_L = -\mu_\mathrm{B} < \widehat{L}_z >$ and $\mu_S = -2\mu_\mathrm{B} < \widehat{S}_z >$, respectively, where z is the direction of the spin quantization axis. If $< \widehat{T}_z >$ can be neglected with respect to $< \widehat{S}_z >$, the ratio $\frac{\mu_L}{\mu_S}$ can be easily evaluated. Often the XMCS/XAS ratio calculated at the L_3 edge is reported as a measurement of the magnetization per atom in the sample. Since the absorption coefficient at the L_3 is proportional to the number of magnetic atoms in the sample, the ratio can be directly compared to other experiments.

The X-ray cross section of an atom is directly proportional to the number of core holes created in the absorption process [72]. Therefore any process that is a measure of core holes created upon interaction with X-rays can be used for quantitative X-ray absorption spectroscopy. The XAS spectra can be acquired by measuring the light intensity transmitted through the sample (direct transmission), or by recording the 'product' of the decay process occurring after photon absorption. The core holes are filled either by Auger electrons or by fluorescence (radiative) decay. Therefore one can measure either the photons (fluorescence, [73]) or the electrons (total electron yield, TEY) emitted during the de-excitation process. Fluorescence and TEY measurements are more suitable for *in-situ* surface preparations, since they allow using bulk crystals rather then very thin samples. Fluorescence measurements instead contain more information about bulk, since the photons have a greater escape depth than electrons whereas the TEY technique enables absorption experiments with sub-monolayer sensitivity, essential for the experiments on nano-structures that will be shown in the next chapter.

In TEY, the absorbed X-ray intensity is measured by monitoring the sample-drain current, due to the photo-electrons that are created during the photon absorption process (Fig. 3.13 (a)). The generated holes are mostly filled by Auger decay, which is the dominant decay process in the soft X-ray region

(as compared to fluorescence). As the primary Auger electrons leave the sample they create scattered secondary electrons which dominate the TEY intensity. The sampling depth in TEY measurements is typically 1 - 2 nm, corresponding to the mean free path of electrons inside the material.
As long as there are no electron yield saturation effects (occuring when the mean free path of the electrons inside the material is larger or comparable to the penetration depth of the X-ray [74]), the TEY current is found to be proportional to the product $\sigma(E) \cdot E$ of the absorption cross section times the energy [75]. Therefore the intensity of the emitted Auger electrons and related secondary cascade can be taken as a direct measurement of the absorbed X-ray intensity, which can be used to monitor different compounds.

XMCD experiments shown in this thesis have been performed at the ID8 beamline at the ESRF and at the UE46 beamline at BESSY. In both cases X-ray absorption spectra are measured in the surface sensitive total electron yield (TEY) mode. In order to get magnetic contrast absorption spectra were measured for positive (σ^+) and negative (σ^-) X-ray circular polarization with magnetic fields of up to $B = 5.5$T applied parallel and antiparallel to the photon beam. The angle of incidence of the X-ray beam could be varied between $\alpha = 90°$ (normal incidence) and $\alpha = 20°$ (grazing incidence) as shown in Fig. 3.13 (a). The XAS signal is obtained as the average intensity $(\sigma^+ + \sigma^-)/2$ while the XMCD is $(\sigma^+ - \sigma^-)$. The experimental timescales for measuring spectra as well as ramping of the magnets to their designated values (measurements at ESRF) are of the order of 10-100s.

3.3 Sample preparation and measurement procedure

This section describes the experimental procedure used for the preparation of samples discussed in the next Chapter 4. Buffer layer assisted growth includes the following preparation steps under ultrahigh vacuum: (1) the pre-adsorption of a noble gas buffer layer, typically Xenon, on crystalline substrate surfaces, (2) the deposition of the cluster material, (3) the increase of the substrate temperature to 300K, to desorb the buffer layer and to bring the metal in contact with the substrate.

3.3.1 Rh nano-structures

The experiment was entirely performed at the ESRF. Ag(100) substrates were cleaned by several sputtering/annealing cycles at 900eV and 600°C, respectively. The cleanliness and structural order of the crystal surface was

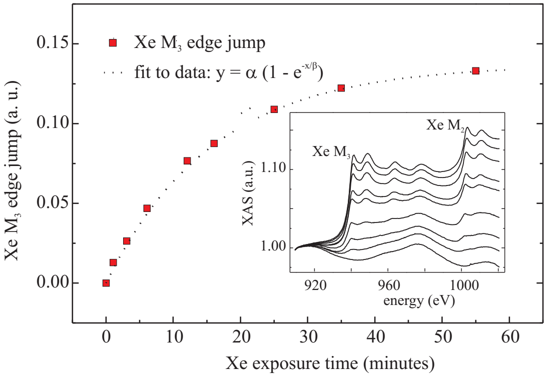

Figure 3.15: Xe M_3 edge jump as a function of exposure time (squares) and fit to the data (dotted line). The inset shows the full XAS at the Xe $M_{3,2}$ absorption edges for several exposure times. The adsorption temperature was 10K.

verified by Auger, LEED and STM measurements. Contamination checks prior and after the measurements were also done using the Oxygen K absorption edge situated at 543.1eV. Crystals were prepared and transferred to the magnet chamber in pressure conditions of $2 \cdot 10^{-10}$mbar.

The Xe gas is adsorbed on the sample at substrate temperatures of $T =$ 10K using an inlet system. The gas inlet was equipped with a nozzle and a gauge to monitor the pressure present during the adsorption of Xe on the clean substrate. Knowing the total volume of Xe in the gas inlet system, the pressure and the distance from the nozzle to the substrate allows a rough estimation of the amount of adsorbed Xe. Independently, also the intensity at the Xe M_3 edge, called edge jump, can be used to quantify the Xe coverage. In Fig. 3.15 the edge jump is shown, measured as a function of the Xe exposure time t. After 60 minutes Xe exposure the edge jump levels off due to saturation effects. Assuming that the edge jump versus t can be approximated by an exponential decay [76] it is possible to extrapolate the value of the Xe flux, using literature values for the mean penetration depth of the Auger electrons in bulk Xe [77]. The amount of Xe used in the experiment was estimated to be about 12 monolayers.

Right after Xe adsorption Rh was evaporated at T = 10K by means of an e-beam evaporator. The Rh coverage was varied in small steps up to a coverage of about 0.6ML. The Rh flux was monitored measuring the TEY current on the sample during evaporation. The conversion to ML units was based on the relation between coverage and intensity of the M_3 edge jump found in [5] for deposition of 1ML Rh on Ag(100)[1]. In the final step of BLAG the Xe layer was desorbed by annealing the sample progressively from 10K up to 150K. During each step of the BLAG the sample composition could be monitored very precisely looking at the XAS intensities Ag $M_{5,4}$, Rh $M_{3,2}$ and Xe $M_{3,2}$.

3.3.2 Co BLAG on Ag(111) and Pt(111)

VT-STM experiments were performed at the Max-Planck Institute for Solid State Research in Stuttgart, while XMCD as well as X-ray scattering and diffraction experiments were done at the ESRF. The experimental parameters Co and Xe coverage used in the different experiments are found in Table 3.2. In all the three cases the samples were prepared and measured in UHV chambers with base pressure about 10^{-10} mbar. A precise determination of temperature, Xenon and Cobalt coverage as shown below ensured the comparability of the experiments.

The Ag(111) and Pt(111) substrates were prepared by several sputtering/annealing cycles, namely sputtering at 800eV and 1.5KeV followed by annealing to 900K and 1250K, respectively and their cleanliness was verified before preparation of the samples. In the case of diffraction experiments, the crystal truncation rod was used for this purpose. The Cobalt coverage was calibrated by a microbalance in the STM measurements and by the Co edge-jump at the L_3 edge for the samples used in XMCD. A measurement of the reflectivity versus time during Co deposition was instead used at ID03. The Xenon coverage was calibrated from the partial pressure in the UHV chamber (converted to Langmuir (L) and then to film thicknesses in units of Ångströms, 5.5L $\approx$ 1ML Xe) for the STM measurements and based on the saturation of the TEY current upon Xenon adsorption for the XMCD measurements, as for the case of Xe/Ag(100) described above. Both partial pressure and reflectivity measurements were used to calibrate Xe before GISAXS and GIXRD measurements. For all the experiments the Xenon was pre-adsorbed on the sample at temperatures between 20 and 30K. Co was deposited from an e-beam evaporator. For the morphologic characterization, the sample was prepared in the manipulator and then transferred in the VT-STM, which was pre-cooled by liquid Helium flow. For magnetic characterization, the clean crystals were transferred to the magnet chamber under UHV conditions.

---

[1] A correction to the value found in [5] was included to take into account the possibility of formation of a Ag-Rh alloy for sub-monolayer amounts of Rh directly deposited on Ag(100).

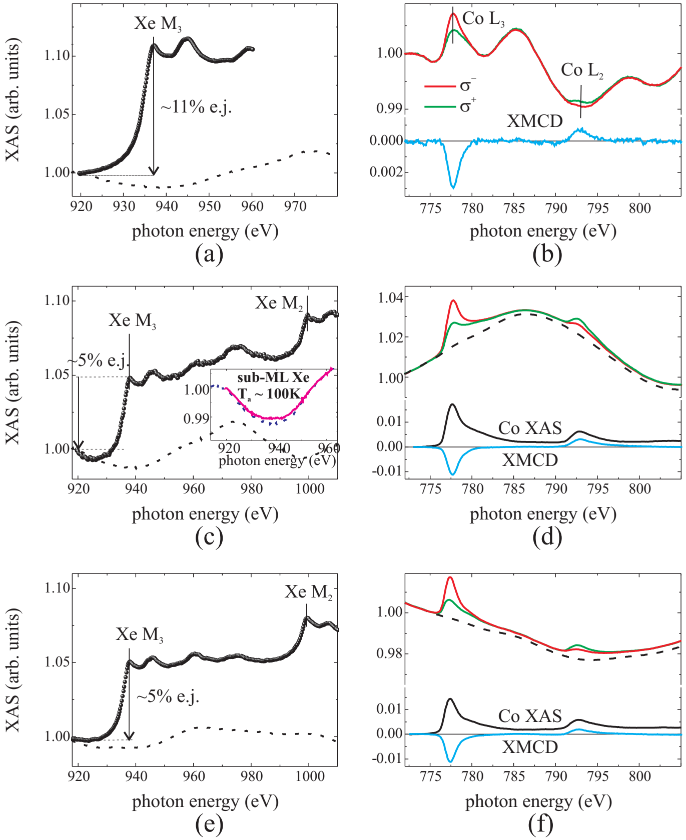

(a) (b) (c) (d) (e) (f)

Figure 3.16: XAS signal for the samples studied in Section 4.2, showing the sample composition and dichroism right after deposition of Xe and Co at 25K: Xe $M_{3,2}$ edges for 12ML Xe/Ag(111) (a), 3-4ML Xe/Ag(111) (c) and 3-4ML Xe/Pt(111) (e); in (a) and and (c) the substrate backgrounds (dashed lines) are also plotted but not in (e), where the signal was quite noisy due to the large amount of Xe. Co $L_{3,2}$ edges for 0.05ML Co/12ML Xe/Ag(111) (b), 0.08ML Co/3-4ML Xe/Ag(111) (d) and 0.06ML Co/3-4ML Xe/Pt(111) (f); dashed lines indicate the Xe/substrate system backgrounds. The inset in (c) shows the XAS taken after annealing at 100K for Xe/Ag(111) (magenta line): a small amount of Xe (sub-monolayer coverage) is still present at this temperature on the Ag(111) surface.

Table 3.2: Overview of the experimental parameters used for the samples in Chapter 4.

	STM		XMCD		GIXRD and GISAXS	
crystal	Co	Xe	Co	Xe	Co	Xe
Ag(111)	0.05ML	50L	0.05ML	12ML	2ML	50L
Ag(111)	0.05ML	5L	0.08ML	3-4ML	0.1 ML	5L,50L
Pt(111)	0.05ML	5L	0.06ML	3-4ML		

In the last step of BLAG the sample was warmed up to 100K in order to desorb the Xe from the substrate, being the nominal desorption temperature $T_{\text{des}}^{\text{substrate}}$ of the Xe monolayer from $T_{\text{des}}^{\text{Ag}} \approx$ 80K and $T_{\text{des}}^{\text{Pt}} \approx$ 110K. After annealing at 100K it was verified that no Oxygen contaminations had appeared.

In Fig. 3.16(a),(c), and (e) XAS spectra at the Xenon $M_{3,2}$ absorption edges is displayed for 12 layers of Xe adsorbed on Ag(111) and 3-4 layers of Xe on Ag(111) and Pt(111), respectively. Before Co deposition, the XAS background was also recorded at the energy range of the Co $L_{3,2}$ edge for the systems of interest: Ag(111), Pt(111) as well as Xenon/Ag(111) and Xenon/Pt(111) for the respective samples under study. In Fig. 3.16 (b), (d), and (f) the total electron yield signal is plotted for the three samples recorded right after Co deposition on the Xe/substrate-system at $T = 25$K. The background spectrum before Co evaporation is shown as a dashed line, which was used to separate the Co XAS shown in the same graph below. Also shown is the XMCD signal of Cobalt indicating a sizable magnetic moment. Hysteresis loops were measured by recording the XMCD/XAS at the L_3 edge of Cobalt as a function of magnetic field. The measurements were repeated also after annealing the sample at 100K. As one can see from the inset in Fig. 3.16 (c), a sub-monolayer amount of Xe was still present on the Ag(111) substrate at these temperatures, due to the 'pinning' of Xe atoms on the Co clusters (the 'pinning effect' will be explained in Section 4.2).

3.3.3 Co BLAG on the *h*-BN nanomesh

For this experiment the samples were prepared at the MPI in Stuttgart and then transported in air to BESSY II, in the UE-46 beamline, for XMCD measurements.

Insulating boron nitride (BN) layers on Rh(111) were prepared using stan-

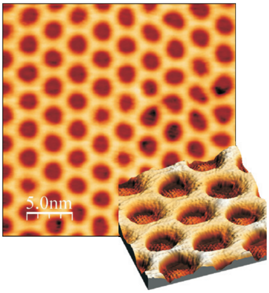

Figure 3.17: STM topography of the *h*-BN nanomesh.

dard UHV procedures. Rh(111) single crystal and Rh thin films (50-200nm) grown on YSZ[2]/Si(111) wafers were used as substrates. The latter were grown at the Universität Augsburg, Institut für Physik by Dr. S. Gsell. The cleaning procedure includes cycles of sputtering at 1.5KeV (single crystal) or 800eV (Rh/YSZ/Si(111)) followed by annealing to 1250K. The boron-nitride layer was fabricated by thermal decomposition of borazine gas, ($B_3N_3H_6$), while the Rh(111) surfaces were kept at 1250K [78]. The resulting *h*-BN layers are atomically thin, electrically insulating, chemically inert and mechanically extremely stable. They show a strain-driven hexagonally ordered corrugation with a periodicity of 3.2 nm [79,80], as can be seen in the scanning tunneling microscopy images in Fig. 3.17. Recent STM and theoretical analysis has shown that the BN layer is buckled due to epitaxial strain and only locally attached to the Rh surfaces [79], [81]. Such BN layers are commonly referred to as nanomesh but they rather resemble the shape of a muffin tin. The difference in height between the attached areas (depressions) and the detached ridges is approximately 0.55Å [81].

2D arrays of Co nano-clusters are prepared by repeated BLAG cycles on the BN, with annealing to 300K in between. After that capping materials (Au, Pt, Al_2O_3 and MnPt) are deposited *in-situ* by means of evaporators pre-calibrated by a quartz balance. The capping layer is between 2 and 3 nm. In the case of MnPt capping, during the co-deposition a blind is moved across the sample surface, resulting in a continuous MnPt wedge between 1nm to 3nm thickness. The sample is terminated with a 2nm Pt capping layer to avoid Mn oxidization. Mn/Pt ratio and quality of the wedge are verified using Auger spectroscopy. The sample structure has been checked also by means of TEM measurements. The Rh was found to be crystalline whereas the Pt capping is rather amorphous.

---

[2] yttrium-stabilized zirconia

Chapter 4

Experiments

The chapter shows three different experiments where metal nano-structures are grown using atomically flat Xe rare-gas layers.

First, several Xe layers deposited on Ag(100) have been used to study the magnetic properties of 'free' Rh nano-structures, e.g. decoupled from the substrate. The aim was to identify coordination effects that lead to occurrence or quenching of magnetism.

Second, the BLAG process itself has been investigated in detail by XMCD and VT-STM for the case of Co nano-structures. The aim was to determine the role of interactions between nano-structures and substrate in determining magnetism and morphology of the nano-structures.

Third, 2D arrays of nano-clusters have been produced by BLAG using the 'template' effect of a pre-patterned substrate, in this case the *h*-BN nanomesh. Here the focus was to study the effect of hybridization on the magnetic properties of highly ordered Co nano-clusters. Different degrees of hybridization were achieved by using various capping materials.

The description of the sample preparation in the three cases is found in Section 3.3.

4.1 Rh nano-structures

Finite magnetic moments in free clusters of a non-magnetic bulk element has been observed for the first time in Stern-Gerlach experiments with Rh clusters of less than 100 atoms [13,14]. Fig. 4.1 shows the dependence of the total magnetic moment on the cluster size. The moment formation in isolated free clusters is predicted from density functional theory but it can just as well be understood qualitatively in the framework of the Stoner criterion as discussed in Chapter 2. Of course, being able to produce free magnetic

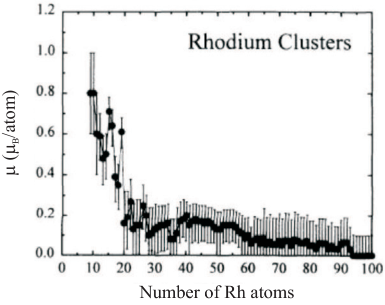

Figure 4.1: The Stern-Gerlach experiment for mass-selected Rh clusters showing the total magnetic moment versus number of Rh atoms per clusters, after Ref. [13, 14]

nano-cluster of Rh immediately raises the question if it is possible to prepare magnetic Rh nano-clusters on a supporting surface.

Indeed, according to *ab-initio* calculations the presence of a weakly interacting noble metal substrate (Ag(100) and Au(100)) should allow a residual non-vanishing magnetic moment of about $1\mu_{\mathrm{B}}$ per atom for systems like $4d$ metal impurities, small clusters and monolayers [82–93].

However, on the experimental side MOKE [94–96] and XMCD results [5] failed to confirm the presence of magnetism in Rh monolayers and sub-monolayers deposited on noble metal surfaces. While the results from MOKE experiments were not entirely conclusive due to, first, the relatively high temperature of 40K during the measurements, and, second, the low sensitivity of the technique, the XMCD results by Honolka et al. [5] performed at $l-{}^{4}$He temperatures, high magnetic fields and with high sensitivity to the magnetic moment ($0.04\mu_{\mathrm{B}}$ per atom) gave a solid proof for the full quenching of the moment in the case of Rh/Ag(100) for sub-monolayer coverages. One way to explain the discrepancies between theory and experiments is that the fragile magnetism in $4d$ metals is expected to be highly susceptible to structural parameters, which might not be adequately covered by theory. For example lattice relaxation effects in the substrate and the Rh are usually not included in the theory. Furthermore, the structure of the Rh nano-structures deposited on top of a surface is not fully known and it can be quite different from an epitaxial monolayer. Indeed it was shown theoretically that the introduction of disorder in the Rh ML system by allowing a partial Ag-Rh alloying or the formation of a second Rh layer would reduce drastically the Rh magnetic moment [93, 97].

In this work the magnetic properties of Rh have been investigated in the sub-monolayer regime on a rare gas layer by means of XMCD. The characteristic multi-step process during BLAG has been exploited to study the system in two extreme conditions, from quasi-free 'atomic-like' nano-structures (a distribution of single atoms, dimers, trimers etc.) on the non-interacting Xenon buffer layer substrate to cluster-like structures (large average Rh-Rh coordination) in contact with a weakly-interacting noble metal substrate, the Ag(100).

4.1.1 Magnetic moments of Rh/Xe

It is important to stress that, to our knowledge, these are the first successful XMCD measurements of nanoscale $4d$ systems on a rare-gas thin film. In order to obtain a sufficient signal-to-noise ratio and to trace potential artifacts in the XMCD signal of non-magnetic origin, the XMCD measurements have been repeated several times for each sample system. Moreover, since the magnetic signal in case of Rh nano-structures is close to the resolution limit of the XMCD technique for magnetic moment detection (about $0.04\mu_{\mathrm{B}}$ per atom), the XAS background at the Rh $M_{3,2}$ range on the Xe/Ag(100) was carefully recorded before Rh deposition, with and without magnetic field. Furthermore, it was verified that the Rh dichroism changes sign when reversing the magnetic field direction. Finally, to exclude unwanted time effects during the experiments it was controlled that no change in the Xe lines occurred, induced through heat input by the absorption of X-rays.

In Fig. 4.2 (a-b) the XAS and XMCD data are shown for 0.16ML Rh/Xe/Ag(100) recorded in polar geometry with $\alpha = 90°$. The background XAS of the respective Xe/Ag(100) in the $M_{3,2}$ region also shown in Fig. 4.2 (a) was subtracted from the total XAS in order to obtain the residual Rh signal, shown in Fig. 4.2 (b). The M_3 and M_2 edges (white lines) of Rh stand out clearly, together with a diffuse feature between the two peaks, which is typical for Rh. This structure has been identified in Ref. [98] for the case of bulk Rh, and is ascribed to hybridization between $4p$ and $4d$ bands at the Fermi level. In the same study the $d-d$ hybridization among Rh atoms is instead responsible for a broadening of the white line, in the bulk case. In order to gain best possible magnetic contrast, the XMCD spectra were recorded at high fields of $B = 5.5$T and low temperatures of 10K. The XMCD spectra in Fig. 4.2 (a-b) show a small but non-vanishing dichroic signal.

A non-magnetic origin of the XMCD features can be excluded for all the spectra, as they change sign when the direction of the magnetic field

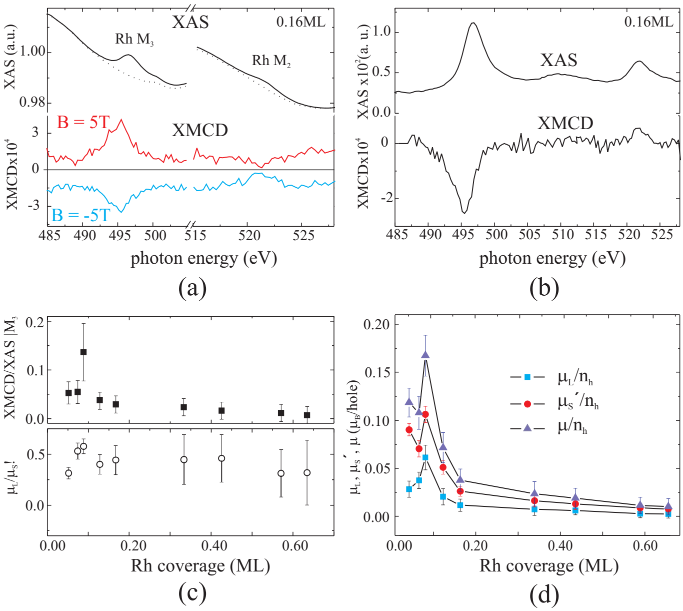

Figure 4.2: (a): XAS spectra at the Rh $M_{3,2}$ edges for a Rh coverage of 0.16 ML on Xenon on Ag(100), measured at $T = 10$K. The dotted line indicates a XAS background spectra for Xenon on Ag(100) without Rh for comparison. The corresponding dichroic signal for magnetic field in two opposite directions is also shown; (b) Rh XAS after subtraction of the background and XMCD signal; (c) XMCD over XAS at the M_3 edge (top panel) and μ_L/μ_S' ratio (lower panel), plotted versus Rh coverage; (d) average spin, orbital and total moment per hole and atom of the Rh nano-structures as a function of Rh coverage, derived from sum rules, and using the approximations explained in the text (negligible dipolar term and saturation of the magnetization assumed at 5.5T.)

is reversed (see Fig. 4.2 (a)). The measurements have been repeated for several Rh coverages, between 0.04-0.64ML of Rh. In all cases a small, non-zero XMCD signal was found (Fig. 4.3). While the XMCD at the M_3 edge is prominent for all the spectra the M_2 peak is barely visible and shows mostly in the two spectra corresponding to 0.12ML and 0.16ML coverages (see Fig. 4.2 (a) - (b)). For comparison in Fig. 4.3 the XMCD spectra for Rh impurities directly deposited on Ag(100) are shown (from Ref. [5]): for similar coverages no trace of dichroism was found.

In Fig. 4.2 (c), top panel, the XMCD over XAS peak ratio at the M_3 edge is plotted as a function of the Rh coverage. This ratio is to first approximation proportional to the sample magnetization. The amount of XMCD signal with respect to the XAS signal is between 5.3% at the smallest (0.05ML) and and 1.2% at the highest (0.64ML) coverage measured, showing a decrease of the sample magnetization with increasing amount of Rh and therefore with increasing average Rh-Rh coordination.

More quantitative information is obtained applying the XMCD sum rules described in Section 3.2.2 that allow to determine the average orbital (μ_L) and spin (μ_S) magnetic moment per hole and atom[1]. The experimentally accessible effective spin moment $\mu'_S = \mu_S + 7\mu_T$ is considered here, that also accounts for the magnetic dipole term contribution μ_T. The result is displayed in Fig. 4.2 (d), where the calculated orbital, spin and total magnetic moments per hole are plotted as a function of the Rh coverage. Increasing the amount of deposited Rh leads to a decay of both μ_L and μ'_S. For very low Rh coverages this behavior is not monotonous but there is a maximum at about 0.1ML, especially pronounced in case of the orbital part of the magnetic moment.

In Fig. 4.2 (c), bottom panel, the ratio between orbital moment and effective spin moment μ_L/μ'_S is plotted for increasing Rh coverage. Being independent of the number of holes in the Rh d-band this ratio is a reliable indicator of the relative strength of orbital and spin magnetism, which can be compared with theory or other experimental values.

In a separate experiment the dependence of magnetic moments on the degree of Rh coordination was studied using a constant coverage and then progressively desorbing the Xe from the substrate. Xe was removed by increasing the sample temperature step by step. After each annealing step the system's morphology was frozen by lowering the temperature down to 10K before performing the XMCD measurements again. In Fig. 4.4 the trend of

---

[1] The XAS integration was performed only across the $M_{3,2}$ resonances, avoiding the diffuse states between M_3 and M_2 edges. Integration was done between 490-510eV (517-527eV) for M_3 (M_2).

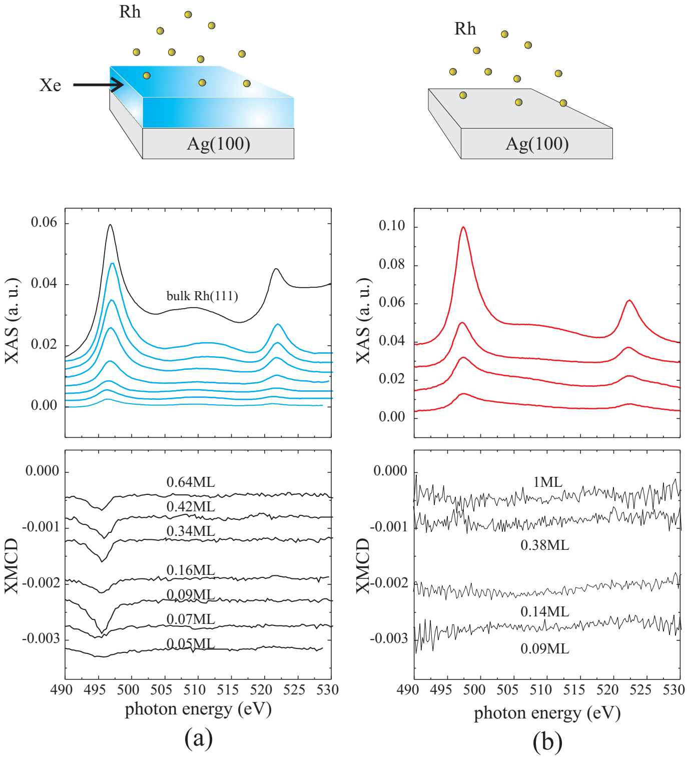

(a)

(b)

Figure 4.3: (a) XAS and XMCD spectra at the Rh $M_{3,2}$ edges for Rh coverages between 0.05 and 0.64 ML on Xenon on Ag(100), measured at $T = 10$K; (b) XAS and XMCD spectra for Rh impurities directly deposited on Ag(100) at $T = 10$K, from Ref. [5]. For clarity, the spectra have been offset in the vertical direction.

orbital and magnetic moment per hole is shown as a function of the annealing temperature, for the Rh coverage of 0.12ML. For comparison the moments found for a non-annealed sample with higher Rh coverage are shown in the same graph. The temperature during the measurements was alway 10K.

At 40K both μ_L and μ'_S are strongly reduced, but still finite. Especially the orbital moment μ_L has almost completely vanished. Above 50K the dichroism is zero. In Fig.4.4 (b) the desorption behavior of the Xe layer is schematically drawn for this range of temperature (see also Ref. [99] in the case of Xe/Ag(111)). Darker color represents larger amounts of Xe. The Xe desorption process could be monitored in the reduction of the XAS signal at the Xe $M_{3,2}$ edges (not shown). The number of Xe layers decreases from 12ML at lowest temperature to 1ML at temperatures above $T = 62$K. The Xe monolayer in direct contact with the substrate has a nominal desorption temperature between 85K and 90K. Furthermore, Xe adsorbed at step edges remain on the substrate for even higher temperatures. This residual Xe is progressively desorbed by increasing the temperature above the Xe ML desorption temperature and up to150K, where no remaining Xe is found on the surface[2].

The quenching of magnetic moment upon annealing might contain both effects of (i) increasing of the cluster size and (ii) contact with the substrate. After annealing to 40K though the Xe buffer is still present but the moment is drastically reduced. This is especially pronounced in the case of the orbital moment and is in agreement with an increase of the cluster size. The orbital moment is usually more sensitive to changes in number of neighbors then the spin moment. If one compares the magnetic moment per atom after annealing at $T = 40$K with those of the non-annealed samples then the values coincide at coverages which are a factor 4.5 larger. The value of the magnetic moment is comparable with a sample made at 10K with 4.5 times more atoms then, after comparison with the plot in Fig. 4.2 (d).

4.1.2 Discussion

First considerations

As a first estimation of the moments one can assume that $1\mu_\mathrm{B}$ per Rh atom produces an XMCD signal of about 13% with respect to the XAS intensity [100], which from Fig. 4.2 (c), upper panel, gives an average magnetic moment between 0.1 and $0.9\mu_\mathrm{B}$ per atom for the non-annealed clusters prepared on the Xe. These numbers are in very good agreement with what is

---

[2] The Xe monolayer desorption process is investigated in detail in Section 4.2 for the system Co/Xe/Ag(111) and Co/Xe/Pt(111)

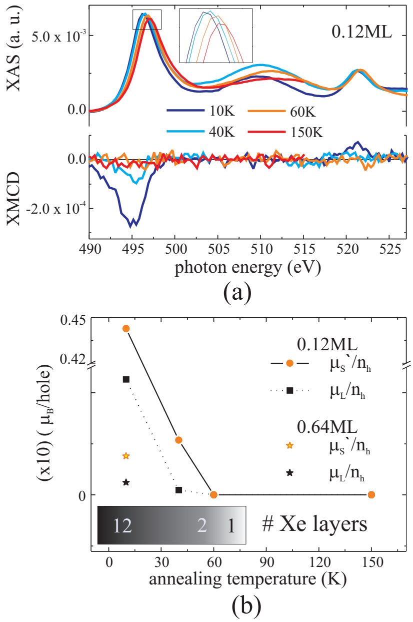

Figure 4.4: (a) XAS and XMCD signal for a sample with a fixed Rh coverage of 0.12 ML versus annealing temperature, measurement at 10K; (b) average effective spin and orbital moments per hole and atom for the same sample, as obtained from XMCD sum rules.

observed in case of free clusters shown in Fig. 4.1, where the magnetic moment is reduced from $0.8\mu_{\rm B}$ to about $0.1\mu_{\rm B}$ per atom when increasing the cluster size from 9 to 30 atoms.

The values in Fig. 4.2 (c) (lower panel) obtained for the μ_L/μ'_S ratio (average 0.4) can be directly compared with what is observed in other Rh systems, since the value does not require the knowledge of the number of holes in the d band. For Rh in Co-Rh nano-particles a value of 0.066 has been reported [101], whereas Rh in Fe-Rh nano-particles show a value between 0.03 and 0.11 [102]. In these $3d$ - $4d$ composite materials μ_L/μ'_S ratios of Rh are, thus, considerably smaller. However, when comparing these results one has to take into account that in these systems magnetic moments in Rh are known to be partly or fully induced by adjacent magnetic $3d$ metals Co and Fe. Instead, the high value found for μ_L/μ'_S in the pure Rh case indicates a strong contribution of the orbital moment to the total moment, in very good agreement with what is predicted by tight binding calculations [103, 104]. Here, the magnetic moments of fcc $\mathrm{Rh_N}$ clusters were found to be about $20 - 50\%$ of the total magnetic moment.

Effect of coordination

The decaying trend observed in the magnetic moments versus Rh coverage (Fig. 4.2 (d)) reflects the increasing nano-structure size which is accompanied by an average number of neighbors per Rh atom. It is reasonable to assume that the Rh atoms on the Xe layer form nano-structures with a narrow size distribution, as found by Monte Carlo simulations of a random deposition process for very low coverages as those used here [5]. In the simulation diffusion processes are neglected due to the low temperature of 8K during deposition. A comparison of the results found in the Stern-Gerlach experiment [13, 14] with the present experiment, especially the dramatic increase in magnetic moment below 20 atoms, seems to indicate that a coverage of 0.2ML corresponds to an average cluster size of about 20 atoms/cluster. Furthermore, since a non-zero magnetic moment was observed over the full coverage range measured, it is reasonable to assume that there was always a fraction of the Rh nano-structures with size below 100 atoms.

The oscillations of the total moment below 0.2ML of Rh reflects the high susceptibility of the magnetic moment to changes in cluster geometry. This is due to the dramatic dependence of moments on the energy level distribution around E_F for elements like Rh and Pd, which are non-magnetic in bulk but very close to fulfill the Stoner criterion (see Chapter 2). This behavior is often called weak unsaturated itinerant magnetism.

In the present experiment the μ_L/μ'_S ratio, after a slight oscillation at low coverage, stays constant within the experimental error, a sign that at large cluster sizes spin and orbital moments vary proportionally to each other (Fig. 4.2 (c) - bottom panel). This is a confirmation that not only the orbital moment but also the spin moment is strongly size dependent, typical of a non-saturated itinerant magnet. For $3d$ ferromagnetic elements instead only the orbital moment is very sensitive to the cluster size, while the spin moments are less susceptible, due to the strong exchange splitting of the $3d$ bands.

Are Rh nano-structures on Xe flat?

The oscillating behavior of the total moment observed below 0.2ML is also observed in the Stern-Gerlach experiment in Fig. 4.1 [13,14], but in that case the oscillations exhibit a shorter period. This might simply be due to the fact that on the Xenon the cluster size will be distributed and oscillations will be partly washed out. However, it may also be due to a different geometrical structure of the nano-clusters in the two experiments.

Recently, tight binding and *ab-initio* calculations [105] have addressed the problem of calculating the magnetic properties of small Rh_N clusters (with $N = 4 - 21$) having non-compact, layered structures rather then the usually assumed icosahedral structure. Surprisingly, such non-compact structures were found to have lower energy [106], and the corresponding calculated absolute values of the magnetic moment were closer to the Stern-Gerlach experiment then the values found for icosahedral-ideal clusters. For unrelaxed Rh_N structures they found a complex decreasing oscillatory behavior. The authors have calculated the trend for the total moment for several possible sequences of cluster structures representing the structural changes of a cluster with increasing number of atoms. The experimental values are in agreement with different sequences below and above the value $N = 13$, the sequence for $N > 12$ corresponding to a higher magnetization state. During the growth of a real system, there would therefore be a switching (flip-flop) of the cluster geometry at some point, in correspondence to a special symmetric arrangement, between low and high symmetry arrays.

In the present case, the trend of μ as a function of N obtained for the growth sequence identified as $S1$ in [105] (see Fig. 4.5) resembles qualitatively the experimental data in Fig. 4.2 (d): the strong peak at about 0.1ML is very similar to the one found between 10 and 15 atoms in the calculation. By using a number of holes equal to the bulk value for Rh, one finds a good agreement with the theoretical values for $N > 15$ atoms (moment below $0.1\mu_\mathrm{B}$ per atom) but not at low coverages, where the experimental values are about 3 times smaller then the calculated one. In the paper also

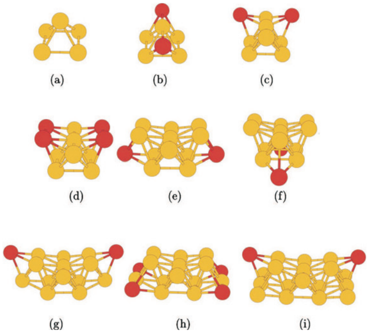

Figure 4.5: Growth sequence labeled as $S1$ in [105].

the effect of structure relaxation has been analyzed, and in general it leads to smaller values of the total magnetic moment. This might be the reason of the disagreement.

Regarding the cluster shape, it is reasonable to think that the Rh nano-structures on Xe have a rather non-spherical, flat geometry. This assumption is motivated by the fact that Xe is expected to partially move on top of the metal and cap the clusters [107]. This process can lead to structures other then spherical ones. An indication in favor of this scenario comes from the diffraction and scattering experiments for the system Co/Xe, that will be presented in Section 4.3.

Absence of magnetism in Rh/Ag(100)

In this last section the absence of magnetism in the case of Rh impurities directly deposited on Ag(100) will be discussed. Here, a key point is to understand the consequences of the interaction between Rh and Ag on the electronic properties of Rh nano-structures. Bulk Ag has the full d - band below E_F, which makes it weakly reactive, and hybridization between p and s states above E_F is negligible [98]. The interactions between Rh and Ag in the system Rh/Ag(100) take place mainly between the d_{Rh} and the sp_{Ag} states [97]. An eventual crystal field splitting of Rh states in case of a Rh-Ag substitution at the surface, would have a square-planar $D4h$ symmetry. Crystal field splitting and d - sp hybridization are both expected to show up in the experimental XAS, since they would both lead to a change of the electronic structure around the Fermi level. The effect of the d_{Rh} - sp_{Ag} interaction on the Rh electronic states could lead to an increase of d character

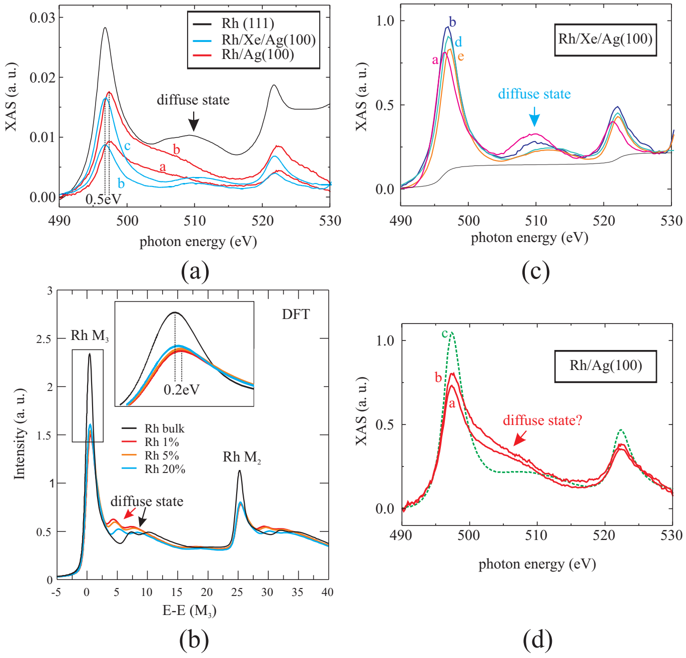

Figure 4.6: (a) Experimental XAS signal for Rh/Xe/Ag(100), Rh/Ag(100)([5]) and Rh(111); (b) DFT calculation of the XAS for a disordered bulk alloy $Ag_{(1-x)}Rh_x$ (Rh atoms diluted in the bulk bcc Ag). The inset shows a zoom-in of the graph, where the energy shift at the M_3 edge is evident; experimental XAS signal for Rh/Xe/Ag(100) (c) and Rh/Ag(100) (d). The XAS intensity has been normalized to the continuum edge jump in order to reveal eventual differences in n_h with increasing Rh-Rh and Rh-Ag coordination. The coverages corresponding to the XAS spectra are the following: Rh/Xe/Ag(100): a= 0.05ML, b= 0.16ML, c= 0.34ML, d = 0.42ML, e = 0.64ML; Rh/Ag(100): a= 0.09ML, b = 0.14ML and c = 1ML.

above E_F or to a shift of the p - like states towards E_F. From a careful analysis of the XAS shape one can understand what is happening in the system from a structural point of view.
In collaboration with the group of Prof. Ebert (Department Chemie und Biochemie, Ludwig-Maximilians-Universität München, 81377 München, Germany) we have simulated the XAS signal by *ab-initio* DFT calculations (using the Munich KKR code) in case of disordered $Rh_{(1-x)}Ag_x$ alloy (Rh atoms substituting Ag atoms in bulk Ag). The results are shown in Fig. 4.6, together with experimental data. The main characteristics of these spectra are the following:

1) The experimental XAS shape and the M_3 and M_2 resonance energies for the Rh/Xe system is always similar to bulk (Fig. 4.3). After annealing instead (Fig. 4.4) a shift of the diffuse p - d state between M_3 and M_2 towards higher energies is observed. Also the values of the energy at the resonances slightly shift in the same direction.

2) The experimental XAS shape for Rh impurities directly deposited on Ag(100) exhibits a strong change with increasing Rh coverage: a strong shift of the $p-d$ state towards lower energies at low coverages, that recovers with increasing coverage (see Fig. 4.6 (c)), and a shift to higher energies of the absorption edges as compared to bulk Rh. A similar change in the XAS line shape has been observed for $PdAl_3$ and $PdCl_4$ compared to bulk Pd [108]. In this case the effect was explained in terms of a depletion of d states in $PdAl_3$ and symmetry reasons in $PdCl_4$.

3) The simulated XAS for a diluted $Rh_{(1-x)}Ag_x$ bulk alloy: compared to bulk the Rh p - d state is shifted towards low energies for very low coverages, and it moves towards higher energies increasing Rh coverage. There is also a shift in the resonant energy. Moreover, the intensity at the M_3 absorption edge versus the continuum edge jump above the M_2 edge can give information about eventual changes in the number of holes n_h in the d band, if all the spectra are normalized to the same continuum edge jump. In Fig. 4.6 (b) one can see that the M_3 intensity decreases of a factor of about 1.7 when moving from bulk Rh towards Rh impurities diluted in bulk Ag, indication that n_h for Ag-coordinated Rh is smaller e.g. electrons from the Ag bands are filling the Rh d band.
In Fig. 4.6 (c) and (d) the experimental XAS normalized to the continuum edge jump is shown, for the two systems. Imprecisions due to the Ag and Xe/Ag background subtraction procedure do not allow for a quantitative determination of the number of holes from the data. Nevertheless one can recognize some qualitative trends in changes of the M_3 intensity as a function of the Rh-Rh or Rh-Ag coordination. From Fig. 4.6 (c) within the experimental error the increase of the Rh-Rh coordination for Rh/Xe does not lead

to significant changes in the M_3 absorption edge which points to a constant n_h. For Rh directly deposited on Ag(100) instead (Fig. 4.6 (c)), a strong difference in the XAS shape and in the M_3 intensity is observed between 0.4ML and 1ML: the XAS shape for the high coverage is more similar to the bulk Rh, and the M_3 edge is more pronounced compared to the Rh sub-monolayer case, that again indicates an increased n_h for the full Rh monolayer. This behavior is in agreement with what found by DFT simulation in Fig. 4.6.

From the above arguments one can conclude that in the case of Rh/Xe/Ag(111) the clusters are free and with an electronic structure resembling the one of bulk Rh. Annealing and Xe removal increase the cluster size, but the electronic structure remain similar to the bulk (no hybridization with the substrate). Therefore it is reasonable to conclude that the disappearance of moments while annealing above 60K discussed in Section 4.1.1 is mainly a size effect.

On the other hand, concerning the sample with Rh impurities prepared by direct deposition, the shape of the spectra points towards alloy formation between Ag and Rh after Rh deposition, even if the deposition occurred at low temperatures. In order to understand better what is the magnetic ground state of the present system, a more detailed modeling will be performed in the future. The shift of the diffuse peak towards lower energies in fact is also present (not shown here), up to a certain extent, in case of geometrical change in the Rh crystal, such as an epitaxial Rh ML on Ag(100) or bulk Rh with the Ag lattice parameter. From preliminary (not shown) results though there is indication that a non-magnetic or complex ground state is only obtained for highly Ag-coordinated Rh nano-structures, for example Rh impurities or small clusters buried under the Ag(001) surface. Such scenario is also strengthened by the observation of a reduced number of holes in the d band in sub-monolayer Rh/Ag(001), compared to the ML amount case.

The interpretation of the absence of magnetism in Rh/Ag(100) in terms of the formation of a Rh-Ag alloy would be in agreement with other theoretical calculations showing that a strongly reduced moment is expected for Rh nano-structures or ML after introduction of structural disorder, e.g. formation of partial alloys with the substrate [93, 97].

Although the energy barrier for exchange of Rh and Ag (260meV, as calculated in [109]) is much higher than the available thermal energy of 0.7meV, such processes can be induced when the impinging atoms hit the surface and locally distribute their kinetic energy. In order to explain the alloy formation in systems where the kinetic energy is lower than the energy barrier for intermixing it was proposed that the missing energy arises from the local acceleration of atoms coming from the attractive forces between the incoming adatom and surface atoms [110, 111].

4.2 BLAG of Co on Ag(111) and Pt(111)

In this section experiments are shown that aim to give an answer to the question posed in the introduction: 'What happens in BLAG if the interaction between deposited atoms and the substrate through the Xe cannot be neglected?'. In order to do that, the mechanisms driving the dynamics during BLAG are investigated in detail using Co as deposited material and Ag(111) and Pt(111) as supporting substrates, two electronically very different metal materials. The aim was to reveal the interaction between substrate and deposited material by monitoring its consequences on both cluster structure and magnetism in the early stages of BLAG, that means right after Co deposition on the Xe layers. The strategy was to combine local imaging techniques (VT-STM) with average techniques sensitive to magnetism (XMCD) and structural ordering (GIXRD and GISAXS). Furthermore, samples were prepared in the limit of thin Xe layers and sub-monolayer of Co. In these conditions in fact the dimension of the magnetic cluster system is comparable to the dimension of the contact area to the environment: the afore-mentioned interactions with surrounding materials are emphasized.

4.2.1 Cluster growth on thick Xenon buffer layers

Cluster growth and morphology

The morphology of Co clusters formed with comparatively thick Xe layers on Ag(111) was studied with VT-STM. The Xe thickness was controlled by the exposure of the clean Ag(111) substrates to Xe partial pressures in UHV at substrate temperatures of 30K. For determination of the Xe thickness an experimentally established estimate was used, 1 ML Xe = 5.5 Langmuir, from Ref. [112] (1 Langmuir = 1sec $\cdot 10^{-6}$ Torr). Thus, exposure of the substrate to 50 Langmuir (L) resulted in Xe buffer layers of approximately 9 monolayers thickness. The lattice constants of bulk Xe are incommensurate with respect to Ag(111) but aligned [113, 114]. Cobalt was deposited on the Xe buffer layer at $T = 30$K. For the samples in this section 5% of a full epitaxial Co monolayer have been deposited.

STM images were taken at different temperatures while warming up the sample to room temperature. In Fig. 4.7, STM topography images are displayed taken at temperatures of (a) 100K, (b, c) 140K, (d, e) 150K, and (f) at 300K, after full Xe desorption. The images show the gradual desorption of the Xe buffer layer, and the presence and ripening of Co clusters. In (a), small clusters of about 1-2nm diameter can already be resolved, on a rather noisy background. The overall quality of the images is reduced by the diminished electron tunneling through the noble gas as well as the weak bonds of the adlayer atoms to the substrate. However, it can clearly be seen how the Xe layer breaks up into islands surrounding the Co clusters at about 140K (Fig. 4.7 (b - c)). The boundary from a continuous to an interrupted Xe layer can best be seen at the bottom of Fig. 4.7 (c). Several hours of time had elapsed between the acquisition of images (b) and (e). From the images (b - e) one concludes that the desorption of Xe from Ag(111) occurs at temperatures above 100K. A delay of desorption of Xe is visible at defects such as substrate steps and Co clusters. The Xe is completely removed at substrate temperatures above 150K.

The Xe desorption temperature in bulk is about 55K. However, monolayer or bilayer systems of Xenon on a metal surface are thermally more stable due to increased binding forces [115]. It is therefore reasonable to assume that the desorption of Xe is a two-step process. In a first step at the bulk desorption temperature, the entire Xe layer desorbs except of the first and second monolayer that are in direct contact with the metal substrate. In a second step the residual Xe is removed by warming up the sample to higher temperatures, which are determined by the intensity of the Xe-substrate interaction. In the specific case of Xe/Ag(111) the last Xe layer remains on the surface up to 85-90K [99]. Thus, the observed desorption temperature of 150K in presence of Co nano-clusters is significantly higher than both desorption temperatures of the bulk Xe and of the Xe ML on Ag(111). The desorption process is of zeroth order, that is, the Xe does not change its phase during annealing.

Tip convolution effects make it rather difficult to derive quantitative values for the size of the clusters from topography data. Nevertheless, the temperature dependent cluster size was estimated from the number of Co atoms on the surface given the nominal Co coverage of 0.05ML and given the cluster density (from STM images). An increasing average number of atoms per cluster with temperature was obtained of about (20 ± 5) atoms at 100K, (40 ± 7) atoms at 140K and about (50 ± 5) atoms at room temperature. The given error here is the statistical error found after averaging over several topographies.

Magnetism of Co clusters on Ag(111)

As discussed in the Chapter 2 magnetic properties of nano-structures like spin and orbital moments, and in particular the magnetic anisotropy, are known to be highly susceptible to cluster size, geometry, and interface effects.

The magnetic properties of the Co clusters have been studied for a sample made with (12 ± 1) layers of Xenon and a Co coverage of 0.05ML. Fig. 4.8 (top) shows hysteresis loops taken shortly after Co deposition at two different

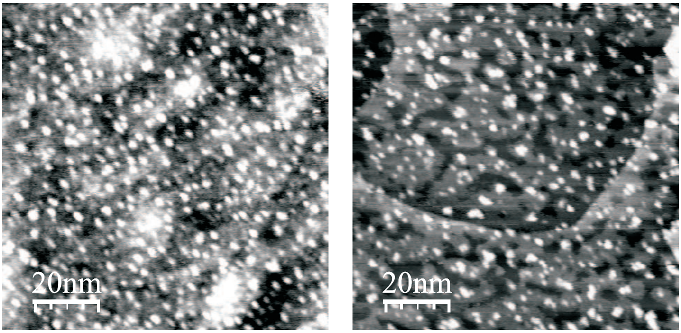

(a) $T_a = 100\pm5$ K (b) $T_a = 140\pm5$ K

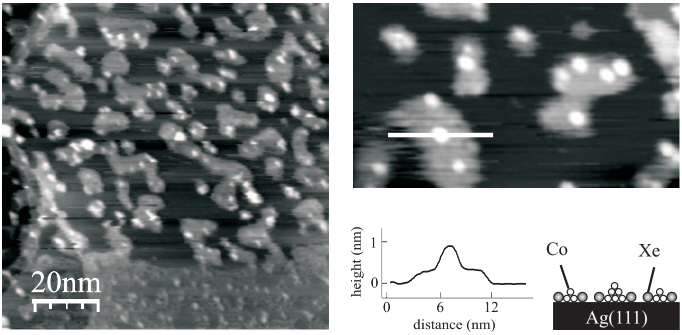
20nm
height (nm)
1
0
0
6
12
distance (nm)
Co
Xe
Ag(111)

(c) $T_a = 140\pm5$ K (d) $T_a = 150\pm5$ K

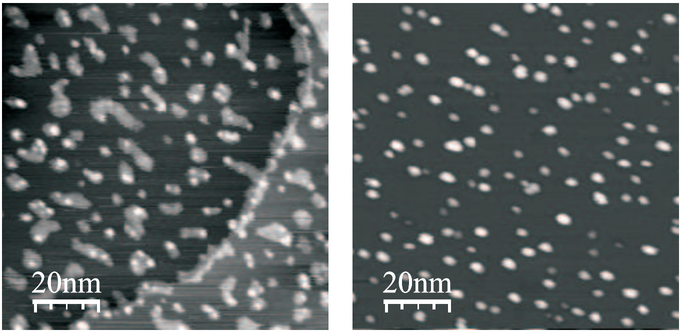

(e) $T_a = 150\pm5$ K (f) $T_a = 300\pm5$ K

Figure 4.7: STM topographies for thick Xenon buffer layers: 0.05ML Co/50L Xenon/Ag(111) deposited at 30K and then annealed at progressively higher temperatures T_a as indicated in the caption; (d) zoom-in of image (e), together with a line scan over a Co cluster and a cartoon showing the Co immersed in Xe.

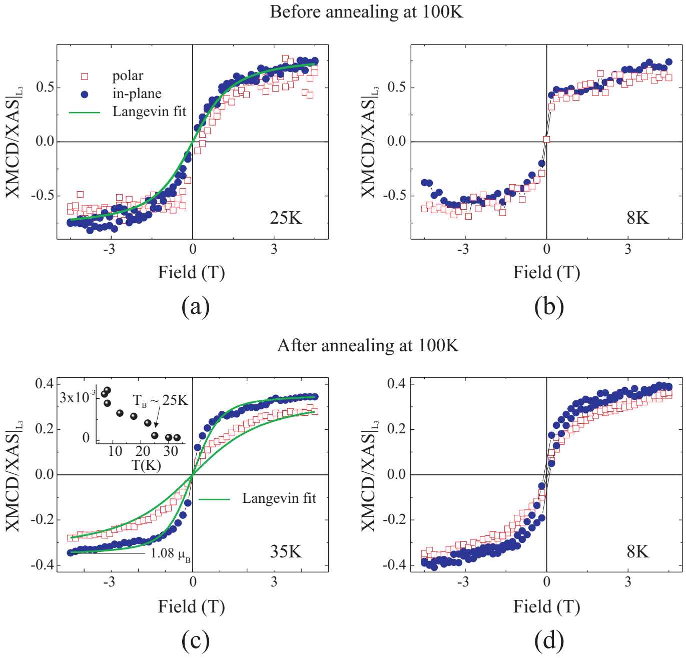

Figure 4.8: Magnetic characterization of 0.05ML Co/12 ML Xe/Ag(111) before and after annealing at 100K; (a) and (b): hysteresis loops at 25K and 8K taken right after Co deposition on the Xe buffer layer; (c) and (d): hysteresis loops at 35K and 8K taken after warming up the sample to 100K with consequent desorption of the bulk Xe, cluster growth and contact with the substrate. The inset in (c) shows quasi-remanence measurements at $B = 5\text{mT}$; the full line in the hysteresis plot corresponds to a Langevin fit according to Eq. [5] in Ref. [116].

temperatures. The ordinate is the XMCD/XAS ratio evaluated at the peak of the L_3 edge plotted versus magnetic field. To first approximation this ratio is proportional to the sample magnetization (see section 3.2.2). None of the magnetization loops in (a, b) show remanent magnetization at zero field. In addition, the loops are isotropic, i.e. they do not show any difference between polar ($\alpha = 90°$) and in-plane ($\alpha = 20°$) magnetic field directions, where α is the incidence angle that also corresponds to angle between the magnetic field and the substrate plane.

Reasons for this apparent absence of magnetic anisotropy could be an amorphous cluster structure, a random distribution of clusters orientations or even a spacial realignment of the clusters on the Xe layer in the presence of a torque created by the magnetic field. A fit to the in-plane magnetization loops with a standard Langevin function yields a spin block size $N = (35 \pm 5)$ atoms.

The scenario changes upon desorption of the Xenon when the sample is annealed up to 100K. In Fig. 4.8 (c - d) hysteresis loops are shown which are taken after Xe desorption and cooling the sample back to 35K and 8K, respectively. While the Cobalt moments exhibit no sign of anisotropy on the Xe layer, anisotropy emerges when the clusters make contact with the substrate surface. The in-plane direction now is an easy axis and we can estimate the value of the magnetic anisotropy energy ΔE_{anis} via a superparamagnetic fit (Eq. 2.16) using the procedure described in Ref. [116] assuming an uniaxial symmetry in the magnetic anisotropy. An uniaxial hard axis is obtained in the polar direction with a ΔE_{anis} of (-0.15 ± 0.1)meV/atom and a spin block size of $N = (52 \pm 5)$ atoms. The latter value is slightly larger than the cluster size of about 20-40 atoms found in Section 4.2.1. However, there is still reasonable agreement, an indication that the thermodynamic model employed to describe the nano-clusters magnetization is reasonable for the nano-cluster system. Further, an upper limit to the blocking temperature of the clusters is obtained from temperature dependent measurements of the magnetization at very small applied fields of $B = 5$mT shown in the inset of Fig. 4.8(c). From the temperature at which the magnetization disappears one finds $T_{\mathrm{B}} \leqslant (25 \pm 5)$K.

The moments per d-band hole derived from the XMCD data using the sum rules (Section 3.2.2, Eqs. 3.38 and 3.39) are summarized in Table 4.1. Unfortunately in the case of Co situated on thick Xe layers the signal-to-noise ratio in the XMCD was insufficient for a quantitative evaluation of the moments.

For the case of Co clusters after annealing at 100K instead, the effective spin and orbital moments could be calculated independently and compared with the Co hcp bulk values given in [68] about $0.6\mu_{\mathrm{B}}$ per hole for the spin moment and about $0.06\mu_{\mathrm{B}}$ per hole for the orbital moment. For small nano-structures both spin and orbital moments are expected to be enhanced respect to the bulk values, as explained in Chapter 2. Here instead, only the orbital moment is enhanced whereas the effective spin moment is surprisingly smaller than the bulk value, even if one takes into account the intra-atomic dipolar moment μ_T which has a maximum value of about $0.02\mu_\mathbf{B}$ per atom in these systems (see the calculated values in Section 4.2.3).

Errors in the data evaluation due to a non-complete saturation of the magnetization only amount to a 5-10% as seen from the hysteresis curves. Errors due to the background subtraction in this case are also small and all together gives an error of about a maximum 20%. The Co was not oxidized, as seen from the XAS line shape and self-absorption processes can be neglected in case of very small clusters.

Therefore, this seems to be a real effect due to either the cluster crystalline geometry or/and an effect induced by contact with the metallic substrate. In the following paragraphs will be shown that this effect is also present, in a smaller extent, in case of Co nano-clusters on Ag(111) and on Pt(111). A detailed discussion of the possible physical origins will be given in Section 4.2.4.

Table 4.1: Magnetic properties of 0.05ML Co/12 ML Xe/Ag(111) before and after annealing at 100K. The average magnetic moments given in units of μ_B have been calculated from the saturated XMCD data at $T = 8$K using the sum rules, with the magnetic field in-plane and polar with respect to the surface normal. The value of the XMCD/XAS ratio at the L_3 absorption edge is also indicated.

BLAG stage	$\frac{\mu_\mathrm{L}}{n_\mathrm{h}}$	$\frac{(\mu_\mathrm{S}+7\mu_\mathrm{T})}{n_\mathrm{h}}$	$\frac{\mathrm{XMCD}}{\mathrm{XAS}}$
before annealing at 100K			
in-plane (8K)	-	-	0.74
polar (8K)	-	-	0.64
after annealing at 100K			
in-plane (8K)	0.08	0.46	0.40
polar (8K)	0.07	0.33	0.36

4.2.2 BLAG with atomically thin Xenon layers

Co cluster morphology on Ag(111) and Pt(111)

In order to address the question if atoms or clusters interact with the substrate long before the last monolayer of the noble gas is desorbed the extreme

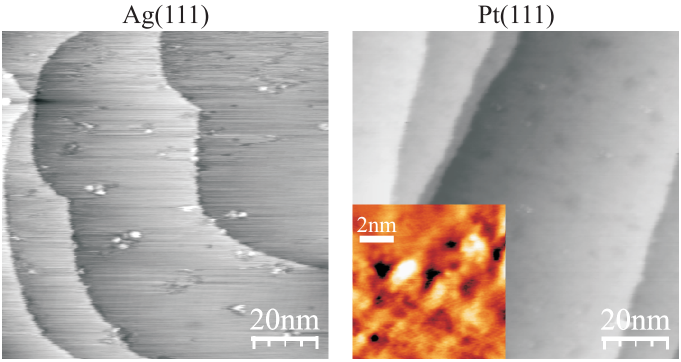
Ag(111)
Pt(111)
20nm
2nm
20nm

(a) T_a = 80±5 K (b) T_a = 80±5 K

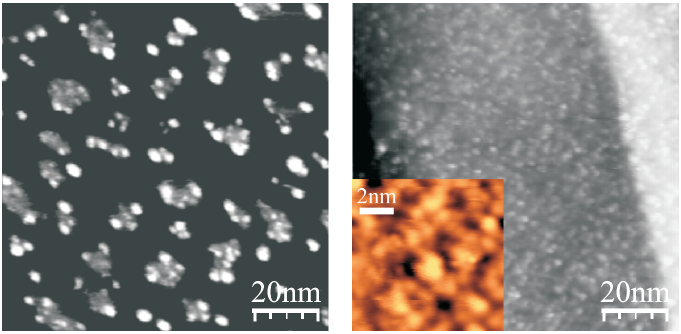
20nm
2nm
20nm

(c) T_a = 120±5 K (d) T_a = 110±5 K

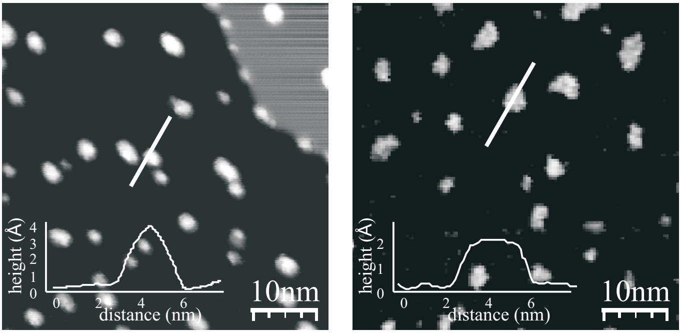
height (Å)
0
1
2
3
4
0
2
4
6
distance (nm)
10nm
height (Å)
0
1
2
0
2
4
6
distance (nm)
10nm

(e) T_a = 300±5 K (f) T_a = 300±5 K

Figure 4.9: STM topographies for 0.05ML Co/5L Xe/Ag(111) (left column) and 0.05ML Co/5L Xe/Pt(111) (right column) taken after annealing at T_a indicated in the figure caption. The scanning temperature was 20K for (a - d) and 300K for (e) and (f). The inset in (e) and (f) shows the line scan across a Co island supported on the two different substrates.

case of BLAG with only a single layer (5 Langmuir) of Xenon was studied. As substrates Ag(111) and Pt(111) were used. The Co coverage was again 5% of an epitaxial monolayer, in analogy to the samples in the previous section.
Xe grows on Pt(111) as a commensurate layer below coverages of $\Theta \simeq 0.33$ ML. At higher coverages a transition from commensurate to incommensurate occurs that leads to a final hexagonal incommensurate rotated 2D solid phase [117]. As for Xe/Ag(111), also for Xe/Pt(111) the desorption is a zero-order transition [118]. The Xe desorption temperature for 1 ML Xe/Pt(111) is about 100-107K, which is significantly higher then on Ag(111), due to the higher binding energy [118].

STM images taken on 0.05 ML Co/1 ML Xe/Ag(111), as well as on 0.05 ML Co/1 ML Xe/Pt(111), in the temperature range between 80K and 300K are summarized in Fig. 4.9.
At low temperatures, when the complete Xe monolayer is still adsorbed and cluster formation is in its early stage, the clusters can be hardly distinguished from the Xe background (see Fig. 4.9 (a - b)). In the case of Ag(111) (Fig. 4.9 (a)) one observes streaks in the STM which points to a displacement of mobile Co clusters or Xe atoms by field-induced diffusion while scanning the tip over the surface. Terrace step edges as well as defects and vacancies in the Xe layer provide an energetically favorable position where the Co clusters are more strongly bound and therefore immobile.
On the Ag(111) surface a behavior similar to that observed in the previous paragraph for thicker Xenon films at comparable temperatures (Fig. 4.7 (e)) occurs, that is residual Xe on the surface is pinned at Co clusters up to 150K. For the BLAG on Pt(111) the dynamics is different. No streaks are observed at the lowest temperature in Fig. 4.9 (b) but an increase of the apparent height corrugation when moving from 80K ($\Delta h \approx 0.2 - 0.4$Å, Fig. 4.9(b)) to 110K ($\Delta h \approx 0.6$Å, Fig. 4.9(d)) and finally 150K ($\Delta h \approx 1.6$Å, not shown). The conclusion from these and many other STM images is that the clusters are actually buried in the Xe and become more and more exposed as the Xe layer desorbs.
Further increase of the temperature up to RT (Fig. 4.9 (e - f)) produces in both cases an increase of the cluster size accompanied by a reduction of density as observed in Fig. 4.7 (f). For Ag(111) the clusters are of double layer height and the average cluster size estimated from the STM data is now $N = (16 \pm 5)$ at 110K and $N = (44 \pm 5)$ at RT. On the Pt(111) surface islands are found to have monolayer height with an average number of atoms that changes from $N = (6 \pm 2)$ at 120K to $N = (60 \pm 5)$ at RT. One can conclude that using constant BLAG parameters the system dependent growth dynamics lead to structures with substantially different properties on

the two substrates: small compact 3D structures on the Ag(111) (Fig. 4.9 (d)) and monolayer islands for the Pt(111) (Fig. 4.9 (e)).

From these experiments it is clear that the substrate does have considerable influence during buffer layer assisted growth and contributes to the final size, shape and distribution of the clusters, in contrast to what has been reported so far.

Comparison of the magnetism of Co clusters on Ag(111) and Pt(111) substrates

The magnetism of all samples in this Section 4.2.2 have been investigated by XMCD. Angular dependent X-ray absorption spectra at the Co $L_{3,2}$ edges have been recorded as functions of temperature and magnetic field. The clusters here have been synthesized by BLAG using 3-4ML Xe and a Co coverage of 0.08ML for Ag(111) and 0.06ML for Pt(111).

The complete set of magnetic moments calculated from the XMCD data are shown in Table 4.2, before and after annealing at 100K. The XMCD was measured at magnetic fields of $B = 4.5$T. The hysteresis loops obtained on those samples along the sample normal and under grazing incidence are summarized in Fig. 4.10, again before and after annealing to 100K. While for clusters situated on Xenon/Ag(111) the magnetization is isotropic (Fig. 4.10 (a)), in analogy to what is observed in Fig. 4.8 for the case of thick buffer layers, clusters on Xenon/Pt(111) show a strikingly pronounced magnetic easy axis in the polar direction (Fig. 4.10 (b)), which endorses the STM interpretation of a stronger tendency of Cobalt to penetrate the Xenon. After annealing both samples at $T = 100$K and measuring again at 25K and 8K (Fig. 4.10 (c - d)) in both cases Ag(111) and Pt(111) a magnetic anisotropy is visible in the magnetization curves: while Co/Pt(111) still has a strong polar easy axis, Co prefers the in-plane direction in the case of the Ag(111) substrate.

The ΔE_{anis} was estimated in the superparamagnetic regime from the Co magnetization loops on Pt(111) at 25K, and on Ag(111) at 8K, using the fitting procedure described earlier. A ΔE_{anis} of +0.6 meV/atom and +0.67 meV/atom for Co/Pt before and after annealing at 100K, and -0.10 meV/atom for Co/Ag. An additional average induced moment per Co atom due to the three Platinum nearest neighbors atoms $m_{\mathrm{Pt}} = 0.15\mu_{\mathrm{B}}$/atom [119] was included in the calculation. For the spin block size one then gets $N = (17 \pm 5)$ for Pt(111) and $N = (25 \pm 5)$ for Ag(111) before annealing and $N = (18 \pm 5)$ for Pt(111) and $N = (15 \pm 5)$ for Ag(111) after annealing at 100K. Remanence is observed at lowest temperatures of 8K in the case of the Pt(111) substrate due to the strong polar magnetic anisotropy which

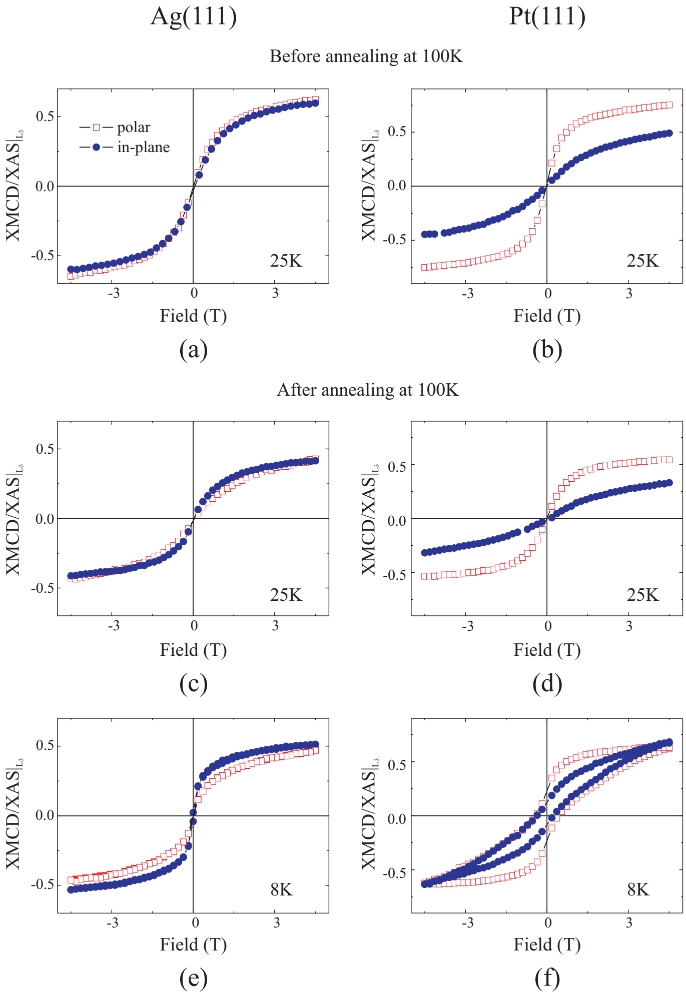

Figure 4.10: Magnetic characterization of the systems in Fig. 4.9: 0.05ML Co/3-4ML Xe/Ag(111) (left) and 0.05ML Co/3-4ML Xe/Pt(111) (right): (a) and (b) before annealing at 100K; (c - f) after annealing at 100K, measured at 25K and 8K.

pushes the blocking temperature to higher values.

From the values of the orbital and effective spin moments given in Table 4.2 one can see that, in analogy to what is observed for Co clusters made with a thick Xe layer (Section 4.2.1), the effective spin moments are not enhanced compared to the bulk value and in some cases they are even slightly smaller. The reduction of the spin moment in case of Co clusters prepared with a thin Xe layer is weaker compared to the case of a thick Xe layer and it is found to be more pronounced for Co clusters on the Ag(111) substrate than on the Pt(111) substrate. This is an indication of a dependence of the effect on the number of atoms in the cluster, which is larger for clusters made with a thick Xe layer and very small in case of clusters on Pt(111).

Table 4.2: Magnetic properties for the samples 0.05ML Co/3-4 ML Xe/Ag(111) and 0.05ML Co/3-4 ML Xe/Pt(111) before and after annealing at 100K. The average magnetic moments given in units μ_B have been calculated from the saturated XMCD data at the indicated temperatures using the sum rules, with the magnetic field in-plane and polar with respect to the surface normal. The value of the XMCD/XAS ratio at the L_3 absorption edge is also indicated.

sample	$\frac{\mu_L}{n_h}$	$\frac{(\mu_S+7\mu_T)}{n_h}$	$\frac{\text{XMCD}}{\text{XAS}}$
before annealing at 100K			
Ag(111) in-plane (30K)	0.10	0.53	0.60
Ag(111) polar (30K)	0.11	0.60	0.65
Pt(111) in-plane (30K)	-	-	0.45
Pt(111) polar (30K)	0.16	0.54	0.76
after annealing at 100K			
Ag(111) in-plane (5K)	0.11	0.49	0.51
Ag(111) polar (5K)	-	-	0.46
Pt(111) in-plane (5K)	-	-	0.38
Pt(111) polar (5K)	0.12	0.57	0.61

4.2.3 *Ab-initio* calculations of magnetic Co$_N$ islands on Ag(111) and Pt(111)

In order to interpret the experimentally observed trends in the magnetic properties of these deposited Co clusters *ab-initio* calculations have been performed by Sven Bornemann (Department Chemie und Biochemie, Ludwig-Maximilians-Universität München, 81377 München, Germany). The scheme used in the calculations is the local density approximation of density functional theory (DFT) [120], using the spin-polarised relativistic Korringa-Kohn-Rostoker multiple scattering formalism [121]. The influence of coordination effects on the magnetism of the deposited Co clusters was studied by a systematic increase of the island size.

Table 4.3 shows the calculated magnetic spin (μ_S), orbital (μ_L), intra-atomic dipolar moment (μ_T) and magneto-crystalline anisotropy energy. with the exception of Co_3 and Co_7 where the anisotropy is slightly in-plane but with a value close to zero. These exceptions reflect oscillations of the magnetic anisotropy for the smallest cluster sizes. More interestingly for Co/Ag(111) a strong out-of plane anisotropy energy is observed for the single atom case of $10.98\frac{\mathrm{meV}}{\mathrm{atom}}$, which is highly sensitive to a lateral coordination with other Cobalt atoms: a sudden easy axis reorientation to the in-plane direction is predicted for the Co dimer case accompanied by an abrupt drop in the MAE absolute value to $-1.23\frac{\mathrm{meV}}{\mathrm{atom}}$. After that, adding more atoms leaves the easy axis direction in-plane and the MAE varies only slightly with increasing number of atoms in the first layer, until reaching the ML value of -1.62meV/atom. Stacking of Co atoms in a second layer reduces the absolute MAE value dramatically (almost a factor of 10), but does not change the easy axis direction for islands with more then 1 atom. The positive MAE in the case of Co4 (three atoms in the first layer and one atom in the second) is due to the single Co atom in the second layer.

A third layer of Co does not substantially change the situation anymore.

Concerning the spin and orbital moments, one can see that they both decrease if the number of atoms in the island is increased, an effect known also from the literature [119, 122]. The intra-atomic dipolar term decreases progressively in absolute value with increasing number of layers, indicating that the distribution of the magnetic moment is becoming isotropic when the cluster is becoming more compact.

4.2.4 Discussion

Growth dynamics of Co nano-structures on Xenon buffer layers

Key observations regarding the growth of Co on thick and thin Xe layers from the presented VT-STM experiments are (i) the observation of delayed Xe desorption in the vicinity of the Co clusters, (ii) differences in the cluster-substrate interaction for Ag and Pt substrates, resulting in a considerably stronger tendency for clusters to penetrate the Xe matrix for the case of Pt substrates, (iii) differences in the cluster morphology on Ag and Pt substrates, as well as cluster ripening during annealing of the samples to room

Table 4.3: *Ab-initio* calculations for the systems Co/Pt(111) and Co/Ag(111) calculated for ML height Co island with increasing number of atoms and for bi-layer and tri-layer height islands. The calculations have been performed by Sven Bornemann (Department Chemie und Biochemie, Ludwig-Maximilians-Universität München, 81377 München, Germany). In the table average values for magnetic anisotropy (in meV per atom) and magnetic spin, orbital and intra-atomic dipolar moment (in μ_B per atom) are reported. Positive (negative) values for the MAE indicate out-of-plane (in-plane) easy axes.

sample	MAE	μ_S	μ_L	μ_T
ML cluster/Pt(111)				
Co1	4.88	2.269	0.604	-0.209
Co2	2.24	2.160	0.441	-0.045
Co3	-0.12	2.081	0.234	-0.088
Co7	-0.25	2.024	0.192	-0.025
Co19	0.22	1.967	0.168	
Co37	0.24	1.947	0.160	-0.047
ML cluster/Ag(111)				
Co1	10.98	2.145	1.350	-0.023
Co2	-1.23	2.050	0.506	0.012
Co3	-2.71	2.009	0.410	0.012
Co7	-2.91	1.954	0.243	0.030
Co19	-1.60	1.915	0.221	-0.015
Co37	-1.78	1.899	0.214	-0.018
monolayer	-1.62	1.872	0.186	-0.027
bi-layer cluster/Ag(111)				
Co4	0.70	2.022	0.571	0.005
Co10	-0.235	1.921	0.277	0.016
Co31	-0.34	1.895	0.217	-0.006
Co64	-0.234	1.884	0.209	-0.007
tri-layer cluster/Ag(111)				
Co39	-0.42	1.899	0.221	0.003
Co82	-0.21	1.888	0.210	0.0002

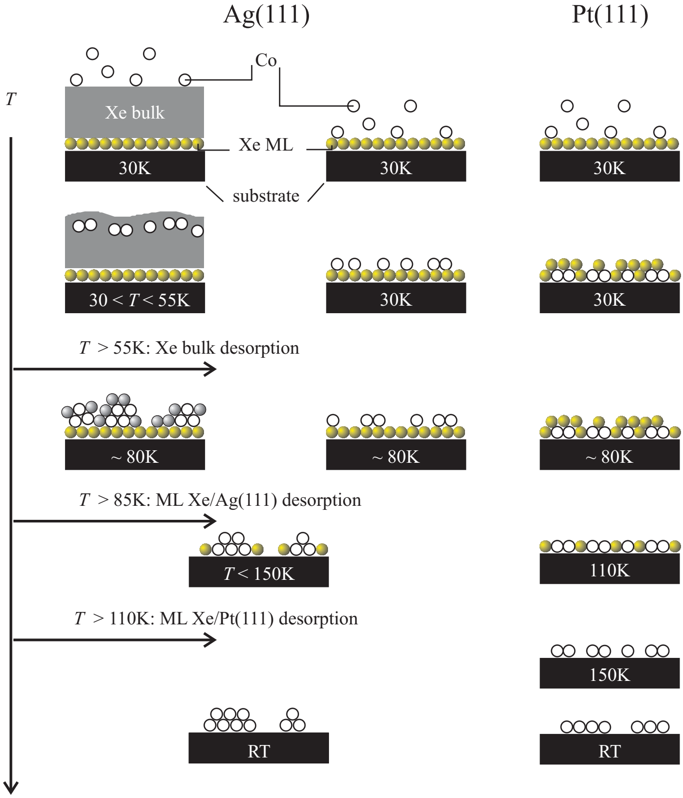
Ag(111)
Pt(111)
Co
T
Xe bulk
Xe ML
30K
30K
30K
substrate
30 < T < 55K
30K
30K
T > 55K: Xe bulk desorption
~ 80K
~ 80K
~ 80K
T > 85K: ML Xe/Ag(111) desorption
T < 150K
110K
T > 110K: ML Xe/Pt(111) desorption
150K
RT
RT

Figure 4.11: Detailed scheme of the cluster formation dynamics for the three different samples: Co/thick Xe buffer layer/Ag(111) (left), Co/Xe ML/Ag(111) (center), and Co/Xe ML /Pt(111) (right). The arrow indicates the raising temperature T from top to bottom.

temperature. The details of Xe desorption and cluster formation will be now discussed in more detail.

One of the most widely used concepts for thin film and cluster growth is the consideration of surface or interface energies of substrates and adlayers [123]. The interfacial energy γ^0_{AB} at the interface of two materials A and B is commonly expressed as $\gamma^0_{AB} = \gamma^0_A + \gamma^0_B + \Delta\gamma^{\text{ads}}_{AB}$, where γ^0_i is the surface free energy of material i and $\Delta\gamma^{\text{ads}}_{AB}$ the interfacial adhesion of the system AB. The $\Delta\gamma^{\text{ads}}_{AB}$ can be calculated for metal/Xe and metal/metal systems, using values for the surface free energy and interfacial adhesion from Ref. [123]. One obtains interfacial energies γ^0_{AB} of 2.33J/m^2, 0.23J/m^2, and 0.007J/m^2 for Co/Xe, Co/Ag and Co/Pt, respectively. The gain in free energy upon formation of an interface between two materials can be written as: $\Delta\gamma = \gamma^0_A + \gamma^0_{AB} - \gamma^0_B$. This formula simply expresses a comparison between the total free energy of the system in two different states: an in initial state where the element B is exposed to vacuum and a final state where the element A is exposed to vacuum in one side and is wetting B in the other side. The AB interface substitutes the B-vacuum interface in the final state. Negative or very small values of $\Delta\gamma$ indicate that the formation of the interface is favored energetically and therefore a layer by layer growth is expected. In the present case, for A=Co one finds the values 1.53J/m^2 and 0.007J/m^2 for the two substrates B=Ag and Pt, respectively, that is Co wets Pt(111) but not Ag(111). Concerning the Xe/Co interface, $\Delta\gamma = -0.188$J/m^2 for Xe wetting the Co surface (A=Xe and B=Co). As already discussed in [107] for the case of Au nanoparticles on Xe, these results suggest that the Xe will coat the Co nanoparticles in order to minimize the surface energy. In the next Section 4.3 will be shown experimental results that reinforce this interpretation.

Similar energy considerations can also be used to predict the morphology of the clusters in equilibrium. The Young-Dupré formula for a liquid droplet on a solid relates the contact angle θ of a droplet to the surface free energies of the solid and liquid, and the interfacial energy of the solid-liquid system: $\gamma^0_{\text{S}} = \gamma^0_{\text{SL}} + \gamma^0_{\text{L}} \cos\theta$. Special cases are complete wetting for $\theta = 0°$, and a crossover from wetting to dewetting for $\theta = 90°$.

Evaluating the Co cluster morphology with this approach predicts total wetting for Co/Pt ($\theta = 0°$), partial wetting for Co/Ag ($\theta = 66.4°$), and dewetting for Co/Xe ($\theta = 154°$). According to this estimate, the formation of a Co/metal substrate interface seems energetically most favorable, which could potentially destabilize three-layer Co/Xe/metal system.

Thus, the analysis of the surface free energies explains very well the experimental observation of the formation of hemispherical Co clusters on Xe/Ag for thick Xe layer, and the differences of the cluster morphology after making contact with the Ag and Pt surface. Especially on the Pt(111) the strong tendency towards complete wetting results in the formation of monoatomically flat, epitaxial islands.

For a better understanding of the temperature dependent dynamics during BLAG it is instructive to compare the desorption energies of Xe in different environments. The desorption energy for bulk Xe is about 170meV per Xenon atom [124–126], while for a single Xe monolayer on on Ag(111) the desorption energy is 208meV/atom [127], and 286meV/atom for 1ML of Xe on Pt(111) [118]. As already introduced in Section 4.2.1, the higher desorption energy for single Xe monolayers is due to interactions with the supporting substrate. Using the same argument, in the vicinity of surface step edges or clusters at the surfaces the Xe desorption can be delayed to even higher temperatures due to a higher coordination with the metal atoms, as seen in the STM images of Sections 4.2.1 and 4.2.2. A similar pinning effect has been reported for Ag clusters, soft-landed on a Kr buffer layer [128].

A difference in desorption energy between bulk Xe and a Xe monolayer adsorbed on a metal is expected to influence the growth mode of Co when directly deposited on Xe. The morphology of the two samples made with Ag(111) substrates and different Xe coverages suggests that Co coating by Xe atoms occurs on the bulk Xe, where the Xe desorption energy is lower. On the Xe single layer on Ag(111) instead Co atoms seem to simply diffuse on the Xe layer but with a higher diffusion coefficient compared to e.g. a metal surface. A very special case is the Xe single layer on Pt(111), where the desorption energy is higher then on Ag(111) but the deposition of Co destroys the ML structure.

As a matter of fact, the required evaporation heat per atom for a single Xe monolayer is determined by intralayer Xe-Xe interactions, as well as Xe-substrate interactions. There are two different contributions to the Xe-Xe intralayer interactions, which are attractive van-der-Waals interaction and a repulsive contribution originating in the interaction between Xe and the substrate. The total lateral binding energy for 1ML Xe/Ag(111) was reported to be 54.37meV/atom [127]. Strain effects or the formation of induced dipoles in the Xe layer, for instance, can in fact increase the described repulsive contribution, hence weakening the total Xe-Xe interaction. The measured surface dipoles for Xe/Ag(111) is 0.2D [129]), which corresponds to an average repulsive contribution of about 7meV/Xe atom. For Xe/Pt(111), the induced dipole moment in the Xe layer is considerably higher, namely 0.53D, corresponding to an increased repulsive energy per Xe atom of 19meV [130]. The higher surface dipole, together with other effects such as a higher work function, an unfilled *d* band, and stronger corrugation of the Pt(111) surface potential, contributes to a total lateral binding energy per Xe atom which is

reduced by 30meV/atom, compared to Ag(111) [117,131].
One can argue here that the observation of Co cluster embedding in the Xe layer is a result of the described weakened Xe-Xe bonds, that results in an effective attractive interaction between the Co and the metal substrate.
This detailed discussion is summarized by the model of cluster formation in Fig. 4.11. The presented comparison of BLAG on Pt and Ag substrates thus shows that the substrate can have a significant influence on the final size and shape of the clusters, as it determines the bond strength in a thin buffer layer, cluster-substrate interactions as well as the wetting behavior. As a result of the differences in BLAG, in the early stages of cluster formation Co clusters on Pt(111) tend to be smaller and of flat shape, in comparison to Ag(111) substrates where the same BLAG parameters result in larger clusters of hemispherical shape.
The above discussion is summarized in the growth model displayed in Fig. 4.11.

Analysis of the magnetic properties during Co self-assembly - Comparison to *ab-initio* theory

In this section the measured magnetization as well as evaluated orbital and effective spin moments of the Co nano-structures during the different steps of BLAG (Table 4.1- 4.2) are discussed in more detail since they allow for a correlation with the morphology information extracted from STM. Table 4.4 shows an overview of magnetic moments in relevant geometries calculated with *ab-initio* theory together with the values obtained from the XMCD sum rules.

First qualitative trends can be seen in the XMCD/XAS values at magnetic fields $B = 4.5$T given in Table 4.1-4.2. As shown in Section 2 the magnetic moment is reduced as $3d$ clusters grow in size. Indeed, the XMCD/XAS values reflecting the average magnetization M are always smaller after Xe desorption, when the cluster size N is increased. When comparing M before Xe desorption then among the three measured samples Cobalt on 12ML of Xe possesses the highest XMCD/XAS value of ≈ 0.7 in average but shows no magnetic anisotropy. This is coherent with the picture that smallest clusters on a the thick Xe layer are electronically decoupled from the substrates. The same amount of Co on only 3.5ML of Xe on Ag(111) shows already a slightly lower XMCD/XAS value of ≈ 0.6 in average but still no magnetic anisotropy. Finally the sample with 3.5ML Xe on Pt(111) shows a similar value of XMCD/XAS≈ 0.6 in average but a rather strong magnetic anisotropy.
In the following a discussion will be done about orbital moments which are

Table 4.4: Average magnetic moments per atom in units μ_B for 0.05ML Co on different substrates measured in the direction of the easy axis. These values are compared with the theory values for epitaxial monolayer and bilayer island. The number of holes in the *d* band was assumed to be n_h =2.49. Magnetic moments and magnetic anisotropy energies are given in units of μ_B and meV, respectively.

sample	$\frac{\mu_L}{atom}$	$\frac{(\mu_S+7\mu_T)}{atom}$	ΔE_{anis}/atom	N	size from STM
thick Xe layer/Ag(111)					
before annealing at 100K (25K)				(35±5)	
after annealing at 100K (8K)	(0.20±0.1)	(1.14±0.1)			
after annealing at 100K (35K)	0.21	0.87	(-0.15±0.1)	(52±5)	(40±7)
thin Xe layer/Ag(111)					
before annealing at 100K (25K)	0.28	1.49	isotropic	(25±5)	
after annealing at 100K (8K)	0.27	1.22	-0.10	(18±4)	
after annealing at 100K (25K)	0.27	0.93			(16±5)
thin Xe layer/Pt(111)					
before annealing at 100K (25K)	0.39	1.35	0.4	(17±5)	
after annealing at 100K (8K)	0.29	1.43	-	-	
after annealing at 100K (25K)	0.25	1.20	0.67	(18±5)	(6±4)
theory	μ_L/atom	μ_S/atom	MAE/atom		
Co10/Ag(111) double	0.277	1.921	-0.235	10	
Co31/Ag(111) double	0.217	1.895	-0.34	31	
Co19/Pt(111) mono	0.168	1.967	0.22	19	
Co37/Pt(111) mono	0.160	1.947	0.24	37	

related to magnetic anisotropy effects, and trends in the spin moments.

Magnetic anisotropy and orbital moments: As discussed in Section 2.1 the MAE originates from anisotropies of the orbital moments via the spin-orbit coupling constant ξ, as given in Eq. 2.7. In general a reduction of the Co orbital moments points to a trend towards bulk electronic structures. In the case of surface-supported Co clusters this effect can be due to hybridization between Co d states with sp and d bands of the substrate and to internal d-d hybridization within the cluster. The latter of course increases with the average cluster size. In Table 4.3 the quenching effect on μ_L with increasing cluster sizes is also shown by DFT theory.
Hybridization effects from the substrate are expected to be smaller for Ag(111) compared to Pt(111), since in the former case the full d band is shifted far below the Fermi level. Again this is reflected in the *ab-initio* calculations, where for a given cluster geometry the orbital moments are higher for the case of Ag(111).

In the case of Co on Ag(111) made with a thick Xe layer the decrease of orbital moment upon desorption at 100K is therefore mainly due to the internal d-d hybridization of the Co with increasing number of Co-Co neighbors in the cluster: the nano-magnets become larger, which is also seen in the spin block size N that increases (see Table 4.4). In the same way the larger orbital moment and smaller N after annealing at 100K for the sample prepared on Ag(111) with thin Xe layers suggests a smaller cluster size, in agreement with both our STM investigation and the findings by Weaver *et al.*. However, the error margin in the orbital moment evaluation is relatively large. Nevertheless, also the absolute values $\mu_\mathrm{L} = 0.27\mu_\mathrm{B}$ per atom measured on Ag(111) are in good agreement with the calculations of bi-layer islands of the experimentally derived cluster sizes $N = 16$ (estimation from STM) and $N = 18$ (spin block size): from Table 4.3 we expect μ_L to be $0.22 - 0.28\mu_\mathrm{B}$.

In the case of Pt(111) *ab-initio* theory of monolayer islands with spin block sizes $N = 25 - 30$ underestimates μ_L by about 30%. However, using the cluster size $N \approx 6$ estimated from STM leads to a much better agreement between experiment and theory. In the case of the Co/Xe/Pt(111) system one can also compare the present results to what was found by Gambardella *et al.* [17] for Co on Pt(111). A monolayer island of 7-8 atoms has a MAE of about 1meV/atom and an orbital moment of about $0.35\mu_\mathrm{B}$/atom. Within the experimental errors, those numbers agree well with that of BLAG-grown Co clusters.

The well pronounced polar magnetic anisotropy observed already right after Co deposition on the Xe layer as compared to the lack of anisotropy for Co/Xe/Ag(111) indicates that in the first case the Co atoms and nano-structures cannot be considered as free. As discussed in Ref. [17], this effect can only occur in presence of a broken symmetry, that means a chemical bond with the Pt(111) surface. In line with what is discussed in the previous section on the STM results, it is proposed that Co penetrates the few Xe layers already at 25K to make contact with the substrate.

Spin moments: The theoretical values of μ_S in Table 4.3 show that depending on the substrate the average spin moment is expected to decrease monotonously up to 14% when going from Co_1 to Co_{31} monolayer islands. In agreement with this trend, the experimentally determined effective spin moments ($\mu_S + 7\mu_T$) in Table 4.4 are larger for the samples made with a thin buffer layer, where clusters are expected to be smaller. However, absolute experimental spin moments μ_S (the contribution of the intra-atomic magnetic dipole moment μ_T was accounted for using theory values in Table 4.3) are smaller then those calculated for small clusters. For example in the case of Co islands on Pt(111) one finds spin moments of only $\mu_S = 1.76\mu_B$/atom compared to the values $\mu_S = 1.96\mu_B$/atom predicted by the calculations. The experimental value is thus more comparable to bulk values of $1.62\mu_B$/atom [132], where the spin moment is known to be reduced due to the large degree of Co-Co coordination. For the samples made on Ag(111) one even finds Co spin moments which are below the bulk value. When comparing the Co/thin Xe buffer layer/Ag(111) sample before and after bulk Xe desorption it is concluded that in the case of Ag(111) the reduction of the spin moment is worsened with Xe desorption. The calculated spin values for ML cluster geometries in Table 4.3 support the more pronounced quenching effect for Ag(111) substrates although the magnitude is underestimated. In the following possible reasons for the small values of the average spin moments in Co clusters will be discussed.

1) Structural effects

The geometry of the clusters produced in the gas phase might play a role. In [133] for example it was found that fcc mass selected clusters, deposited on Au(111), have a spin moment of only about $1.5\mu_B$ per atom, similar to the value found here. The clusters are quite large (about 8nm in diameter) but small enough to show an enhancement of the orbital moment. Furthermore, according to [134] epitaxial Co islands on Au(111) with a similar size should still exhibit an enhancement of the spin moment compared to bulk. The reduced spin moment found in fcc cluster might therefore be connected with the geometry of the clusters, which differs from the arrangement of atoms in nano-structures grown epitaxially on a substrate. Diffraction experiment that will be presented in the next paragraph have shown that Co on Xe has both the hexagonal and cubic phases (bulk Co is hcp) and that the process of Xe desorption favors the formation of the cubic phase. Therefore there might be some similarities between the properties of Co clusters produced in the gas phase, confirmed by a similar enhancement of the orbital moment (0.2 that are connected with a low spin phase of Co. The similar enhancement of the orbital moment observed in [133], might give an explanation for the lack of spin moment enhancement for Co clusters on thin Xe on Ag(111).

The further decrease of spin moment upon Xe desorption and contact with the substrate in case of Ag(111) could be due to both an increase of the percentage of fcc clusters and/or an effect induced by the substate.
On Pt(111) since the Co penetrates the Xe layer the contact with the substrate occurs on a very early stage. One might still think that the structure obtained in this way is quite different from an epitaxial island obtained upon direct deposition of Co on Pt(111). This would be surprising though, given the ML height of the island seen in STM experiments and the small number of atoms. Therefore in this case an interpretation of the spin moment reduction in terms of a substrate mediated effect seems to be more adequate.
In the following, substrate mediated effects will be discussed.

2) Substrate-mediated effects

A quenching of the spin moment of Co in contact with a non-magnetic metal has been found earlier for Co nano-clusters embedded in a Cu matrix [135,136]. The authors could attribute the effect to the cluster-matrix hybridization and presence of Rudermann-Kittel-Kasuya-Yosida (RKKY) type cluster-cluster interactions. In the present case, however, this explanation is excluded for two reasons. First, the average distances between clusters are larger then 2nm which makes the RKKY inter-cluster interaction negligible. To give an order of magnitude, for Co_{32} clusters embedded in a Cu matrix [137] and cluster-cluster distances between 2nm and 3nm, calculated RKKY oscillations give interaction energies between 0.03meV and 0.005meV, respectively. At experimental temperatures of 8K (0.7meV) used here these interactions should not play a role. The second argument is the trend of magnetization versus cluster size and density: the magnetization is smaller for the sample made with 50L Xe, which corresponds to larger clusters with smaller cluster density. Instead in Ref. [136] it was found that, as a consequence of cluster-cluster interactions, the magnetization increases with the cluster size and, for a given size, decreases with the cluster concentration.

Screening effects due to polarization of the Ag atoms surrounding the Co cluster is another possible explanation of the reduced spin moments. Recently, in an experiment on Co nano-particles embedded in a Ag matrix [138], Ag atoms were shown to exhibit a non-vanishing dichroic signal in an external magnetic field of 1Tesla. The same was observed for Au and Cu capped clusters. Although the induced noble metal moments in the presence of Co atoms point in the same direction as those of Co, charge transfer processes between Co and noble metal need to be taken into account, which leads to incomplete filling of the Ag *d* bands and can decrease the average Co moments. The same authors in fact report a value of the magnetization of Co clusters embedded in Cu and Au matrices which is similar or below the bulk value [139, 140], somehow in agreement with what observed in the present work.

Even though Co and Ag are immiscible, different scenarios might appear for deposition of minute amounts on surfaces [141]. Co-Ag intermixing could lead to the formation of a magnetically dead layer at the interface between clusters and Ag(111), with consequent reduction of the Co magnetic moment. This has been observed for example for Co/Ag multilayer [142], where the Co moment of a 1nm thick Co layer was found to be quite small (about $1\mu_\mathrm{B}$ per atom). Furthermore, according to calculations in [143] the spin moment of Co-Ag alloys could be reduced compared to the Co hcp bulk value, depending on the geometry and composition of the alloy, down to a value of about $1.3\mu_\mathrm{B}$ per atom.

Finally the possibility of a non-collinear alignment the Co moments inside the cluster is considered, which can lead to a reduction of the average spin moments. Among other reasons non-collinear magnetism can be induced by the Dzyaloshinski-Moriya (DM) term, also called 'anisotropic exchange interaction'. This term is usually only important in the case of weak exchange interactions between magnetic atoms, which is why it is not taken into account in most ferromagnetic systems. In contrary, recently it was calculated for Co dimers on a Pt(111) substrate with strong spin-orbit coupling [144] that a non-collinear spin-structure could be stabilized. In particular the authors suggest that DM couplings can affect the spin structure around the edges of larger nano-structures like those studied in this work.

In conclusion the experiments of Co/Xe gave two main results: first that the BLAG concept is not universal but depends strongly on the mutual interactions between substrate, rare gas atoms and deposited material. In some extreme cases where the interaction with the substrate is very high, as for the Pt(111) substrate, the BLAG fails in the sense that the deposited atoms destroy the order of the rare gas layer; second the experiments confirmed that the magnetism of small aggregates of atoms is a very sensitive physical quantity, that can change a lot depending on the substrate properties. In particular magnetic anisotropy was found to appear only when contact between clusters and substrate occurs and the spin moment of Co atoms are strongly affected by the presence of the substrate.

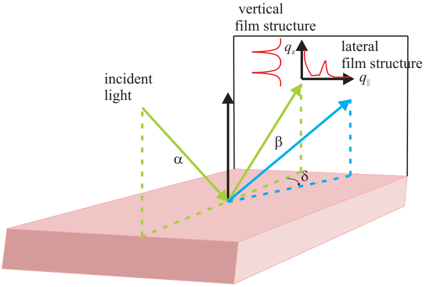

Figure 4.12: X-ray diffraction and scattering geometry.

4.3 GIXRD and GISAXS measurements

In addition to the information acquired with VT-STM and XMCD techniques, surface diffraction and scattering measurements have been performed for the system Co/Xe/Ag(111), to further investigate the crystal structure and the growth dynamics of Co nano-structures during the whole BLAG process. Measurements have been done with Co coverages in the mono- and sub-monolayer range. In the latter case, the growth of Co has been investigated in two different conditions: full decoupling from the substrate (thick Xe layer) and partial coupling (thin Xe layer).

With the aim of investigating the atomic structure of the interfaces of the system Co/Xe/Ag(111) it is useful to briefly look at what is known about the properties of the parts composing the system. Synchrotron X-ray diffraction experiments on the system Xe/Ag(111) have been performed in Ref. [114]. They found that layer by layer growth is achievable only up to a maximum number of layers $N = 8$, that depends on the substrate temperature, the growth rate (Xe partial pressure) and the quality of Ag(111) crystal. Concerning the structure of the Xe films, those grown in quasi-equilibrium conditions exhibit two domains of stacking: the ABC sequence according to the fcc structure and another one rotated 60 degrees with respect to the surface normal. Non-equilibrium grown films instead show a large fraction of ABA stacking faults, that are believed to be located mainly in the interfacial region. About the structure of the deposited Co there are no reference measurements but it is worth to remember that even if Co is *hcp* in bulk, Co nano-clusters with only a few nanometers in diameter behave differently. The high surface/volume ratio and relaxation of interactomic distances can in fact affect the cluster crystal structure. As an example it has been calculated that for particles smaller then 20nm in diameter, the ground state for the particle structure is the *fcc* phase [145].

4.3.1 Growth of monolayer coverges of Co on atomically flat Xe layers

From δ and reflectivity scans (for explanation see Section 3.2 and Fig. 4.12) information on the in-plane and out-of-plane system ordering is obtained. Specifically grain size and structure but also characteristics of the interfaces Co/Xe, Xe/Ag(111) and Co/Ag(111) can be extracted.

The Kiessig fringes in the reflectivity curves in Fig. 4.13 (b) shows the onset of crystalline ordering of the Xe(111) film along the direction normal to the sample surface, after annealing at 30K (cyan curve). From the oscillation period of the Kiessig fringes, one can easily estimate the total thickness t of the film (see Section 3.2.1). For this sample the Xe layer thickness was found to be $t \approx 6$ML. The high degree of order of the Xe film is destroyed upon deposition of Co (magenta curve), as it is visible from the damping of the oscillation intensity. Furthermore, the increased periodicity of the Kiessig fringes suggests that the Xe film became thinner as a consequence of the Co deposition. In this case, a loss of about 25% is estimated.

This effect could be explained by hot Co atoms impinging on the surface that locally increase the temperature of the Xe film and therefore triggers Xenon desorption. One can estimate the temperature of a Co atom impinging on the substrate from the Co deposition rate. Experimental data of this dependence in the case of Co sublimation are reported in Ref. [146]. Deposition rates used in our experiments are between 0.06ML/minute and 0.3ML/minute, that give us an average kinetic energy $< E_{\mathrm{K}} >= \frac{3}{2}k_{\mathrm{B}}T$ of about 130meV. This value has to be compared with the heat of sublimation of a Xe atom in the bulk Xe that is about 170meV [124–126]. The energy required to sublimate the Xe is therefore higher then the estimated average energy that can be transferred from the hot Co atoms to the solid. Nevertheless, the kinetic energy is certainly enough to provoke a re-arrangement of the structure (by creation of defects) even towards a less ordered state. Furthermore, also the period of the interference fringes localized around the positions at $L = 2$ and $L = 4$ (see Fig. 4.13 (b)) show a reduction of the period of about 20% after Co deposition. These fringes correspond to the bulk Xe Bragg peaks and therefore their period is sensitive to the number of ordered layers of the film, as it is the case for non-infinite crystalline films. Thus a change in the periodicity here is an indication that the crystalline structure of the film has changed; in this case, since the periodicity has increased, towards a lower

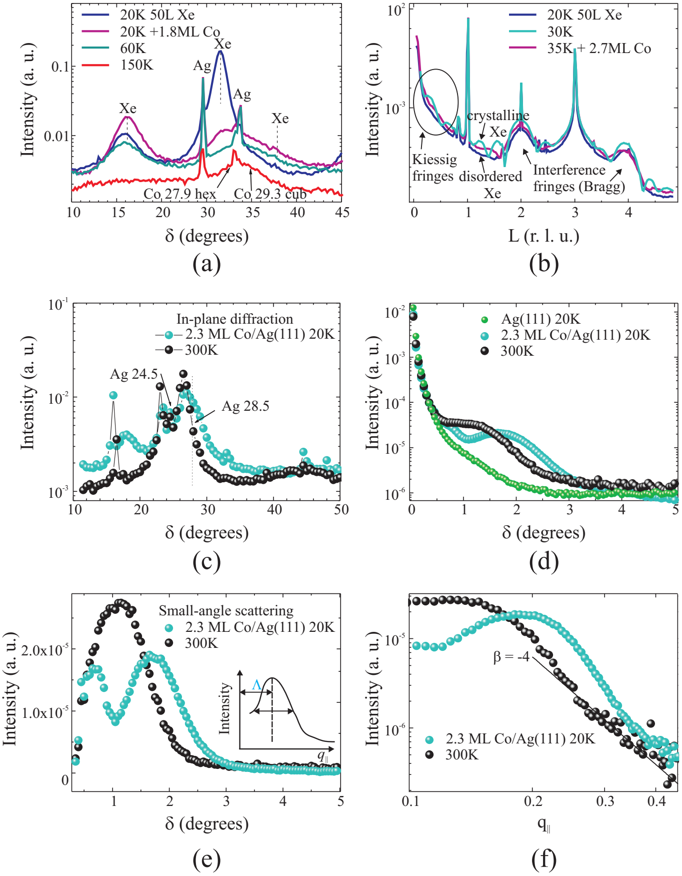

Figure 4.13: X-ray diffraction of 2ML Co/50L Xe/Ag(111): (a) in-plane scans and (b) reflectivity versus the z component of the momentum transfer L defined in 3.24, expressed in reciprocal lattice units (r. l. u.) of the surface (b); Direct deposition of 2.2ML Co on Ag(111) at 20K followed by annealing to RT: (c) in-plane scans, (d - e) small angle scattering scans versus δ before (d) and after (e) background substraction and finally versus $q_{||}$ (f).

number of ordered layers.

In-plane δ scans, at an incidence angle α and exit angle δ (see Fig. 4.12) are shown in Fig. 4.13 (a) for 2ML of Co evaporated at 20K on 50L of Xe/Ag(111). They probe the in-plane crystal structure of the adlayers during BLAG. Xe was also absorbed at 20K. The deposition of Co (magenta colored data) on the Xe film induces a drop of the intensity of the Xe peak at $\delta = 26.7°$, corresponding to the $< 220 >$ orientation, but an increase of the peak at lower values $\delta = 16.2°$, corresponding to the $< 111 >$ direction. This indicates most likely a rearrangement of the Xe layer structure due to the impact of Co atoms. In particular as already pointed out in the last sections, due to surface energy gain, Xe most likely coats the Co nano-structures, which reduces the amount of ordered layers of Xe, in agreement with what is observed in the reflectivity scans.

A multi-Gaussian fitting procedure was used to fit the diffracted intensity line shape in the δ-scans, with two sets of curves corresponding to the peak distribution of Co in the hexagonal phase or in the cubic phase. It was found that Co on Xe has both cubic and hexagonal phases with the former being more abundant. Together with Xe desorption, the peak corresponding to the cubic phase becomes narrower (larger grains) whereas the hexagonal phase is unchanged.

For comparison, in-plane diffraction measurements have been repeated for 2.3 ML of Co grown directly on Ag(111) at 20K and then annealed to 300K (Fig. 4.13 (c)). At low temperatures again both hexagonal and cubic phase are present, represented by the broad peak with a maximum around $\delta = 27°$. A peak at lower values of δ, between $\delta = 17°$ and $\delta = 20°$ is also observed. This peak is not tabulated in the hcp and fcc distributions, therefore it might be corresponding to an amorphous phase of Co coexisting with the ordered phases at low temperatures. After annealing to room temperature this peak disappears. The center of the Co peak distribution moves towards lower δ after annealing. The spectral distribution observed in the δ scans at RT resembles the hcp one, with peaks at $\delta = 21.9°, 24.8°, 26°, 28° \text{and} 32°$. Therefore the thermally activated diffusion on the Ag(111) surface seems to favor the formation of *hcp* structures.

On the same sample also GISAXS scans were performed. The results are shown in Fig. 4.13 (d-f). From the position of the peak in intensity and the FWHM in Fig. 4.13 (e) one finds the following values for the average diameter d and inter-particle distance L, according to Eq. 3.33: $L = (18 \pm 2)$Å and $d = (23 \pm 1)$Å at $T = 20$K, indicating overlap between particles and $L = (26 \pm 1)$Å and $d = (24 \pm 1)$Å after annealing to 300K.

From the power law $I \sim q^{\beta}$ at high q values (Fig. 4.13 (f)) instead one can get information about the particle structure (see Section 3.2.1). The power law after annealing to room temperature is $\beta = -4$, coinciding with the Porod's law in Eq. 3.29 for perfectly spherical particles, with negligible interaction between them. The value found at low temperatures instead indicates a more complex structure of the domains, possibly with no sharp boundary between them. Dendritic shape has indeed been observed for sub-monolayer coverages of Co deposited on Ag(111) at temperatures between 160 to 200K [147]. The feature at small q in the low temperature scan might indicate interaction between particles.

4.3.2 Growth of sub-monolayer coverages of Co on Xe/Ag(111)

The growth dynamics of Co nano-structures made with coverages of only $5 - 10\%$ of a monolayer on 50L Xe and 5L Xe films has been monitored by GISAXS measurements. The aim was to reveal whether there are differences in the growth mode of the same amount of Co atoms on different Xe buffer layer thicknesses. These samples are prepared under the same conditions as those investigated in Section 4.2.
The scans have been normalized to the Bragg peak amplitude and the background signal from the clean Ag(111) single crystal was subtracted. Since the GISAXS intensity depends on the roughness of the surface, the scans taken during the different steps of BLAG monitor changes in the morphology of the films. The range of δ values was between 0 and 5 degrees. This corresponds to an observation window R (see Section 3.2.1) between 200Åand 10Å. The window defines the range of sizes in real space to which the measurements are sensitive.

In Fig. 4.14 GISAXS scans are plotted on a log-log scale for Co sub-monolayer samples made with 5L and 50L of Xenon as a function of the momentum transfer q in the surface plane. The scans have been taken during the different BLAG steps, namely after Xe adsorption at 20K, annealing to 35K, deposition of sub-monolayer amounts of Co and progressive annealing in several steps up to room temperature. In Fig. 4.14 (a-b) the full q range is displayed for both samples. One can distinguish two distinct regimes where the scattered intensity follows a specific power law, connected by a kink where the behavior is exponential. These regimes are at $q < 0.15$ Å^{-1} and $q > 0.25$ Å^{-1}, in the following referred to as small q regime' and 'high q regime', respectively. They are plotted independently in Fig. 4.14 (c-e). These two regimes correspond to different observation windows, describing changes in the Xe-Ag interface (between 15nm and 4nm) at small q and Co-Xe-Ag interface (below 4nm) at high q.
Let's now describe in detail what happens to the system in the two different

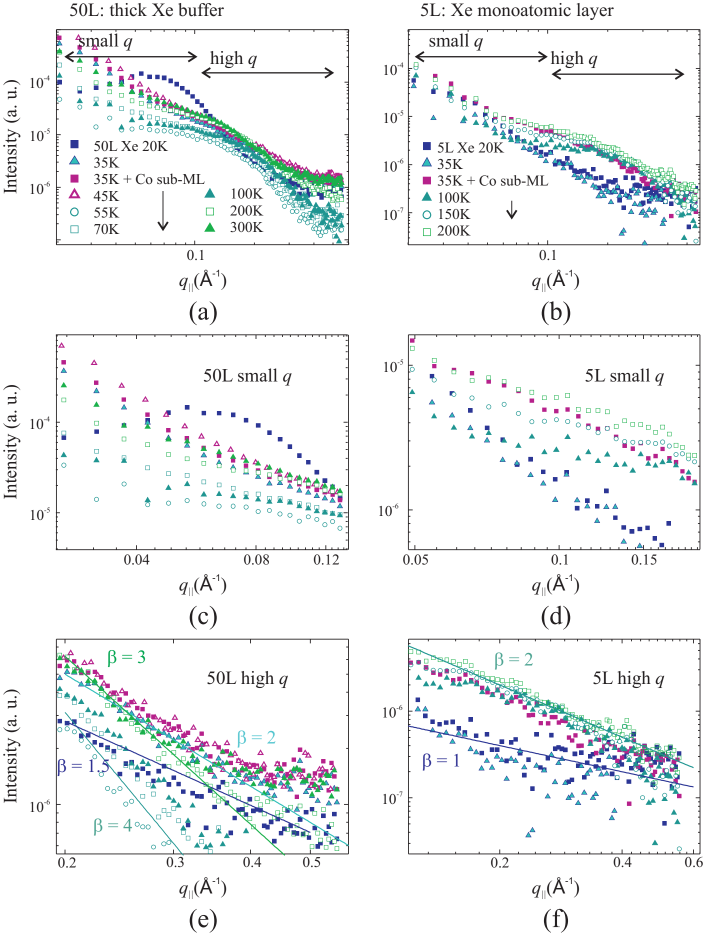

Figure 4.14: GISAXS scans during BLAG of sub-monolayer coverage of Co on (a) 50L Xe, label ’50L’ and (b) 5L Xe (b), label ’5L’. The plots in (c, e) and (d, f) are zoom-ins of the measurements in (a) and (b), respectively, to show the trend in the small q (c - d) and high q (e - f) regions for the two samples in more detail.

regimes, during the BLAG steps.

Small q regime

In the small q regime scattering measurements are sensitive to both the Xe film structure (domain size and roughness) and the Co nano-particles $S(q)$ (see Section 3.2.1). From the VT-STM investigation in Section 4.2 the latter are known to have a (non uniform) size of few nanometers and to be randomly distributed over the surface.

Thus, it is reasonable to think that in this range the Xe roughness dominates the signal, being the Xe layer(s) highly ordered and the amount of Xe much larger than the amount of Co. In other words, peaks in the GISAXS scans like those in Fig. 4.13 (e) for large Co particles are not expected to be found, in the present case. On the other hand changes on the Xe layer, for example in correspondence with Co deposition, indirectly provide information about the Co growth mode.

The first step of BLAG is the adsorption of Xe on the cold substrate. In the case of 50L Xenon (c) the GISAXS of pure Xe measured at $T = 20$K (blue navy symbols) and $T = 35$K (turquoise symbols) are very different, whereas for 5L Xe (d) they are quite similar. This reflects the ordering process of Xe thick buffer layers that is also observed in reflectivity data (Fig. 4.13). The range of q tells that the Xe roughness (domain size) before annealing is above 4 nm, the size corresponding to $q_{\max}$.

The second step is deposition sub-monolayer amounts of Co on the Xe (magenta symbols). During deposition the intensity does not change for the 50L sample, whereas it increases strongly for 5L Xe sample. This significant difference must reflect differences in the growth mode, depending on the Xe thickness.

The third step is to progressively anneal the samples up to room temperature. For the 5L sample, we observe a drop of the intensity at 100K, that is about to the nominal desorption temperature of a Xe single layer adsorbed on Ag(111) [99]. When the sample is further annealed to $T = 200$K the intensity recovers to the same value that was found at 35K after Co deposition. A similar behavior is found for the sample with 50L. Here, though, we have more steps, due to the multi-step desorption process for multi-layer Xe (see Section 4.2.1). Annealing to 45K leaves the sample unchanged, whereas a drop of the intensity follows the Xe multi-layer desorption occurring at about 55K; then, after a slight increase of the intensity upon annealing to 70K another drop is found at 100K. After that, the intensity increases progressively up to 300K, where it has similar values as after Co deposition on Xe at 35K.

High q regime

In this regime one is sensitive to the interface between Co and the underlying substrate, that is Xe before and Ag after Xe desorption. Here, the spatial distribution of the particles does not affect the signal, as explained in Section 3.2.1.

For the 5L Xe sample, the data show a power law dependence with exponent β = - 1 for Xe/Ag(111), also after annealing to 35K, and β = -2 after Co deposition. No other changes are observed in this range, up to 200K.

For the 50L Xe sample a more complex scenario is found: Xe adsorbed on the sample after annealing at 35K has β = - 2, and the same exponent can be used to describe the scattered intensity after Co deposition and annealing to 45K. A strong change occurs instead after desorption of the Xe multilayer: the exponent is in this case β = - 4 (Porod's law!). This power law is retained up to 100K. Further annealing to 200K and then 300K leads to weaker exponents, β = - 3 and β = -2, respectively. In Fig. 4.15 the trend of β with temperature is summarized, for both samples.

4.3.3 Discussion

For samples made with about 2ML of Co, the most interesting result is the change observed in the Xe structure upon deposition of Co. This might be due to a coating of the Co by Xenon, that would reduce the number of Xe layers in the ordered phase and/or the desorption of a fraction of the Xe multilayer upon contact with 'hot' Co atoms. Concerning Co, it could be shown that Co on Xe has both cubic and hexagonal phases with the former being more abundant. The process of Xe desorption favors the growth of clusters with cubic phase.

Instead for Co directly deposited at low temperatures on Ag(111), a mixture between hexagonal-cubic and amorphous phases is found. The structure of the film is possibly granular, with no well defined boundaries between grains. Annealing to RT provokes a structural transition with selection of the hexagonal structure and formation of spherical, well separated clusters, without a strong ripening.

For the system made with sub-monolayer coverages of Co, the following conclusions can be drawn concerning the dynamics of the BLAG process in the two cases of thick and thin Xe layers:

1) In both cases annealing between 70K and 200K has the same effect of increasing the scattered GISAXS intensity at small q and therefore increasing

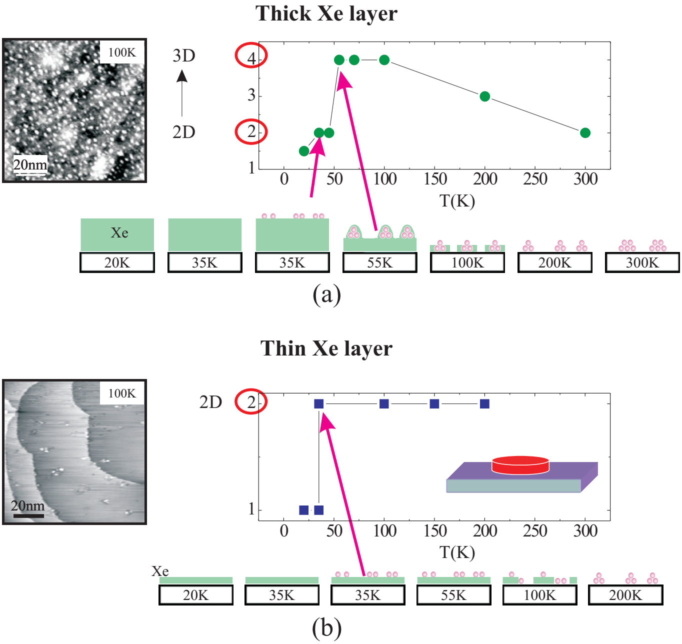

Figure 4.15: Critical exponent β for the two systems Co/thick Xe/Ag(111) (a) and Co/thin Xe/Ag(111) (b), plotted for the different stages of BLAG. STM topographies showing the system morphology after annealing at 100K are also included.

the surface roughness. Being in a q regime corresponding to the size of Xe domains, it is reasonable to think that these changes are due to a progressive melting of the Xe ML. This gradual increase of roughness is observed at temperatures considerably higher than the nominal temperature for desorption of the Xe monolayer which is about 85K. Therefore one can speculate that this trend in the GISAXS data coincides with the pinning effect of the Co clusters on the Xe atoms observed by VT-STM in the previous section (Section 4.2)

2) The effect of Co deposition on the scattered intensity is surprisingly different for the two samples and suggest a different growth mode in the two cases. The increase of roughness over the full q range for the 5L Xe sample suggests that in this case the Co atoms form small aggregates on the Xe ML with very different electronic density as compared to the Xe. On the other hand, on the 50L Xe sample, the absence of any 'reaction' in the intensity after Co deposition would suggest an epitaxial growth. This cannot be the case though, due to energetic reasons: the Co does not wet the Xe (see Section 4.2). It is more reasonable to imagine that Co atoms are capped by Xe, as already discussed for ML amounts of Co on Xe.

3) Annealing to 55K after Co deposition for the 50L Xe sample leads to Xe multi-layer desorption. As a consequence, the roughness is lower (the Xe ML is perfectly epitaxial, whereas the multi-layer structure can have many defects) and the power law at high q values is $\beta = -4$, as for spherical particles embedded in a homogeneous material. This description is in agreement with the STM topography taken right after bulk Xe desorption for the analogue sample (Fig. 4.7 (a)). This value of β though could also be due to a fractal interface, with fractal dimension equal to 2. Further annealing provokes a change of the power law towards smaller values. Interestingly at 200K, after full Xe desorption, the same power law $\beta = -2$ is found for both samples, indication that the nano-cluster/Ag(111) interface is similar in the two cases. Therefore the system forgets about its own history, after Xe desorption, as also suggested by the STM investigation in Section 4.2.

4) Low values found for β and their variations during BLAG indicate that from the point of view of X-ray scattering, the Co nano-clusters cannot be considered as proper 3D structures and/or the interfaces present in the system have fractal properties. Due to tip convolution effects though the actual lateral shape of the clusters made by more then one atomic layer height is difficult to resolve by STM, and always appear spherical. In order to answer this question, more investigation is needed. In any case, for Au clusters made by Xe-BLAG with graphite as substrate, a fractal dimension between 1.42 and 1.72 was found [112], depending on the initial metal coverage. One can expect though that this is a value which is strongly dependent on the

substrate and deposited metal. This could be quite different in the case of Co clusters on Ag(111).

A second interpretation of the low values of β during BLAG can be done, based on the dimensional law (see Eq. 3.31). According to this law a value of $\beta = 2$ is found in case of a disc and of $\beta = 4$ in case of a sphere. The value of $\beta = 2$ found right after deposition of Co on Xe for both Xe thicknesses would indicate that Co nano-structures have a disc-like shape. In case of Co/thin Xe layer, the disc-like shape would remain over the full temperature range, meaning that also nano-clusters on Ag(111) are two-dimensional objects. On the other hand in case of Co/thick Xe layer, the process of Xe desorption above 55K gives $\beta = 4$ that points towards the formation of spherical nanoparticles. The 3D shape is maintained until the clusters make contact with the substrate for temperatures above 100K, when β starts to gradually decrease down to the value $\beta = 2$ found at room temperature. This could be a symptome of a progressive wetting of the surface by the nano-clusters, which is reflected in the high aspect ratio (diameter/height) found for the Co clusters on Ag(111) at room temperature, which is about 10 (see Section 4.2.2). Differences in the cluster morphology for the two systems at the temperature of 100K are also observed in STM topographies shown in Fig. 4.15: compact 3D clusters are observed for the Co/thick Xe system whereas only tiny clusters appears in case of Co/thin Xe, mainly absorbed on the surface step edges.

In conclusion the X-ray scattering experiments were able to show that in the limit of a single Xe ML on Ag(111) the BLAG is equivalent to a deposition of Co atoms on a very weakly interacting substrate. On the other hand from the measurements on the thick Xe buffer layer one could see that deposition of Co provokes a change in the Xe bulk structure, due to a weaker Xe-Xe interaction that finally affects the formation of Co nano-structures in the early stages of BLAG. The two growth modes are finally indistinguishable for temperatures above 150K, i.e. after complete Xe desorption, where the cluster shape and distribution only depends on the balance between surface wetting and thermal activated diffusion.

4.4 2D arrays of Co nano-clusters

In this last set of experiments the BLAG concept at low Xe coverage presented in the previous section has been exploited to 'fabricate' ordered arrays of Co nano-clusters on a pre-patterned substrate. Here the pre-patterned substrate with template functions is the mechanically stable boron-nitride nanomesh (BN). As shown for the Ag(111) and Pt(111) substrates in Sec-

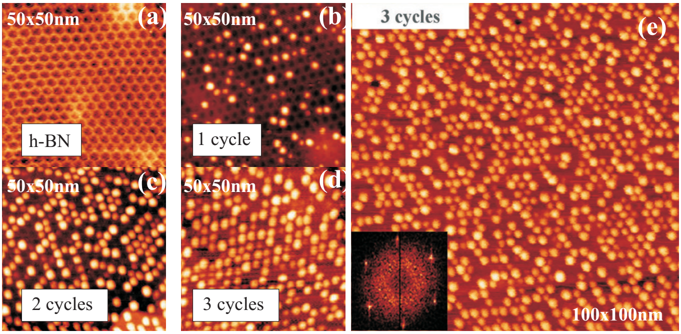

Figure 4.16: STM topographies: (a) The *h*-BN nanomesh (T = 4.2K); (b)-(e) the system after BLAG cycles of Co clusters (T = 300K)

tion 4.2 in fact, the metal-substrate interaction during BLAG strongly affects the cluster morphology. Here, it will be further shown that this interaction can be used to make mono-dispersed, highly ordered, and dense arrays of nano-clusters using the template effect.

Such ordered arrays of magnetic nano-structures have been further used to investigate the effect of well-directed hybridization of the Co clusters with other materials. The magnetism of Co arrays capped with non-magnetic (Au, Pt, Al_2O_3) and magnetic (Mn-Pt) materials was investigated. The aim was duplex: first to study the magnetic properties of the clusters on the nanomesh *per se* and their mutual interactions (direct dipolar or through the matrix atoms) and second to use the system for more basic physics studies of magnetic interactions between superparamagnets and unsaturated spins of an antiferromagnet, at the nano-cluster interface.

4.4.1 *h*-BN nanomesh as a template for Co nano-clusters

Co clusters are prepared *in-situ* on the BN by repeated cycles of buffer layer assisted growth. Due to the template effect of the BN, Co clusters of about 2nm in diameter occupy the pits of the corrugated surface, that correspond to the depressions in the Moiré structure formed by the BN on the Rh(111) surface (see Section 3.3.3). This leads to a dense arrangement of well-separated clusters (see Fig. 4.16). Clusters of $1-3$ nm in diameter are achieved by using approximately 2 monolayers of Xe and 3-5% of a full monolayer of Co. With the deposition parameters Cobalt = 0.05ML and Xenon =5L, about 30% of the depressions in the BN layer are filled by one BLAG cycle, as shown in the

STM image in Fig. 4.16 (b). The number of the clusters deposited per area can be controlled, to some extent, by varying experimental parameters but depression occupancies beyond 40% are difficult to achieve in a single BLAG cycle. In order to fabricate ordered cluster layers with BN layer occupations approaching the ideal value of 100% (full occupancy), the BLAG cycles were repeated several times. The fraction of occupied depressions gradually increases, and after three subsequent BLAG cycles approximately 70% of the depressions are occupied (Fig. 4.16 (d)-(e)). Larger amounts of Co per cycle help in filling the BN layer more quickly. However, more Co per cycle results also in larger clusters, and one observes that the presence of larger clusters impedes their ordered arrangement. This might be due to a decreased mobility of the clusters with increased volume, or simply a geometrical on-site repulsion problem if the clusters diameters exceed the distance between the centers of neighboring depressions on the BN layer. This behavior could be modeled by Monte Carlo simulations of the deposition process [148]. The model shows that the approach to full coverage is critically slowed down by attractive interparticle interactions, which result in the coalescence and growth of some of the clusters.

The present structure has several specific advantages. First, the clusters center-to-center distance of order of 3 nm is ideal for application as patterned media for ultrahigh density magnetic data storage (with a cluster density of $80 \cdot 10^{12}$ clusters per square inch, one cluster per bit and 100% filling would correspond to a storage density of about 80 Terabit/inch^2. This is 400 times larger than up-to-date densities of 345 Gigabits /inch^2, e.g. by Hitachi 2006). Second, the structures have a high periodicity necessary for a reliable read-and-write process. Some degree of aperiodicity can be accounted for by multiple-pass reading and writing. Third, the mesh is suitable for robust annealing at high temperatures, which is an important practical consideration for e.g. high-coercivity FePt based recording media. Forth, tunneling spectroscopy studies revealed a Coulomb gap of 160 meV in the electronic structure of the Co clusters on the BN layer, proving their electronic decoupling from the Rhodium substrate [80]. BN layers thus turn out to be also an ideal playground for the study of the electronic interaction of nano-structures with the substrate.

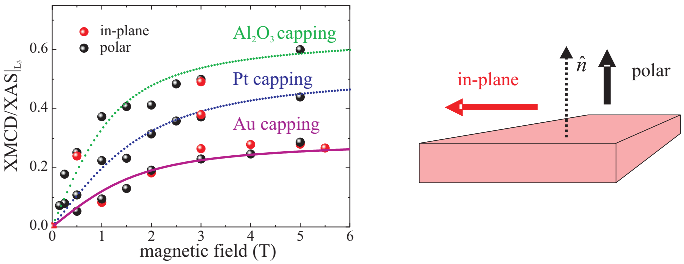

Figure 4.17: XMCD/XAS ratio at the L_3 Co edge versus magnetic field intensity for the Co clusters system capped with Au, Pt and Al_2O_3.

4.4.2 Magnetic properties of capped Co nano-cluster arrays

Non-magnetic capping

In Fig. 4.17 a plot of the XMCD/XAS asymmetry at the L_3 edge of Co versus magnetic field is shown for the samples capped with non-magnetic materials Au, Pt and Al_2O_3. The amount of Co for the three samples was about $0.15 - 0.2$ML. From the XAS spectra a check for the eventual contamination of the sample after exposure to air could be done. The sample capped with Pt was partially oxidized, possibly due an insufficient thickness of the capping layer. The partial oxidization is visible in the spectral shape of the XAS at the Co L_3 edge, showing typical features of a mixture between Co and CoO. The other two samples instead showed a pure Co spectral shape.

In all the three cases highest available magnetic field of 5 Tesla were sufficient to saturate the Co magnetization. The XMCD/XAS value at saturation for the three samples differ: the highest value is found for Al_2O_3 capping, with an XMCD/XAS value at the L_3 edge of about 60% at saturation. This value is in line with other experimental data for Al_2O_3 capped Co clusters [149]. The sample capped with Pt has a slightly smaller value, about 45%, which can be explained by contamination, in agreement with what was reported in Ref. [150]. Finally, for the sample capped with Au, the moment is strongly reduced, leading to a value of only 30%.

The orbital moment in the three samples can be compared, by normalizing the XMCD signal at the L_2 edge to one. According to Eq. 3.38, the orbital moment in fact is proportional to the integral of the XMCD spectrum across the $L_{3,2}$ edges, that is the difference between the areas at the L_3 and at the L_2 edges (see Fig. 3.12). Therefore, for the same area at the L_2 edge, a larger area at the L_3 edge simply implies a larger difference between the two areas, that is a larger orbital moment.

After making the normalization (not shown) one could observe that the sample capped with Pt has the highest orbital moment. An enhancement of the orbital moment with respect to the spin moments due to oxidization of Co clusters was reported again by Ref. [150].

Magnetic measurements have been performed for two different orientations of the magnetic field with respect to the sample, in-plane and polar. A common feature to all three samples is the absence of magnetic remanence (no finite XMCD/XAS at zero magnetic field) in all measured directions. This is in line with the isotropic behavior of the magnetization that has, within the experimental error, the same value in the two direction parallel and perpendicular to the sample normal. The Co clusters therefore must have a blocking temperature below the measurement temperature of $T = 15\text{K}$.

MnPt capping

Exchange bias can appear e.g. when a magnetic $3d$ metal like Cobalt is brought in contact with an antiferromagnetic material. The effect becomes manifest in a horizontal shift of the hysteresis curves by a characteristic field H_b called exchange bias field. For a topical review see Ref. [151].

Exchange bias has been known for many years, yet the microscopic origin is still under debate and has seen the development of a large number of theories. One of these theories is the domain state model (DS, [152]), in which the exchange bias-field H_b is correlated with the bulk magnetic state of the antiferromagnet (AFM) rather than with interface disorder. Accordingly to this interpretation the interface magnetization responsible for H_b is proportional to the uncompensated bulk magnetization. Recent SQUID measurements in Ref. [153] showed that the presence of the exchange bias effect for isolated Co nano-clusters immersed in a bulk MnPt matrix could be explained by the DS model. The authors stress the fact that with SQUID only the bulk MnPt magnetization is available, which they compare with Co/MnPt samples.

The aim of the present measurements is to examine the system of Co cluster in contact with MnPt in reduced dimensions. Varying the amount of MnPt allows to extract information of Mn atoms at the Co interface, crucial for exchange bias. The key of these measurements is the element selective XMCD technique, which in contrast to the SQUID technique used in [153] enables the magnetic characterization of Co and Mn individually.

A MnPt wedge was deposited at low temperature (about 50K) in order to impede thermal diffusion of the atoms impinging the substrate (see Fig. 4.18). The low temperature deposition should in fact lead to formation of

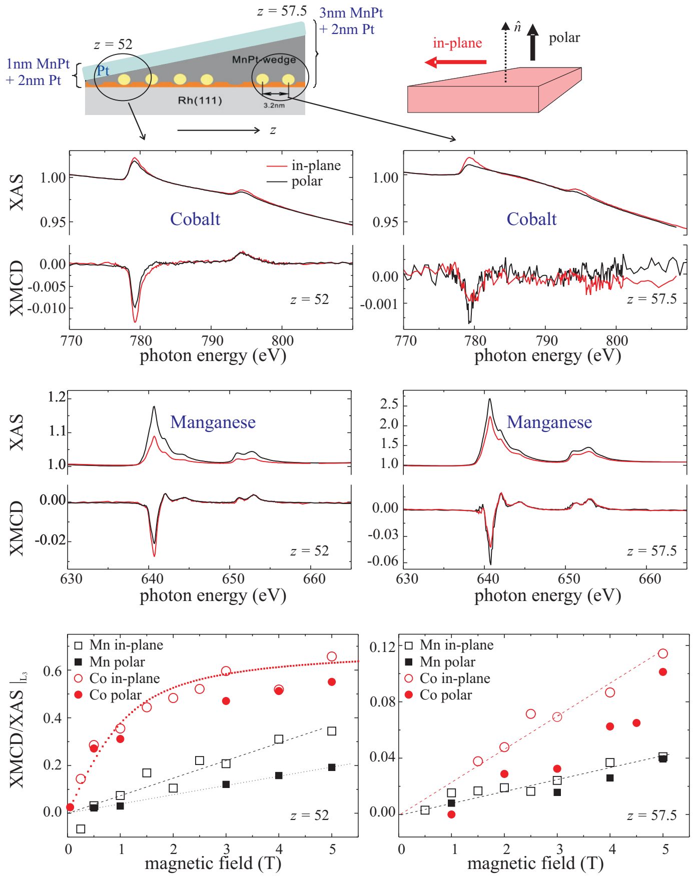

Figure 4.18: XAS and XMCD measurements of Co clusters capped with a MnPt wedge. The XAS signal was recorded at the $L_{3,2}$ Co and Mn absorption edges for different positions along the wedge, and the plots here are shown for the two extreme positions with 1nm (left column) and 3nm (right column) of MnPt capping. In the lowest row the XMCD/XAS ratio at the L_3 recorded versus applied magnetic field intensity is plotted in the two positions along the wedge, for both Co and Mn.

disordered layers made out of small ordered grains. XAS and XMCD spectra are shown in Fig. 4.18, at the two extreme positions along the wedge with MnPt thicknesses $t_{\mathrm{MnPt}} = 1\mathrm{nm}$ and 3nm, respectively. Magnetization curves were also measured at the Mn and Co lines along the wedge, by recording the XMCD/XAS at the L_3 edge versus applied magnetic field. The results are shown in the lowest panel of Fig. 4.18, for the same MnPt thicknesses. The following main results are found:

- Thin MnPt capping $(0.5 - 1\mathrm{nm})$: the Co magnetization is saturated (very similar to what is seen for non-magnetic capping Pt; there is a slight in-plane anisotropy; the Mn magnetization is not saturated and shows in-plane anisotropy.
- Thicker MnPt capping (about 3nm): the Co magnetization is not-saturated and therefore strongly reduced, about 5 times less as compared to the value found at thin MnPt capping with the same value of the magnetic field; Co shows possibly still in-plane anisotropy but the signal/noise ratio is too poor for a definitive conclusion; the Mn magnetization is still unsaturated but also reduced (about 8 times compared to thin capping in the in-plane direction) and there is no anisotropy.
- In both cases no remanence and no exchange bias is observed.

It is safe to state that for small thicknesses of MnPt the ratio R of Mn atoms bound in the MnPt phase and Mn atoms at the interface to Co is decreased. Therefore in the thin part of the wedge one is predominantly sensing the Mn interface atoms (hereafter called Mn-I). On the other hand, for higher values of the MnPt thickness, R is higher and consequently the measured XMCD reflects more the magnetization of the Mn within the bulk MnPt phase (hereafter called Mn-II). Therefore from the data in Fig. 4.18 one can say that the unsaturated Mn magnetization at the interface is much higher then in bulk. This makes sense if one considers that stable antiferromagnetism develops with increasing MnPt thickness. The more MnPt, the more degree of AF coupling in the system, just because the AF is a bulk property. It seems that, in correspondence with the development of a bulk AF-state, a quenching of the magnetization of the Co clusters occurs, somehow totally unexpected. Summarizing the observations one gets:

Mn-I. At the thin part of the MnPt wedge, most likely the clusters are surface covered (fully or partially) with MnPt atoms and the Co is not really affected by that. The magnetic properties of the sample are very similar to the case of non-magnetic capping. The Mn atoms have an unsaturated magnetization that shoes an in-plane easy axis.

Mn-II. With increasing MnPt thickness (not shown here are intermediate points along the wedge) the XMCD/XAS of the Mn decreases dramatically, up to a factor of almost 10 in the in-plane direction. This is a sign for the onset of the bulk AF ordering, that leads to a smaller value of the uncompensated magnetization. These Mn atoms show no preferential direction of the magnetization. At the same time, the magnetization of the Co clusters is strongly reduced, and saturation at fields of 5T is incomplete. Especially in the polar direction the Co magnetization seems to suffer the MnPt interaction more strongly, being below the value found in the in-plane direction until 5T.

4.4.3 Discussion and open questions

First, a few words have to be spent on the absence of magnetic anisotropy for the samples capped with non-magnetic material, starting by a simpler case: a thin Co film capped with a metal. Capping leads to hybridization of the *d* orbitals of the Co with the *d* orbitals of the metal at the interface. If the coupling between the two metal is larger in the vertical direction, the effect of the hybridization is an enhancement of the orbital moment in the direction perpendicular to the interface and therefore generates magnetic anisotropy (see Section 2.1). The effect is maximized for the capping material that has the smallest difference with the energies of unoccupied *d*-orbitals of Co, since this leads to a stronger bond. This is the case for example for a Au on a Co monolayer, where an out-of-plane magnetic anisotropy is expected. The ingredients for an observable magnetic anisotropy are therefore a strong interaction accompanied by a well defined directionality of the bond.

In the case of Co clusters on the *h*-BN a very weak electronic coupling of the clusters with the substrate occurs and furthermore the interface between capping layer and Co does not define a specific direction as in the case of a thin film: for atoms on the cluster apex the magnetic moment might be the highest along the normal to the surface, but for an atom on the side the interface normal would be in the in-plane direction. Therefore every atom at the surface has an easy axis in a different direction, and in average there is no anisotropy.

Second, in the magnetization values (proportional to the ratio XMCD/XAS at the L_3) one can see a clear trend where maximum M is found for Al_2O_3-capped Co clusters, slightly lower values for Pt-capped Co-CoO clusters and finally Au-capped clusters with a value of M that is half of the value found for Al_2O_3. This trend reflects the chemical interaction between Co atoms and atoms of the capping layer at the cluster surface, and therefore the different degree of hybridization with the Co *d* band. The effect is the highest for Au,

which is reasonable due to the above mentioned vicinity of the *d* levels of Co and Au atoms.
This discussion will need to be confirmed by band-structure calculations, that would be simplified due to the high level of ordering of the system as compared to granular alloys or clusters embedded in a matrix.

Third, concerning the very strong quenching effect of the average magnetization values observed in MnPt-capped clusters the situation is more complex and a final explanation was not possible so far. However, possible scenarios are given below.

- RKKY interaction between clusters mediated by the MnPt matrix that can lead to antiferromagnetic coupling between clusters. This argument was used to explain the quenching of moments in Co clusters capped with Cu [154] and is supported by calculations. If this is the case, the occurring of quenching only at higher MnPt coverages must be related to an incomplete interconnection of the clusters through the MnPt matrix at low coverages of 1nm. That means, even if the clusters are capped, there might still be some empty spaces between them. This, however, should not be the case since the Co clusters are composed by about 50 atoms (as inferred by careful analysis of STM images that also takes into account tip convolution effects) and with an apparent height of about 1ML, that is about 2 Å.

- 'Chemical' effect: as discussed in case of non-magnetic capping, the Co atoms at the cluster surface, bonded to Mn atoms, might have a lower spin moment due to hybridization effects and/or formation of a frustrated spin phase or a spin glass. The average magnetism is therefore reduced. In the same direction is the possibility of the formation of a Co-Mn alloy, even though the low MnPt deposition temperature of $T = 50$K makes it unlikely. A deeper investigation of the lineshape of the Mn XAS and XMCD spectra will be helpful to understand what is the chemical state of Mn. However, this would not explain why, at low MnPt coverage, both Co and Mn are found to have a higher magnetization.

- Effect of the DS magnetization: the interaction between Co clusters and the MnPt matrix at the cluster interface is dominated by the MnPt bulk magnetization. Since the MnPt system at thick capping layers does not exhibit magnetic anisotropy, and also no blocking, the effect of the DS is to quench the Co moments at the cluster surface instead of the formation of exchange bias as seen by Morel *et. al.* [153]. In this case, the dependence of the Co magnetization on the MnPt thickness

> would be explained with the appearance of the DS for large enough MnPt thicknesses. Furthermore, it would be an indication that the Mn-II atoms are those responsible for triggering the magnetization of the Co atoms, and not those at the interface with the clusters.

In conclusion 2D arrays of nano-clusters on the *h*-BN are not the ideal system for magnetic storage devices due to the lack of remanence, but they revealed to be a very suitable system to study very basic physical phenomena of nanomagnetism like the famous exchange bias effect.

Chapter 5

Conclusions and outlook

In this thesis experiments on $3d$ and $4d$ metal nano-structures grown by buffer layer assisted growth (BLAG) have been presented. The work was focused on understanding and exploiting the interactions between the deposited metal and the underlying substrate, with the following aims (i) to clarify the growth mechanism of nano-structures during BLAG; (ii) to use the BLAG to fabricate ordered arrays of nano-structures and (iii) to study coordination effects in magnetic materials.

In Section 4.1 finite intrinsic magnetic moments have been measured for Rh nano-structures in contact with an inert, non-magnetic Xenon surface using X-ray magnetic circular dichroism. The characteristic multi-step procedure of Xenon BLAG is exploited to study the magnetism of Rh submonolayer coverages between two extreme limits, from quasifree few-atom sized clusters on a non-interacting buffer layer towards Rh nano-structures in contact with a weakly-interacting Ag(100) substrate. Size and hybridization effects affecting the Rh orbital and spin moments become visible when the average Rh-Rh coordination is changed. Non-vanishing magnetic moments as large as $0.17\mu_\mathrm{B}$ per hole appear for Rh atoms situated on a Xenon buffer layer, which decay as a function of increasing Rh-Rh coordination. When the Rh clusters are brought in contact with the Ag(100) surface the moments become entirely quenched. This behavior is ascribed to the formation of large clusters upon Xenon desorption. The analysis of the Rh experimental XAS lineshape and its comparison with *ab-initio* simulated spectra for differently coordinated Rh atoms allowed to understand the absence of magnetism in Rh impurities directly deposited on Ag(100), that most likely is due to formation of a Ag-Rh alloy.

In Section 4.2 a detailed investigation of the mechanisms driving the dynamics during BLAG has been presented, focusing on the early stage of cluster formation. Variable temperature scanning tunneling microscopy (VT-

STM) for the first time enables the direct observation of cluster-substrate interactions that lead to different growth mechanisms of Cobalt/Xenon in case of adsorption on two electronically very different metal substrates: Ag(111) and Pt(111). The key result is that for thin Xenon buffer layers the cluster formation is ruled by the interaction with the metal substrate underneath, which in the case of Pt(111) leads to a penetration of the Cobalt into the Xenon buffer layer long before the buffer layer is desorbed. This effect is favored by the high value of Xe-Xe repulsion for the Xe/Pt(111) system. The observations are backed by X-ray magnetic circular dichroism measurements which allowed to independently estimate cluster size and to address the question at what stage during BLAG the clusters make contact with the metal substrate. No magnetic anisotropy is measured before Xenon desorption for the Cobalt/Xenon/Ag(111). Opposite to that, an out-of-plane magnetic anisotropy emerges for the case of Pt(111) already before Xenon desorption, a clear signature for a direct magnetic interaction between surface and clusters. By application of the XMCD sum-rules the magnetic moments and the magnetic anisotropy during the different stages of BLAG have been calculated. The largest values for the moments are obtained for Co clusters on the thick Xenon layers, while during desorption a decrease is observed. The effect is explained by the reduced average coordination of small Co atoms as well as the absence of hybridization with the substrate, showing that classic BLAG works in the thick buffer layer limit. In the case of Co clusters supported on Ag(111) values of the spin moment lower than bulk Co have been found, and the result is discussed in terms of possible substrate mediated effects such as RKKY and Dzyaloshinski-Moriya (DM) anisotropic exchange interaction.

From *ab-initio* DFT calculations it is evident that magnetic properties like the moments but especially the appearance of magnetic anisotropy is largely determined by cluster-substrate interface effects. X-ray surface diffraction and scattering measurements presented in Section 4.3 revealed to be extremely helpful to investigate the BLAG process. The experiments give complementary information to the VT-STM and XMCD measurements, especially on the dynamics happening during Co deposition onto Xenon layers, which are not accessible by VT-STM. The data allow to draw a growth model where the Co deposited on the Xenon buffer is coated by the Xenon atoms, in case of thick Xe buffer and prove that the growth of Co on a thick Xe layer and on a single Xe layer in the early stages of BLAG exhibit fundamentally different behaviors.

In Section 4.4 the effect of the interaction between substrate and deposited metal during BLAG has been exploited to form ordered arrays of Co nanoclusters. Using a *h*-BN nanomesh as a substrate with very thin Xenon buffer

layers a template effect for the clusters is obtained. The resulting cluster array system shows a very high degree of order, with well separated nanoclusters corresponding to the hexagonal symmetry of the nanomesh pits.
This system has been used to investigate basic magnetic properties of Co clusters in contact with non-magnetic and magnetic capping materials. The advantage over the granular structures or clusters embedded in matrix investigated so far is the full control over cluster size and inter-cluster distance. The latter is given by the template periodicity of 3.2 nm, that allows for a much better modeling.

The results achieved in this thesis opened new scientific paths that could be followed in the near future. One idea is to use the BLAG technique in order to form 2D arrays of binary clusters, made out of a $3d$ and a $4d$ or $5d$ element. In these compounds the high value of the $3d$ metal magnetization joined together with the high spin-orbit constant of the $4d$ and $5d$ elements can lead to a high stability of the magnetization. For example for the Co-Pt alloys in the bulk-ordered $L1_0$ phase a value of the magnetic anisotropy as high as 0.8meV/Co atom was found [155], while the bulk value of hcp Co is only 0.045meV/atom. In a nano-structure these numbers are expected to be even larger, due to the increase of the orbital moment (see Section 2.1). Despite the fact that many groups are already studying these systems, a certain difficulty is usually found to achieve control over the structures. The problem is that as-grown Co-Pt particles or films are usually chemically disordered, and hence have only low anisotropy values. The required $L1_0$ phase can only be achieved after thermally annealing the substrate to 600°C [156], a temperature at which alloying with the substrate can occur for metal supported clusters. Using the very low reactivity of the nanomesh and its robustness up to high temperatures might be a good strategy.

Nano-cluster on the h-BN are a very interesting system also from a fundamental point of view. The electronic coupling between the h-BN monolayers and transition-metal surfaces has been studied by *ab-initio* density functional theory (DFT) calculations in Ref. [157], showing that in the presence of magnetic $3d$ atoms such as Co or Ni also the p_z states of the h-BN are spin-splitted in up and down bands. This is quite interesting in view of a system where the h-BN is intercalated between two different metals, one being a ferromagnet and the other one a non-ferromagnet, however, with a high susceptibility, such as Pt or Rh. In this case, the non-magnetic element is supposed to become polarized because of the interaction via the h-BN states, polarized by the ferromagnet. This might lead to new, interesting properties such as well-defined and high magnetic anisotropies. Such aspects might be investigated by spectroscopy measurements such as XAS, to probe directly the electronic coupling between the two metals and the h-BN layer but also indirectly by electronic transport measurements in Hall configurations which are sensitive to magnetic properties of the material.

Finally, one would like to use different templates for the nano-clusters, where a stronger interaction with the material template leads to magnetic anisotropy and therefore stabilization of the magnetization. One candidate is the system graphene on Ru(0001) [158], which has the advantage to be easy to prepare, simply by annealing the substrate at high temperatures under ethane partial pressure. Graphene/Ru(0001) is a corrugated single-layer with strongly bound and weakly bound regions, that makes it a good template for adsorbates very similar to *h*-BN/Rh(111). Furthermore, graphene/Ru(0001) shows a metallic behavior with a Fermi surface [158], that makes it especially appealing for electronic coupling of small $3d$ clusters. This might lead to increased magnetic anisotropies and therefore higher blocking temperatures.

Bibliography

[1] G. D. Waddill, I. M. Vitomirov, C. M. Aldao, S. G. Anderson, C. Capasso, J. H. Weaver, and Z. Liliental-Weber, Phys. Rev. B **41**, 5293 (1990).

[2] J. Weaver and G. Waddill, Science **251**, 1444 (1991).

[3] T. R. Ohno, J. C. Patrin, U. S. Ayyala, and J. C. Weaver, Phys. Rev. B **44**, 1891 (1991).

[4] I. G. Marchenko and I. M. Neklyudov, Low Temp. Phys. **32**, 957 (2006).

[5] J. Honolka, K. Kuhnke, L. Vitali, A. Enders, S. Gardonio, C. Carbone, S. Krishnakumar, K. Kern, P. Bencok, S. Stepanow, and P. Gambardella, Phys. Rev. B **76**, 144412 (2007).

[6] E. C. Stoner, Proc. R. Soc. Lond. **A165**, 372 (1938).

[7] D. M. Cox, D. J. Trevor, R. L. Whetten, E. A. Rohlfing, and A. Kaldor, Phys. Rev. B **32**, 7290 (1985).

[8] W. A. de Heer, P. Milani, and A. Chtelain, Phys. Rev. Lett. **65**, 488 (1990).

[9] J. P. Bucher, D. C. Douglass, and L. A. Bloomfield, Phys. Rev. Lett. **66**, 3052 (1991).

[10] I. M. L. Billas, A. Châtelain, and W. A. de Heer, J. Magn. Magn. Materials **168**, 64 (1997).

[11] E. C. Stoner, Proc. R. Soc. Lond. **A154**, 656 (1936).

[12] S. Blügel and G. Bihlmayer, In *Handbook of Magnetism and Advanced Materials*, edited by H. Kronmüller and S. Parkin (J. Wiley & Sons, 2007), p. Magnetism of Low Dimensions: Theory.

[13] A. J. Cox, J. G. Louderback, and L. A. Bloomfield, Phys. Rev. Lett. **71**, 923 (1993).

[14] A. J. Cox, J. G. Louderback, S. E. Apsel, and L. A. Bloomfield, Phys. Rev. B **49**, 12295 (1994).

[15] M. Getzlaff, *Fundamentals of Magnetism* (Springer, 2007).

[16] S. Kaya, Sci. Reports Tohoku Univ. **17**, 639 (1928).

[17] P. Gambardella, S. Rusponi, M. Veronese, S. S. Dhesi, C. Grazioli, A. Dellmeyer, I. Cabria, R. Zeller, P. H. Dederichs, K. Kern, C. Carbone, and H. Brune, Science **300**, 1130 (2003).

[18] J. Stöhr, J. Magn. Magn. Materials **200**, 470 (1999).

[19] G. van der Laan, J. Phys.: Condens. Matter **10**, 3239 (1998).

[20] P. Bruno, Phys. Rev. B **39**, 865 (1989).

[21] P. Krams, F. Lauks, R. L. Stamps, B. Hillebrands, and G. Güntherodt, Phys. Rev. Lett. **69**, 3674 (1992).

[22] C. Chappert, H. Bernas, V. K. J. Ferr, J.-P. Jamet, Y. Chen, E. Cambril, T. Devolder, F. Rousseaux, V. Mathet, and H. Launois, Science **280**, 1919 (1998).

[23] H.-J. Elmers, J. Hauschild, and U. Gradmann, Phys. Rev. B **54**, 15224 (1996).

[24] M. Bode, O. Pietzsch, A. Kubetzka, and R. Wiesendanger, Phys. Rev. Lett. **92**, 067201 (2004).

[25] J. Prokop, A. Kukunin, and H. J. Elmers, Phys. Rev. Lett. **95**, 187202 (2005).

[26] G. Bihlmayer, *Magnetism goes Nano; Reduced Dimensions: Magnetic Anisotropy.* 36th IFF Spring School, Jülich (2005).

[27] S. Blundell, *Magnetism in Condensed Matter* (Oxford University Press, 2001).

[28] D. Gatteschi and R. Sessoli, Angew. Chem. Int. Ed. **42**, 268 (2003).

[29] B. Hayes, Am. Sci. **90**, 212 (2002).

[30] S. D. Bader, Rev. Mod. Phys. **78** (2006).

[31] D. Weller and T. McDaniel, *Advanced Magnetic Nanostructures* (Springer, Berlin, 2006), pp. 295–324.

[32] C.-B. Rong, N. Poudya, G. S. Chaubey, V. Nandwana, R. Skomski, Y. Q. Wu, M. J. Kramer, and J. P. Liu, J. Appl. Phys. **102**, 043913 (2007).

[33] G. Binnig, H. Rohrer, C. Gerber, and E. Weibel, Appl. Phys. Lett. **40**, 178 (1982).

[34] C. J. Chen, *Introduction to Scanning Tunneling Microscopy* (Oxford Science Publications, 2008), 2nd edition.

[35] J. Bardeen, Phys. Rev. Lett. **6**, 57 (1960).

[36] J. Tersoff and D. R. Hamann, Phys. Rev. Lett. **50**, 1998 (1983).

[37] J. Tersoff and D. R. Hamann, Phys. Rev. B **31**, 805 (1985).

[38] C. J. Chen, Phys. Rev. Lett. **65**, 448 (1990).

[39] J. Tersoff, M. J. Cardillo, and D. R. Hamann, Phys. Rev. B **32**, 5044 (1985).

[40] C. J. Chen, Phys. Rev. Lett. **69**, 1656 (1992).

[41] J. V. Barth, H. Brune, G. Ertl, and R. J. Behm, Phys. Rev. B **42**, 9307 (1990).

[42] S. Park and C. F. Quate, Rev. Sci. Instrum. **58**, 2004 (1987).

[43] K. Nagaya and H. Kojima, J. Dynam. Syst. Meas. Control. **106**, 52 (1984).

[44] D. Peterka, A. Enders, G. Haas, and K. Kern, Rev. Sci. Instrum. **74**, 2744 (2003).

[45] D. Peterka. Ph.D. thesis, École Politechnique Fédérale de Lausanne (2002).

[46] D. Repetto. Ph.D. thesis, École Politechnique Fédérale de Lausanne (2006).

[47] F. Meier, K. von Bergmann, P. Ferriani, J. Wiebe, M. Bode, K. Hashimoto, S. Heinze, and R. Wiesendanger, Physical Review B (Condensed Matter and Materials Physics) **74**, 195411 (2006).

[48] E. Lundgren, B. Stanka, M. Schmid, and P. Varga, Phys. Rev. B **62**, 2843 (2000).

[49] K. Besocke, Surf. Sci. **181**, 145 (1987).

[50] B. C. Stipe, M. A. Razaei, and W. Ho, Rev. Sci. Instrum. **70**, 137 (1999).

[51] B. L. Henke, E. M. Gullikson, and J. C. Davis, Atom. Data and Nucl. Data Tables **54**, 181 (1993).

[52] R. Feidenhans', Surf. Sci. Reports **10**, 105 (1989).

[53] B. E. Warren, *X-Ray Diffraction* (Addison-Wesley, Reading, MA, 1969).

[54] R. W. James, *The Optical Principles of the Diffraction of X-Rays* (Ox Bow Press, Connecticut, 1982).

[55] M. Born and E. Wolf, *Principles of Optics* (Pergamon, Oxford, 1975), chapter 1.6.

[56] L. Nevot and P.Croce, Phys. Appl. **15**, 761 (1980).

[57] H. Kiessig, Ann. Phys. **10**, 715 (1931).

[58] H. Kiessig, Ann. Phys. **10**, 769 (1931).

[59] U. Pietsch, V. Holy, and T. Baumbach, *High resolution X-ray scattering* (Springer, New York, 2004), second edition.

[60] S. K. S. Sinarota, E. B. Garrot, and S. Stanley, Phys. Rev. B **38**, 2297 (1988).

[61] M. V. R. Murty, T. Curcic, A. Judy, B. H. Cooper, A. R. Voll, J. D. Brock, S. Kycia, and R. L. Headrick, Phys. Rev. B. **60**, 16956 (1999).

[62] G. Renaud, R. Lazzari, C. Revenant, A. Barbier, M. Noblet, O. Ulrich, F. Leroy, J. Jupille, Y. Borensztein, C. R. Henry, J.-P. Deville, F. Scheurer, J. Mane-Mane, and O. Fruchart, Science **300**, 1416 (2003).

[63] D.-M. Smilgies, P. Busch, C. M. Papadakis, and D. Posselt, Synchr. Rad. News **15**, 35 (2002).

[64] M. Blume., J. Appl. Phys. **57**, 3615 (1985).

[65] F. de Groot and A. Kotani, *Core Level Spectroscopy of Solids* (CRC Press, 2008).

[66] F. M. F. de Groot, J. C. Fuggle, B. T. Thole, and G. A. Sawatzky, Phys. Rev. B **42**, 5459 (1990).

[67] H. Ebert, Rep. Prog. Phys. **59**, 1665 (1996).

[68] C. T. Chen, Y. U. Idzerda, H.-J. Lin, N. V. Smith, G. Meigs, E. Chaban, G. H. Ho, E. Pellegrin, F., and Sette, Phys. Rev. Lett. **75**, 152 (1995).

[69] J. Stöhr and Y. Wu., In *X-ray Magnetic Circular Dichroism: Basic Concepts and Theory for 3d Transition Metal Atoms*, edited by A. S. Schlachter and F. J. Wuilleumier (Kluwer Academic Publishers, 1994), volume 254 of *NATO ASI Series E: Applied Sciences*, p. 221.

[70] P. Carra, B. T. Thole, M. Altarelli, and X. Wang, Phys. Rev. Lett. **70**, 694 (1993).

[71] B. T. Thole, P. Carra, , F. Sette, and G. van der Laan, Phys. Rev. Lett. **68**, 1943 (1992).

[72] J. Stöhr, *X-Ray Absorption: Principles, Applications, Techniques of EXAFS, SEXAFS and XANES* (Wiley, New York, 1988), p. 443.

[73] M. O. Krause, J. Phys. Chem. Ref. Data **8**, 307 (1979).

[74] R. Nakajima, J. Stöhr, and Y. U. Idzerda, Phys. Rev. B **59**, 6421 (1999).

[75] W. L. O'Brien and B. P. Tonner, Phys. Rev. B **50**, 12672 (1994).

[76] R. Nakajima, J. Stöhr, and Y. U. Idzerda, Phys. Rev. B **59**, 6421 (1999).

[77] R. Paniago, R. Matzdorf, G. Meister, and A. Goldmann, Surf. Sci. **325**, 336 (1995).

[78] M. Corso, W. Auwarter, M. Muntwiler, A. Tamai, T. Greber, and J. Osterwalder, Science **303**, 217 (2004).

[79] S. Berner, M. Corso, R. Widmer, O. Groening, R. Laskowski, P.Blaha, K. Schwarz, A. Goriachko, H. Over, S. Gsell, M.Schreck, H. Sachdev, T. Greber, and J. Osterwalder, Angew. Chem. Int. Ed. **46**, 5115 (2007).

[80] I. Brihuega, C. H. Michaelis, J. Zhang, S. Bose, V. Sessi, J. Honolka, M. A. Schneider, A. Enders, and K. Kern, Surf. Sci. **602**, L95 (2008).

[81] R. Laskowski, P. Blaha, T. Gallauner, and K. Schwarz, Phys. Rev. Lett. **98**, 106802 (2007).

[82] P. Lang, V. Stepanyuk, K. Wildberger, R. Zeller, and P. Dederichs, Sol. Stat. Comm. **92**, 755 (1994).

[83] K. Wildberger, V. S. Stepanyuk, P. Lang, R. Zeller, and P. H. Dederichs, Phys. Rev. Lett. **75**, 509 (1995).

[84] V. S. Stepanyuk, W. Hergert, P. Rennert, K. Wildberger, R. Zeller, and P. H. Dederichs, Phys. Rev. B **59**, 1681 (1999).

[85] I. Cabria, B. Nonas, R. Zeller, and P. H. Dederichs, Phys. Rev. B **65**, 054414 (2002).

[86] D. Bazhanov, W. Hergert, V. S. Stepanyuk, A. A. Katsnelson, P. Rennert, K. Kokko, and C. Demangeat, Phys. Rev. B **62**, 6415 (2000).

[87] V. Bellini, N. Papanikolaou, R. Zeller, and P. H. Dederichs, Phys. Rev. B **64**, 094403 (2001).

[88] O. Eriksson, R. C. Albers, and A. M. Boring, Phys. Rev. Lett. **66**, 1350 (1991).

[89] M. J. Zhu, D. M. Bylander, and L. Kleinman, Phys. Rev. B **43**, 4007 (1991).

[90] R. Wu and A. J. Freeman, Phys. Rev. B **45**, 7222 (1992).

[91] S. Blügel, Phys. Rev. Lett. **68**, 851 (1992).

[92] S. Blügel, Phys. Rev. B **51**, 2025 (1995).

[93] I. Turek, J. Kudrnovský, M. Šob, and P. W. V. Drchal, Phys. Rev. Lett. **74**, 2551 (1995).

[94] G. A. Mulhollan, R. L. Fink, and J. L. Erskine, Phys. Rev. B **44**, 2393 (1991).

[95] C. Liu and S. D. Bader, Phys. Rev. B **44**, 12062 (1991).

[96] I. Chado, F. Scheurer, and J. P. Bucher, Phys. Rev. B **64**, 094410 (2001).

[97] S. Blügel, Phys. Rev. B **51**, 2025 (1995).

[98] T. K. Sham, Phys. Rev. B **31**, 1888 (1985).

[99] R. J. Behm, C. R. Brundle, and K. Wandelt, J. Chem. Phys. **85**, 1061 (1986).

[100] M. Tomaz, T. Lin, G. R. Harp, E. Hallin, T. K. Sham, and W. L. O'Brien, J. Vac. Sci. Technol. A **16**, 1359 (1998).

[101] M. Munoz-Navia, J. Dorantes-Davila, D. Zitoun, C. Amiens, B. Chaudret, M.-J. Casanove, P. Lecante, N. Jaouen, A. Rogalev, M. Respaud, and G. M. Pastor, Faraday Discuss. **138**, 181 (2008).

[102] A. Smekhova, D. Ciuculescu, P. Lecante, F. Wilhelm, C. Amiens, and B. C. B. Rogalev, IEEE Trans. Magn. **44**, 2776 (2008).

[103] R. Guirardo-López, P. Villaseñor-Gonzáles, J. Dorantes-Dávila, and G. M. Pastor, Eur. Phys. J. D **24**, 73 (2003).

[104] P. Villaseñor-González, J. Dorantes-Dávila, H. Dreyssé, and G. M. Pastor, Phys. Rev. B **55**, 15084 (1997).

[105] F. Aguilera-Granja, J. M. Montejano-Carrizalez, and R. A. Guirado-López, Phys. Rev. B **73**, 115422 (2006).

[106] Y.-V. Bae, H. Osanai, V. Kumar, and Y. Kawazoe, Phys. Rev. B **70**, 195413 (2004).

[107] J. S. Palmer, P. Swaminathan, S. Babar, and J. H. Weaver, Phys. Rev. B **77**, 195422 (2008).

[108] T. K. Sham, Phys. Rev. B **31**, 1903 (1985).

[109] L. S. Perkins and A. E. DePristo, Surf. Sci. **319**, 225 (1994).

[110] S.-P. Kim, S.-C. Lee, K.-R. Lee, and Y.-C. Chung, Acta Materialia **56**, 1011 (2008).

[111] S.-G. Lee and Y.-C. Chung, J. Appl. Phys. **105**, 034902 (2009).

[112] C. Haley and J. H. Weaver, Surf. Sci. **518**, 243 (2002).

[113] M. A. Chesters, M. Hussain, and J. Pritchard, Surf. Sci. **35**, 161 (1973).

[114] P. Dai, Z. Wu, T. Angot, S.-K. Wang, and H. Taub, Phys. Rev. B **59**, 15464 (1999).

[115] L. Brucha, R. D. Diehl, and J. A. Venables, Rev. Mod. Phys. **79**, 1381 (2007).

[116] S. Bornemann, J. Minár, J. Staunton, J. Honolka, A. Enders, K. Kern, and H. Ebert, Europ. Phys. J. D **45**, 529 (2007).

[117] K. Kern, R. David, P. Zeppenfeld, and G. Comsa, Surf. Sci. **195**, 353 (1988).

[118] W. Widdra, P. Trischberger, W. Frieß, and D. Menzel, Phys. Rev. B **57**, 4111 (1998).

[119] O. Šipr, S. Bornemann, J. Minár, S. Polesya, V. Popescu, A. Šimunek, and H. Ebert, J. Phys.: Condens. Matter **19**, 096203 (2007).

[120] S. H. Vosko, L. Wilk, and M. Nusair, Can. J. Phys. **58**, 1200 (1980).

[121] H. Ebert, In *Electronic Structure and Physical Properties of Solids*, edited by H. Dreyssé (Springer, Berlin, 2000), volume **535** of *Lecture Notes in Physics*, p. 191.

[122] O. Šipr, J. Minár, and H. Ebert, Cent. Eur. J. Phys. **7**, 257 (2009).

[123] A. R. Miedema and B. E. Nieuwenhuys, Surf. Sci. **104**, 191 (1981).

[124] J. Küppers, K. Wandelt, and G. Ertl, Phys. Rev. Lett. **43**, 928 (1979).

[125] K. G., S. O., Y. Lilach, and A. M., Phys. Rev. B **71**, 205414 (2005).

[126] C. W. Leming and G. L. Pollack, Phys. Rev. B **2**, 3323 (1970).

[127] S. Igarashi, A. Tosaka, T. Hirayama, and I. Arakawa, Langmuir **19**, 4627 (2003).

[128] R. Schaub, H. Joedicke, F. Brunet, R. Monot, J. Buttet, and W. Harbich, Phys. Rev. Lett. **86**, 3590 (2001).

[129] R. H. Roberts and J. Pritchard, Surf. Sci. **54**, 687 (1976).

[130] G. Schönhense, Appl. Phys. A: Solid Surf. **41**, 39 (1986).

[131] J. M. Gottlieb and L. W. Bruch, Phys. Rev. B **44**, 5759 (1991).

[132] C. T. Chen, Y. U. Idzerda, H.-J. Lin, N. V. Smith, G. Meigs, E. Chaban, G. H. Ho, E. Pellegrin, and F. Sette, Phys. Rev. Lett. **75**, 152 (1995).

[133] J. Bansmann, A. Kleibert, F. Bulut, M. Getzlaff, P. Imperia, C. Boeglin, and K.-H. Meiwes-Broer, Eur. Phys. J. D **45**, 521 (2007).

[134] T. Koide, H. Miyauchi, J. Okamoto, T. Shidara, A. Fujimori, H. Fukutani, K. Amemiya, H. Takeshita, S. Yuasa, T. Katayama, and Y. Suzuki, Phys. Rev. Lett. **87**, 257201 (2001).

[135] D. A. Eastham, Y. Qiang, T. H. Maddock, J. Kraft, J.-P. Schille, G. S. Thompson, and H. Haberland, J. Phys.: Condens. Matter **9**, L497 (1997).

[136] Y. Qiang, R. F. Sabiryanov, S. S. Jaswal, H. H. Y. Liu, and D. J. Sellmyer, Phys. Rev. B **66**, 064404 (2002).

[137] D. Altbir, J. d'Albuquerque e Castro, and P. Vargas, Phys. Rev. B **54**, R6823 (1996).

[138] J. Bartolomé, L. M. Garca, F. Bartolomé, F. Luis, R. López-Ruiz, F. Petroff, C. Deranlot, F. Wilhelm, A. Rogalev, P. Bencok, N. B. Brookes, L. Ruiz, and J. M. González-Calbet, Phys. Rev. B **77**, 184420 (2008).

[139] F. Luis, F. Bartolome, F. . Petroff, J. Bartolome, L. M. Garcia, C. Deranlot, H. Jaffres, M. J. Martinez, P. Bencok, F. Wilhelm, A. Rogalev, and N. B. Brookes, EPL (Europhysics Letters) **76**, 142 (2006).

[140] F. Luis, J. Bartolomé, F. Bartolomé, M. J. Martínez, L. M. García, F. Petroff, C. Deranlot, F. Wilhelm, and A. Rogalev, In *Enhancement of the magnetic anisotropy of Co clusters by Au capping* (AIP, 2006), volume 99, p. 08G705.

[141] R. Q. Hwang, Phys. Rev. Lett. **76**, 4757 (1996).

[142] G. H. Yang, J. Chen, and F. Pan, Phys. Stat. Solidi (a) **194**, 71 (2002).

[143] L. T. Kong, R. F. Zhang, Z. C. Li, and B. X. Liu, Phys. Rev. B **68**, 134446 (2003).

[144] S. Bornemann, J. Minár, S. Polesya, J. B. Staunton, A. I. Lichtenstein, and H. Ebert, Phys. Rev. B **80**, 014422 (2009).

[145] O. Kitakami, H. Sato, Y.Shimada, F. Sato, and M. Tanaka, Phys. Rev. B **56**, 13849 (1997).

[146] B. C. Sales, J. E. Turner, and M. B. Maple, Phys. Rev. Lett. **44**, 586 (1980).

[147] K. Morgenstern, J. Kibsgaard, J. V. Lauritsen, E. Lægsgaard, and F. Besenbacher, Surf. Sci. **601**, 1967 (2007).

[148] J. Zhang, V. Sessi, C. H. Michaelis, I. Brihuega, J. Honolka, K. Kern, R. Skomski, X. Chen, G. Rojas, and A. Enders, Phys. Rev. B **78**, 165430 (2008).

[149] F. Luis, F. Bartolome, F. Petroff, J. Bartolome, L. M. Garcia, C. Deranlot, H. Jaffres, M. J. Martinez, P. Bencok, F. Wilhelm, A. Rogalev, and N. B. Brookes, Europhys. Lett. **76**, 142 (2006).

[150] P. Imperia, P. Andreazza, D. Schmitz, J. Penuelas, and C. Andreazza-Vignolle, J. Magn. Mag. Mat. **310**, 2417 (2007).

[151] R. L. Stamps, J. Phys. D: Appl. Phys. **33**, R247 (2000).

[152] U. Nowak, K. D. Usadel, J. Keller, P. Miltényi, B. Beschoten, and G. Güntherodt, Phys. Rev. B **66**, 014430 (2002).

[153] R. Morel, C. Portemont, A. Brenac, and L. Notin, Phys. Rev. Lett. **97**, 127203 (2006).

[154] D. A. Eastham, Y. Qiang, T. H. Maddock, J. Kraft, J.-P. Schille, G. S. Thompson, and H. Haberland, J. Phys.: Condens. Matter **9**, L497 (1997).

[155] D. Weller and A. Moser, IEEE Trans. Mag. **35**, 4423 (1999).

[156] S. Sun, C. B. Murray, D. Weller, L. Folks, and A. Moser, Science **287**, 1989 (2000).

[157] R. Laskowski, P. Blaha, and K. Schwarz, Phys. Rev. B **78**, 045409 (2008).

[158] T. Brugger, S. Günther, B. Wang, J. H. Dil, M.-L. Bocquet, J. Osterwalder, J. Wintterlin, and T. Greber, Phys. Rev. B **79**, 045407 (2009).

Acknowledgments

I'm grateful to Prof Klaus Kern for the opportunity he gave me to work in his group. I will always remember his critic look at science and ability to go straight to the hearth of problems.

My profound gratitude goes to Dr. Jan Honolka for being a friend and a good colleague at the beginning of my PhD and a careful supervisor over the last two years. Thanks for allowing me to follow my own path, but also for 'forcing' me to be more pragmatic, precise and understandable in expressing my thoughts. I'm still working on that!

A very important role is also the one of Prof. Axel Enders that followed the thesis in the first two years. I have especially appreciated the effort he made to keep an eye on my advancements also after he went to the United States.

Thanks to Liza Herrera Diez and Simon Hertenberger, my colleagues in the Nanomagnetism subgroup the last years. With both it has been a real pleasure to work together. I also acknowledge my predecessor Dr. Diego Repetto from whom I have inherited a UHV chamber in a very good state and Dr. Jian Zhang that developed at the beginning the clusters on the nano-mesh project.

I acknowledge the jury members of the PhD exam Prof. Wolf-Dieter Schneider, Prof. Thomas Greber and Prof. Pietro Gambardella and the President of the jury Prof. Giovanni Dietler.

Thanks to Dr. Sven Bornemann, Dr. Jan Minár, Prof. Hubert Ebert and Dr. Ondrej Šipr for the DFT calculations that contributed substantially to the comprehension of experimental data.

My acknowledgment also goes to Dr. Fabrizio Arciprete and Dr. Ernesto Placidi, my former colleagues at the University of Tor Vergata in Rome, for helping me with the translation of the abstract in italian.

Many of the results of my thesis are based on measurements done at synchrotron facilities. Those experiments have been often quite challenging, and therefore I'm thankful to the researchers and technicians that contributed to the realization: Dr. Peter Bencok, Dr. Carsten Tieg, Dr. Júlio Criginski

Cezar at the ID08 beamline of ESRF, Dr. Didier Wermeille, Dr. Roberto Felici, Helena Isern and Thomas Dufrane at ID03 and Dr. Detlef Schmitz at the beamline UE-46 of BESSY II.

Thanks to Dr Stefan Gsell for providing us Rh/YSZ/Si(111) samples and to Ute Salzberger, Peter Kopold and Dr. Peter A. van Acken for TEM measurements. I also acknowledge Wolfgang Stiepany and Hermann Beer for technical help with the UHV components.

Thanks to the Max Planck Institute for Festkörperforschung in Stuttgart that hosted me in these four years and to the financial support from the DFG Schwerpunktprogramm SPP 1153.

All over my PhD time I have met a few generations of students and researchers and all of them added something to my scientific and personal development. Among them, and I apologize to mention only few of them, I would like to recall the ’hard core’ of my first period: Stephan Rauschenbach, Sören Neubeck, Dietmar Payer, Sebastian Stepanow, Magalí Lingenfelder, Paula Acosta-Diaz, Georgios Katsaros, Alexander Langner and Robin Ohmann. Of the ’new’ generation I would like to thank Adarsh Sagar and Ravi Shankar Sundaram for teaching me a bit of transport measurements and Tzu Chun Tseng and Stefan Kahle for sharing nice time in the office. I also acknowledge Dr. Markus Ternes for discussions and advices. I’m indebted to Dr. Klaus Kuhnke and Dr. Lucia Vitali for the help they both gave me in several occasions. A special thanks also goes to Maximilian Assig, Eduardo Lee and Christian Michaelis. With them I have shared many moments of happiness but also disappointment towards experiments and machines, together with long discussions about science and life.

Finally I acknowledge my parents and my brother for the continuous love and support they gave me since I was born.

Publications

- V.Sessi, K. Kuhnke, C. H. Michaelis, D. Wermeille, R. Felici, J. Honolka, and K. Kern
  Growth of Co on atomically flat Xe layers studied by surface scattering and diffraction
  in preparation

- V.Sessi, K. Kuhnke, J. Zhang, A. Enders, C. Tieg, J. Minár, O. Šipr, H. Ebert, J. Honolka, and K. Kern
  Magnetic moments of Rh nanostructures on rare-gas layers
  in preparation

- V. Sessi, K. Kuhnke, A. Enders, J. Zhang, P. Bencok, S. Bornemann, J. Minár, H. Ebert, J. Honolka, and K. Kern
  Cobalt nano-clusters on metal supported Xe monolayers: influence of the substrate on cluster formation kinetics and magnetism
  submitted to Phys. Rev. B (2009)

- J. Honolka, T.Y. Lee, K. Kuhnke, D. Repetto, V. Sessi, P. Wahl, A. Buchsbaum, P. Varga, S. Gardonio, C. Carbone, S. R. Krishnakumar, P. Gambardella, M. Komelj, R. Singer, M. Fhnle, K. Fauth, G. Schtz, A. Enders, and K. Kern
  Complex magnetic phase in submonolayer Fe stripes on Pt(997)
  Phys. Rev. B **79**, 104430 (2009)

- J. Zhang, V. Sessi, C. H. Michaelis, I. Brihuega, J. Honolka, K. Kern, R. Skomski, X. Chen, G. Rojas, and A. Enders
  Ordered Layers of Co Clusters On Boron-Nitride Template Layers
  Phys. Rev. B **78**, 165430 (2008)

- I. Brihuega, Ch. Michaelis, J. Zhang, S. Bose, V. Sessi, J. Honolka, M. A. Schneider, A. Enders, and K. Kern
  Electronic decoupling and templating of Co nanoclusters arrays on the

boron nitride nanomesh
Surf. Sci. Lett. **602**, L95 (2008)

- R. Skomski, J. Zhang, V. Sessi, J. Honolka, K. Kern, and A. Enders
  Substrate-Controlled Growth and Magnetism of Nanosize Fe Clusters on Pt
  J. Appl. Phys. **103**, 07D519 (2008)
- J. Zhang, D. Repetto, V. Sessi, J. Honolka, K. Kern, and A. Enders
  Magnetism of Fe ckusters formed by buffer-layer assisted growth on Pt(997)
  Europ. Phys. J. D **45**, 515 (2007)
- D. Repetto, T.Y. Lee, S. Rusponi, J. Honolka, K. Kuhnke, V. Sessi, U. Starke, H. Brune, P. Gambardella, C. Carbone, A. Enders, and K. Kern
  Structure and magnetism of atomically thin Fe layers on flat and vicinal Pt surfaces
  Phys. Rev. B **74**, 054408 (2006)
- F. Arciprete, E. Placidi, V. Sessi, M. Fanfoni, F. Patella and A. Balzarotti
  How kinetics drives the two- to three-dimensional transition in semiconductor strained heterostructures: the case of InAs/GaAs(001)
  Appl. Phys. Lett. **89** 041904 (2006)
- E. Placidi, F. Arciprete, V. Sessi, M. Fanfoni, F. Patella and A. Balzarotti
  Step erosion during InAs quantum dots on GaAs(001) surface
  Appl. Phys. Lett. **86**, 241913, (2005) [Cover page for Issue 24]
- F. Patella, F. Arciprete, M. Fanfoni, V. Sessi, A. Balzarotti and E. Placidi
  Reflection high electron energy diffraction observation of surface mass transport at the two- to three- dimensional growth transition of InAs on GaAs(001)
  Appl. Phys. Lett. **87**, 252101 (2005)

Curriculum vitae

Name	Violetta Sessi
Date of Birth	December 15, 1978
Nationality	Italian
1992-1997	High School at Liceo Scientifico 'Renato Cartesio', Olevano Romano, Roma, Italy
Oct. 1997-Sept. 2000	Study of Physics at University of Rome 'La Sapienza', Rome, Italy
Oct. 2000-Jan. 2005	Study of Physics at University of Rome 'Tor Vergata', Rome, Italy
Oct. 2003-Jan. 2005	Diploma thesis at University of Rome 'Tor Vergata' in the group of Prof. A. Balzarotti 'Eteroepitassia di InAs su GaAs: analisi in microscopia a forza atomica della transizione 2D-3D'
Jul. 2005-Aug. 2009	Doctoral research in the group of Prof Klaus Kern at Max Planck Institute for Solid State Research, Stuttgart, Germany